USAGE OF 3D PRINTED PLA SCAFFOLDS FOR SMALL MOLECULE INDUCED BONE REGENERATION

by
Nisa İrem Büyük

Submitted to Graduate School of Natural and Applied Sciences
in Partial Fulfillment of the Requirements
for the Degree of Doctor of Philosophy in
Biotechnology

Yeditepe University
2023

USAGE OF 3D PRINTED PLA SCAFFOLDS FOR SMALL MOLECULE INDUCED BONE REGENERATION

APPROVED BY:

Prof. Dr. Gamze Torun Köse ……
(Thesis Supervisor)
(Yeditepe University)

Assist. Prof. Dr. Gülengül Duman ……
(Yeditepe University)

Prof. Dr. Halime Kenar ……
(Acıbadem University)

Assist. Prof. Dr. Görke Gürel Peközer ……
(Yıldız Technical University)

Assist. Prof. Dr. Mehmet Hikmet Üçışık ……
(Yeditepe University)

DATE OF APPROVAL: ..../..../2023

I hereby declare that this thesis is my own work and that all information in this thesis has been obtained and presented in accordance with academic rules and ethical conduct. I have fully cited and referenced all material and results as required by these rules and conduct, and this thesis study does not contain any plagiarism. If any material used in the thesis requires copyright, the necessary permissions have been obtained. No material from this thesis has been used for the award of another degree.

I accept all kinds of legal liability that may arise in case contrary to these situations.

Name, Last name ……

Signature …..…….……..

ACKNOWLEDGEMENTS

I would like to express my deepest gratitude and endless respect to my supervisor, Prof. Dr. Gamze Köse, whose knowledge I benefited from during my education and who set an example with her humanitarian and moral values. I was honored to have her as my advisor. I'm grateful to her for the love, respect, and tolerance she showed throughout my thesis.

I am indebted to my thesis committee members for their kindness and support.

I would like to thank my laboratory colleagues Dr. Ezgi Bektaş, Didem Aksu, Kardelen Tüfekçi, and Afra Demirci for believing in me and supporting me from the beginning to the end of my thesis.

I would like to thank my dear friends, whose interest and support I felt during this difficult process of preparing my thesis, as in every other period of my life.

Finally, I would like to extend my sincere thanks to my dear family, who have always stood by me throughout my life and supported me unconditionally in all matters.

This study was supported by the Tübitak BIDEB 2211/A scholarship program.

ABSTRACT

USAGE OF 3D PRINTED PLA SCAFFOLDS FOR SMALL MOLECULE INDUCED BONE REGENERATION

Bone is a tissue that has the ability to repair itself. However, critical bone damage that may occur as a result of trauma, tumor, disease, or infection cannot heal naturally. Developed 3D-printed scaffolds used in bone repair and regeneration applications stand out in this context. Chitosan nanoparticles increase the biocompatibility of synthetic polymer scaffolds as they support cell adhesion while also inducing bone differentiation of stem cells. On the other hand, bone tissue engineered structures were found to fail after implantation, usually due to insufficient vascularization. In tissue engineering, media and factors that enable endothelial cells to migrate to the region are used to support vascularization.

In this study, poly (lactic acid) scaffolds produced with a 3D printer were used for bone regeneration. The ideal pore sizes of the scaffolds were determined at 370–460 μm. The scaffolds were alkali treated with 0.5 M NaOH for 4 hours, and the surfactant groups were exposed. Within the scope of the study, DIPQUO and GS4012 small molecules were encapsulated in chitosan nanoparticles to induce bone formation and vascularization, respectively. The surfaces of the scaffolds were coated with these nanoparticles. Mesenchymal stem cells isolated from rat bone marrow were seeded on the scaffold, and differentiation into bone tissue was achieved with controlled release of small molecules. Peripheral blood endothelial cells isolated in vitro from rat blood were used to test vascularization success. The designed system was tested in vitro in terms of osteogenesis and angiogenesis properties, and bone tissue formation was investigated. It was observed that bone differentiation was high in DIPQUO-containing groups (D-NP and DG-NP), while cell proliferation increased with vascularization in group containing GS4012 (G-NP). With this study, the bioactivity of the scaffold was increased by the encapsulation of small molecules, and the failure rate due to insufficient vascularization encountered in bone tissue engineering studies was reduced. Finally, the patient's recovery period was shortened by accelerating the healing process of bone injuries.

ÖZET

KÜÇÜK MOLEKÜL İLE İNDÜKLENMİŞ KEMİK REJENERASYONU İÇİN 3B BASILI PLA İSKELELERİNİN KULLANIMI

Kemik, kendini tamir etme yeteneğine sahip bir dokudur. Ancak, travma, tümör, hastalık veya enfeksiyon sonucu oluşabilecek kritik boyutlu kemik hasarları kendiliğinden iyileşemez. Kemik onarımı ve rejenerasyonu uygulamalarında geliştirilen 3D baskılı doku iskeleleri bu bağlamda öne çıkmaktadır. Kitosan nanoparçacıkları, hücre adezyonunu desteklerken aynı zamanda kök hücrelerin kemik farklılaşmasını tetikledikleri için sentetik polimer doku iskelelerinin biyouyumluluğunu arttırır. Öte yandan, kemik doku mühendisliği ile oluşturulmuş yapıların, implantasyondan sonra genellikle yetersiz vaskülarizasyona bağlı olarak başarısız olduğu görülmüştür. Doku mühendisliğinde vaskülarizasyonu desteklemek için endotel hücrelerin bölgeye göç etmesini sağlayıcı ortam ve faktörler kullanılmaktadır.

Bu çalışmada, kemik rejenerasyonu için 3D yazıcı ile üretilmiş poli(laktik asit) doku iskeleleri kullanılmıştır. İskelelerin ideal gözenek boyutları 370–460 μm olarak belirlenmiştir. Doku iskeleleri, 0.5 M NaOH ile 4 saat boyunca alkali muamelesine tabi tutularak yüzey aktif grupları açığa çıkarılmıştır. Çalışma kapsamında sırasıyla DIPQUO ve GS4012 küçük molekülleri kitosan nanoparçacıkları içinde kapsüllenerek kemik oluşumu ve vaskülarizasyon sağlanmıştır. Doku iskelelerinin yüzeyi bu nanopartiküller ile kaplanmıştır. Sıçan kemik iliğinden izole edilen mezenkimal kök hücreler doku iskelesi üzerine ekilmiş ve küçük moleküllerin kontrollü salımı ile kemik dokusuna farklılaşma sağlanmıştır. Vaskülarizasyon başarısını test etmek için in vitro ortamda sıçan kanından izole edilen periferik kan endotel hücreleri kullanılmıştır. Tasarlanan sistem, in vitro ortamda osteogenez ve anjiyogenez özellikleri bakımından test edilmiş ve kemik dokusu oluşumu incelenmiştir. DIPQUO içeren gruplarda (D-NP ve DG-NP) kemik farklılaşmasının yüksek olduğu, GS4012 (G-NP ve DG-NP) içeren gruplarda ise vaskülarizasyon ile hücre çoğalmasının arttığı gözlenmiştir. Bu çalışmada küçük moleküllerin enkapsülasyonu ile doku iskelesinin biyoaktivitesi arttırılmış ve kemik doku mühendisliği çalışmalarında karşılaşılan yetersiz vaskülarizasyona bağlı başarısızlık oranını azaltılmıştır. Son olarak, kemik yaralanmalarının iyileşme süreci hızlandırılarak hastanın iyileşme süresi kısaltılmıştır.

TABLE OF CONTENTS

ACKNOWLEDGEMENTS iv

ABSTRACT v

ÖZET vi

LIST OF FIGURES xii

LIST OF TABLES xviii

LIST OF SYMBOLS/ABBREVIATIONS xix

1. INTRODUCTION 1
   1.1. BONE 2
      1.1.1. Structure 3
      1.1.2. Composition 5
      1.1.3. Cells 6
      1.1.4. Bone Defects 9
   1.2. BONE TISSUE ENGINEERING 10
      1.2.1. Cell Source 11
         1.2.1.1. Stem Cell Differentiation into the Osteoblast Lineage 13
      1.2.2. Scaffolds 14
         1.2.2.1. Polymeric Scaffolds 15
         1.2.2.2. Production Methods 20
      1.2.3. Stimulating Factors 25
         1.2.3.1. Growth Factors 26
         1.2.3.2. Small Molecules 27
         1.2.3.3. Nanoparticles 29

2. MATERIALS 32
   2.1. CHEMICALS 32
   2.2. KITS 34
   2.3. CD MARKER ANTIBODIES 34
   2.4. INSTRUMENTS 35

3. METHODS 37

3.1. PLA SCAFFOLD PREPARATION AND CHARACTERIZATION 37
3.1.1. Design and Fabrication of PLA Scaffold 37
3.1.2. Characterization of Scaffold 37
3.1.2.1. SEM 37
3.1.2.2. Fourier Transform Infrared Spectrophotometer (FT-IR) 38
3.1.2.3. Differential Scanning Calorimetry (DSC) 38
3.1.2.4. Contact Angle Measurement 38
3.1.2.5. Mechanical Analysis 38
3.1.2.6. In vitro Degradation Analysis 39
3.2. NANOPARTICLE PREPARATION AND CHARACTERIZATION 40
3.2.1. Preparation of Nanoparticles 40
3.2.2. Characterization of Nanoparticles 44
3.2.2.1. Zeta-sizer 44
3.2.2.2. TEM 44
3.2.2.3. FT-IR 44
3.2.2.4. DSC 44
3.2.2.5. Evaluation of NP Yield Analysis 44
3.2.2.6. Evaluation of NP Encapsulation Efficiency and Loading Capacity 45
3.2.2.7. In vitro Release Study of the CS Nanoparticles 45
3.2.3. Determination of Half-Maximum Inhibitory Concentration 46
3.3. NP COATING OF SCAFFOLDS 46
3.4. *IN VITRO* CELL CULTURE STUDIES 47
3.4.1. Isolation and Characterization of rBMSCs 47
3.4.1.1. Osteogenic Differentiation 48
3.4.1.2. Chondrogenic Differentiation 48
3.4.1.3. Adipogenic Differentiation 48
3.4.1.4. Flow Cytometry Analysis 49
3.4.2. Isolation and Characterization of rPBECs 49
3.4.2.1. CD31 (PECAM-1) 50
3.4.2.2. Dil acetylated low-density lipoprotein (Dil-Ac-LDL) 50
3.4.3. Cell Labeling 51
3.4.3.1. Labeling of rBMSCs 51
3.4.3.2. Labeling of rPBECs 51

3.5. *IN VITRO* MATERIAL-CELL INTERACTIONS 52
3.5.1. Cell Viability by MTS Assay 52
3.5.2. Live-Dead Assay 52
3.5.3. Cell Proliferation by PicoGreen Assay 53
3.5.4. Alkaline Phosphatase Activity 53
3.5.5. Calcium Assay 53
3.5.6. Osteocalcin Analysis 54
3.5.7. Realtime-PCR 54
3.5.8. von Kossa Staining 55
3.5.9. Alizarin Red Staining 55
3.5.10. *In Vitro* Angiogenesis 56
3.5.11. Migration Assay 56
3.5.12. Immunofluorescence Staining of Coated Scaffolds 57
4. RESULTS 58
4.1. PLA SCAFFOLD CHARACTERIZATION 58
4.1.1. Bright Field and Scanning Electron Microscope Analysis 58
4.1.2. Fourier Transform Infrared Spectrophotometer (FT-IR) 60
4.1.3. Differential Scanning Calorimetry (DSC) 61
4.1.4. Contact Angle Measurement 62
4.1.5. Mechanical Analysis 62
4.1.6. *In vitro* Degradation Analysis 64
4.2. NANOPARTICLE CHARACTERIZATION 68
4.2.1. Zeta-sizer 68
4.2.2. TEM 72
4.2.3. FT-IR 72
4.2.4. DSC 74
4.2.5. Evaluation of NP Encapsulation Efficiency and Loading Capacity 75
4.2.6. Evaluation of NP Yield Analysis 76
4.2.7. *In vitro* Release Study of the CS Nanoparticles 76
4.2.8. Determination of Half Maximal Inhibitory Concentration 77
4.3. NP COATING OF SCAFFOLDS 78
4.4. *IN VITRO* CELL CULTURE STUDIES 80
4.4.1. Characterization of rBMSCs 80

4.4.1.1. Osteogenic Differentiation....80
4.4.1.2. Chondrogenic Differentiation....81
4.4.1.3. Adipogenic Differentiation....82
4.4.1.4. Flow Cytometry Analysis....82
4.4.2. Characterization of rPBECs....83
4.4.2.1. CD31 (PECAM-1)....83
4.4.2.2. Dil acetylated low-density lipoprotein (Dil-Ac-LDL)....84
4.4.3. Cell Labeling....85
4.5. *IN VITRO* MATERIAL-CELL INTERACTIONS....86
4.5.1. PLA Scaffold-Cell Interactions....86
4.5.1.1. Cell Viability by MTS Assay....86
4.5.1.2. Live-Dead Assay....88
4.5.1.3. Cell Proliferation by PicoGreen Assay....89
4.5.1.4. Alkaline Phosphatase Activity....90
4.5.1.5. von Kossa Staining....90
4.5.2. Chitosan Nanoparticle-Cell Interactions....91
4.5.2.1. Cell Viability by MTS Assay....91
4.5.2.2. Alkaline Phosphatase Activity....92
4.5.2.3. Hematoxylin&Eosin Staining....93
4.5.2.4. Alizarin Red Staining....94
4.5.2.5. von Kossa Staining....95
4.5.3. NP Coated PLA Scaffold-Cell Interactions....96
4.5.3.1. Cell Viability by MTS Assay....96
4.5.3.2. Live-Dead Assay....97
4.5.3.3. Cell Proliferation by PicoGreen Assay....98
4.5.3.4. Alkaline Phosphatase Activity....99
4.5.3.5. Calcium Assay....100
4.5.3.6. Osteocalcin....100
4.5.3.7. Alizarin Red Staining....101
4.5.3.8. von Kossa Staining....101
4.5.3.9. Realtime-PCR....102
4.5.3.10. In Vitro Angiogenesis....103
4.5.3.11. Migration Assay....104

4.5.3.12. Immunofluorescence Staining of Coated Scaffolds.....105

5. DISCUSSION.....107

6. CONCLUSION 119

7. FUTURE PROSPECTS.....121

REFERENCES ……..122

APPENDIX A ……..138

LIST OF FIGURES

Figure 1.1 A long bone's anatomy [5] 4

Figure 1.2 Blood and nervous system in bone [5] 5

Figure 1.3 Bone cells [5] 7

Figure 1.4 Two enantiomer forms of lactic acid [46] 17

Figure 1.5 Chemical structure of (a) PLLA, (b) PDLA, (c) PDLLA [47] 18

Figure 1.6 Scaffold production techniques: (a) solvent casting-particle leaching process (b) freeze drying process (c) supercritical fluid technology (d) phase separation technology (e) wet spinning process (f) electrospinning process (g) melt molding technique (h) layout of Solid Free Form (SFF) process [41] 22

Figure 1.7 A schematic representation of three commonly used additive manufacturing processes also referred to as 3D printing for bone engineering: fused deposition modeling, stereolithography, and selective laser sintering [63] 23

Figure 1.8 Molecular structure of DIPQUO [84] 28

Figure 1.9 Molecular structure of GS4012 [88] 29

Figure 3.1 Schematic representation of dual small molecule loaded chitosan nanoparticle synthesis. Created with BioRender.com 41

Figure 3.2 Isolation of endothelial cells from rat peripheral blood (A) before and (B) after centrifugation. 50

Figure 4.1 Structural and morphological characterization of a 3D-printed PLA (BASF) scaffold with different pore sizes (50, 60, 70, 80, and 90%). (A) CAD design of the 3D-printed scaffolds, (B) Digital images of 3D-printed scaffolds, (C) BF images of 3D-printed scaffolds, scale: 200 μm, (D) SEM analysis of 3D-printed scaffolds : (1) Top view images of the 3D-printed scaffolds, scale: 200 μm, (2) Cross-section images of the 3D-printed scaffolds, scale: 100 μm. 59

Figure 4.2 Structural and morphological characterization of 3D-printed PLA (Corbion) scaffold with 60% filling rate. (A) Digital image, (B) BF image, scale:200 μm, (C) SEM analysis, top view image, scale: 200 μm, (D) SEM analysis, cross-section image, scale: 100 μm. 60

Figure 4.3 FT-IR spectrum of PLA. 61

Figure 4.4 DSC thermograms of pre and post printing of PLA, respectively. 61

Figure 4.5 Contact angle measurement analysis of 3D-printed scaffolds. (A) Values of the contact angle of the 3D-printed scaffolds with different filling rates, (B) Images of the droplet of the 3D-printed scaffolds with a filling rates of (a) 50%, (b) 60%, (c) 70%, (d) 80%, and (e) 90%..... 62

Figure 4.6 Digital images of scaffolds before and after mechanical analysis: (A) compression and (B) tensile analyses. 63

Figure 4.7 Mechanical analysis of 3D-printed PLA scaffolds with different filling rates. (A) Compressive Young's modulus, (B) Compressive strength at yield, (C) Compressive strength at break, (D) Tensile Young's modulus, (E) Ultimate tensile strength, (F) Fracture strength of the 3D-printed PLA scaffold with different filling rates; n=3, $p < 0.0001$. *$p < 0.05$; ****$p < 0.0001$. 64

Figure 4.8 *In vitro* degradation behavior of 3D-printed PLA (BASF) scaffolds with different filling rates in PBS solution at 37 °C with respect to (A) weight loss (%), (B) swelling ratio (%), and (C) pH changes throughout 120 days of incubation..... 65

Figure 4.9 Enzymatic degradation behavior of 3D-printed PLA scaffolds with different filling rates in enzyme solution at 37 °C with respect to (A) weight loss (%), and (B) pH changes throughout 10 days of incubation. 66

Figure 4.10 *In vitro* degradation behavior of a 3D-printed PLA (Corbion) scaffold in PBS solution at 37 °C with respect to (A) weight loss (%), (B) swelling ratio (%), and (C) pH changes throughout 120 days of incubation. 66

Figure 4.11 Enzymatic degradation behavior of 3D-printed PLA scaffolds in enzyme solution at 37 °C with respect to (A) weight loss (%), (B) swelling ratio (%), and (C) pH changes throughout 15 days of incubation. 67

Figure 4.12 Size distribution graphs of blank NPs with ionic gelation method using (A) magnetic stirrer, (B) burette, and (C) sonicator. 70

Figure 4.13 Size distribution graphs of NPs synthesized with magnetic stirrer (A) blank NP, (B) BSA-NP, (C) D-NP, (D) G-NP, and (E) DG-NP. 70

Figure 4.14 Zeta potential distribution graphs of (A) blank NP, (B) BSA-NP, (C) D-NP, (D) G-NP, and (E) DG-NP. 71

Figure 4.15 TEM micrographs of blank chitosan nanoparticles with a scale of (A) 200 nm, and (B) 100 nm. 72

Figure 4.16 FT-IR spectra of (A) chitosan, (B) TPP, (C) Tween 20, (D) DIPQUO, (E) GS4012, and (F) blank and loaded NPs. 74

Figure 4.17 DSC spectra of (A) chitosan, TPP, and Tween 20, and (B) blank and loaded NPs. 75

Figure 4.18 Absorbance peaks of (A) DIPQUO, and (B) GS4012 75

Figure 4.19 *In vitro* release study of (A) BSA loaded chitosan NP, and (B) small molecule loaded chitosan NP, (C) Dialysis bags with (1) BSA loaded NPs and (2) small molecules loaded NPs. 77

Figure 4.20 The half maximal inhibitory concentration graphs of (A) DIPQUO, and (B) GS4012. 78

Figure 4.21 Scanning electron micrographs of (A) untreated, and (B) alkaline treated (0.5 M NaOH for 4 h) scaffolds that were coated with NPs either by mixing them on a magnetic stirrer and then air-drying (C, D, E, F) or by adding them directly and drying in a vacuum desiccator (G, H, I, J). Scaffolds treated with (C, G) 1.25 M NaOH for 2 h, (D, H) 1.25 M NaOH for 4 h, (E, I) 0.5 M NaOH for 2 h, and (F, J) 0.5 M NaOH for 4 h. Scale: 10 μm and indent scale: 2 μm. 79

Figure 4.22 Osteogenic differentiation stainings of rBMSCs in GM and OM by (A) von Kossa, and (B) alizarin red stainings, scale: 200 μm. 80

Figure 4.23 Chondrogenic differentiation of rBMSCs in GM and OM bu alcian blue-PAS staining, scale: 200 μm. 81

Figure 4.24 Adipogenic differentiation stainings of rBMSCs in GM and OM by oil red O, scale: 200 μm. 82

Figure 4.25 Flow cytometry analysis of rBMSCs stained with CD90, CD29, CD45, and CD34. 83

Figure 4.26 Bright field images of rPBECS with a scale of (A) 200 μm, and (B) 100 μm. 83

Figure 4.27 Fluorescent microscopy images of rPBECS labeled with CD31 (PECAM). Magnification: (A) 20X, and (B) 40X. Green: CD31, Blue: DAPI. 84

Figure 4.28 rPBECs after the Dil-Ac-LDL uptake study. Magnification: (A) 10X, and (B) 20X. 84

Figure 4.29 Fluorescence microscopy images of red fluorescent-labeled rBMSCs with a scale of (A) 200 μm, and (B) 100 μm. 85

Figure 4.30 Fluorescence microscopy images of vybrant-labeled rPBECs with a scale of (A) 200 μm, and (B) 100 μm. 85

Figure 4.31 Cell viability by MTS assay in 3D-printed PLA scaffolds that were seeded with (A) 3T3 in DMEM growth medium, (B) rBMSCs in MEM-a growth medium, and (C) rBMSCs in OM with a density of 5×10^4 cells, n=3, $p < 0.05$. 87

Figure 4.32 Cell viability by MTS assay in 3D-printed PLA (Corbion) scaffolds with a 60% filling rate that were seeded with rBMSCs in GM or OM with a density of 5×10^4, n=3. 87

Figure 4.33 (A) Cell viability by Live-Dead assay in 3D-printed PLA (BASF) scaffolds that were seeded with rBMSC throughout 1, 7, 14, and 21 days of incubation (dead cells: red; live cells: green), scale: 200 μm. Graphs of (B) live cells and (C) dead cells as a percentage of total area. 88

Figure 4.34 Cell viability by Live-Dead assay in 3D-printed PLA (Corbion) scaffolds with 60% filling rate that were seeded with rBMSC throughout 1, 7, 14, and 21 days of incubation (dead cells: red; live cells: green), scale: 200 μm. 89

Figure 4.35 Cell proliferation (PicoGreen) assay of rBMSC seeded scaffolds; $p < 0.05$.... 89

Figure 4.36 ALP analysis after 3, 7, 14, and 21 days of culturing. The data were normalized against DNA content; n=3, $p < 0.05$, ****$p < 0.0001$. 90

Figure 4.37 von Kossa staining of scaffolds in growth medium (GM) and osteogenic medium (OM) after 7, 14, and 21 days in culture. 91

Figure 4.38 rBMSCs viability upon NP application by MTS assay. Cells were seeded at a density of 5 x 10^4 in DMEM growth medium, n=3, $p < 0.05$. 92

Figure 4.39 ALP analysis after 7, 14, and 21 days of culturing. The data were normalized against protein content, n=3, $p < 0.05$. 92

Figure 4.40 Hematoxylin & Eosin staining of NP treated cells in OM after 7, 14, and 21 days in culture, scale:200 μm. 93

Figure 4.41 Alizarin red staining of NP treated cells in OM after 7, 14, and 21 days in culture, scale:200 μm. 94

Figure 4.42 von Kossa staining of NP treated cells in OM after 7, 14, and 21 days in culture, scale:200 μm. 95

Figure 4.43 Cell viability by MTS assay of untreated and treated scaffolds coated with nanoparticles in (A) a 1:1 ratio, (B) different ratios, and (C) different ratios and seeding methods. Initial cell seeding density was 5 x 10^4 cells/scaffold. 96

Figure 4.44 Cell viability by MTS assay of uncoated, untreated, and treated scaffolds coated with nanoparticles in a 1:20 ratio. Initial rBMSC seeding density was 5 x 104 in DMEM growth medium. 97

Figure 4.45 rBMSC viability by Live-Dead assay in 3D-printed NP coated PLA scaffolds throughout 7, 14, and 21 days of incubation (dead cells: red; live cells: green), scale:200 μm. 98

Figure 4.46 Cell proliferation by PicoGreen assay of rBMSC seeded NP coated scaffolds. $p < 0.05$. Initial cell seeding density was 5 x 10^4 cells/scaffold. 99

Figure 4.47 ALP analysis on rBMSC seeded NP coated scaffolds after 7, 14, and 21 days of culturing. The data were normalized against DNA content; n=3, $p < 0.05$..... 99

Figure 4.48 Calcium assay of rBMSC seeded NP coated scaffolds after 7,14, and 21 days of culturing; $p < 0.05$. 100

Figure 4.49 Osteocalcin assay on rBMSC seeded NP coated scaffolds after 7,14, and 21 days of culturing: (A) Gla-OCN, and (B) Glu-OCN. 100

Figure 4.50 Alizarin red staining of rBMSC seeded NP coated scaffolds in osteogenic medium (OM) after 7, 14, and 21 days in culture..... 101

Figure 4.51 von Kossa staining of rBMSC seeded NP coated scaffolds in osteogenic medium (OM) after 7, 14, and 21 days in culture..... 102

Figure 4.52 Expression levels of A) ONC, B) Runx2, and C) Collagen type I (Col1a1).. 103

Figure 4.53 BF images obtained as a result of an *in vitro* angiogenesis assay after (A) 48 h, and, (B) 120 h with magnification of (1) 10X, and (2) 20X. EGM:endothelial growth medium. 104

Figure 4.54 Migration assay study of rPBECs in the insert with crystal violet. (A) Digital images, (B) BF images in the insert, and (C) BF images of rPBECs migrating to a tissue culture plate after migration assay. EGM:endothelial growth medium..... 105

Figure 4.55 Immunofluorescence staining of NP coated scaffolds in co-culture after 7, 14, and 21 days of incubation. Scale: 200 μm, Indent scale: 100 μm. 106

LIST OF TABLES

Table 1.1 Summary of bone cell functions and their locations [5] 8

Table 1.2 Advantages and disadvantages of SF delivery [93] 31

Table 3.1 NP synthesize conditions. 42

Table 3.2 Experimental groups used in the study. 46

Table 3.3 Sequences of the primers used for the Real Time PCR. 55

Table 4.1 Porosity, fill rates, and pore sizes (top view and cross-section) of the 3D-printed scaffold. 59

Table 4.2 DSC measurements of pre and post printing of PLA. 62

Table 4.3 Physicochemical properties of CS NPs. 68

Table 4.4 Zeta potential results of NPs. 71

Table 4.5 Reaction yield, encapsulation efficiency and loading capacity results of NPs. 76

LIST OF SYMBOLS/ABBREVIATIONS

ALP	Alkaline phosphatase
BMP	Bone morphogenetic protein
BTE	Bone tissue engineering
CAD	Computer-aided design
DSC	Differential scanning calorimetry
ECM	Extracellular matrix
ESC	Embryonic stem cell
FDA	United State Food and Drug Administration
FDM	Fused deposition modeling
FGF	Fibroblast growth factor
FT-IR	Fourier-transfrom infrared spectroscopy
GF	Growth factor
HSC	Hematopoietic stem cell
IGF	Insulin-like growth factor
MIT	Massachusetts Institute of Technology
MSC	Mesenchymal stem cell
NP	Nanoparticle
PCL	Poly(γ-caprolactone)
PDGF	Platelet-derived growth factor
PDLA	Poly (D-lactide)
PDLLA	Poly (DL-lactide)
PGA	Poly (glycolic acid)
PLA	Poly (lactic acid)
PLGA	Poly (lactic-co-glycolic acid)
PLLA	Poly (L-lactide)
PTH	Parathormone
PTHrP	Parathormone related protein
rBM	Rat bone marrow
SEM	Scanning electron microscope
SF	Stimulating factor
SFF	Solid free form

SLA	Stereolithography
SLS	Selective laser sintering
TE	Tissue engineering
TGF-β	Transforming growth factor -β
VEGF	Vascular endothelial growth factor
3D	Three dimensional
3DP	Three dimensional printing

1. INTRODUCTION

Tissue engineering (TE) has been a developing field for the improvement and restructuring of various tissues for many years. Bone tissue is the hardest tissue in the body in terms of structure and has the ability to renew. Therefore, bone tissue can solve small fractures and heal itself. However, it is insufficient for bone tissue to regenerate large fractures. As a result, research into bone tissue engineering (BTE) has increased. TE is based on three main elements: cells, scaffolds, and growth factors (GFs). Choosing the cell correctly is of great importance. The cell sources used in today's studies are examined in three separate groups: autologous, allogenic, and xenogenic. Since these cells are completely differentiated, they also have some disadvantages. Therefore, stem cells are more accurate and suitable resources for use in TE studies. In BTE studies, mesenchymal stem cells (MSCs), which show multipotent features, are usually preferred. Although the source and type of cell selection are very important for BTE, cell use alone is inadequate. For this reason, a carrier matrix should be used where the cells can attach and proliferate. This matrix is called the scaffold. Scaffolds can be made from a variety of materials or from a synthetic material. In this context, the material and design of the scaffold show great importance. Although stimulating factors (SFs), another foundation stone of TE, do not come to the fore, it is important for the precursor cells used to differentiate into the desired cell line and thus for maximum tissue healing. SFs exhibit various physical and chemical characteristics, allowing differentiation of cells on the surrounding tissue and scaffold. These three main elements are applied to BTE studies, and real bone tissue-like structures are produced under laboratory conditions. In recent years, especially with the development of three dimensional (3D) printers, bone tissue models can be produced individually. It is possible to produce scaffolds quickly and control the interconnected porous structure in this manner. It also makes standardization easy. Essential elements for obtaining an ideal scaffold in BTE are biocompatibility, porosity, suitable surface properties, osteoinductivity, suitable mechanical properties, and biodegradability.

Vascular loss is shown as the most important reason why bone healing has not been fully achieved. With the vascular system, not only is oxygen transported to the environment, but it also contains positive signals necessary for the differentiation of osteoblasts. As a new tissue is formed, the nutrition of the cells becomes possible due to this vascular structure.

In bone healing, VEGF is seen as the most important SF for angiogenesis. Osteoblasts, the cells responsible for the production of new bone tissue, are the basis of bone repair. This entails the necessity of differentiating progenitor cells into osteoblasts.

1.1. BONE

Of all the connective tissues, bone is a dynamic, complex, and highly vascularized tissue. In contrast to most tissues, bone has the ability to heal and renew itself without the need for external interventions, and at the same time it does not leave a scar. Bones' primary function is to form the skeletal system, which serves as structural support for the body. The bone has calcium and phosphate in its structure; it functions as a mineral deposit of the body, and thus it is involved in the preservation of the mineral homeostasis. Bone additionally supports muscular contraction, provides protection of internal organs, is responsible for the production of blood cells, and acts as a deposit for immune system elements [1]. Henceforth, huge deformities in bone structure can fundamentally modify the balance of the body and personal satisfaction [2].

To classify the skeletal system anatomically, it is mainly examined in five categories: (i) long tubular bones, which are longer than wide, like the femur and tibia; (ii) short bones, which are as wide as they are long, like the carpal bones; (iii) flat bones, which act as a wall for the cavities in the body, like the skull; (iv) irregular bones, which vary in shape and structure, like the vertebrae and sacrum; and (v) sesamoid bones, which are embedded in tendon or muscle [3]. This categorizing approach to dealing with an arrangement not only reflects a clear way to begin arranging and recognizing mixed-up bones, but it also legitimately reflects differences in how bones vascularize, shape, and develop, as well as changing biomechanical properties, metabolic capacities, and locomotor capacities. Flat bones, for example, are frequently present with red marrow, which produces new recruit cells, and are thus extremely vascularized [4].

1.1.1. Structure

Bone tissue, also called osseous tissue, exhibits a different structure than all other tissues in the body. Bone is a hard tissue, and all functions that belong to bones are associated with this characteristic feature.

The diaphysis and epiphysis parts of the long bone are shown in Figure 1.1. The diaphysis section can be defined as the cylindrical part of the bone extending along the upper and lower ends of the tubular bone. The walls of the diaphysis have dense and firm bone. The cavity extending within the diaphysis is defined as the medullary cavity and contains the bone marrow. The diaphysis part mostly contains yellow bone marrow, which contains mainly fat [3].

The wider part at the ends of the bone is defined as the epiphysis. The bone that forms this part is the spongy bone. The spaces in the spongy bone are filled with red bone marrow, and this part is metabolically more active than the yellow bone marrow.

The medullar cavity is covered with a layer defined as a highly sensitive endosteum. Bone growth, healing, and remodeling are performed in the endosteum. The external surface of the bone is covered with a dense, thick fibrous layer called the periosteum [3]. The periosteum layer is vastly vascularized and osteogenic. As a result of the blood vessels, nerves, and lymphatic vessels on this membrane, cells in the compact bone structure can be nourished. These blood vessels are not only important in bone growth but also play a part in bone repair; without the periosteum layer, bone cells will die and necrotize [4]. In the tendons and ligaments, which are connective tissue elements, it attaches to the bone by the periosteum layer on it and covers the entire surface, except for the epiphysis section. The epiphysis layer is covered with articular cartilage to diminish irritation and act as a cushion.

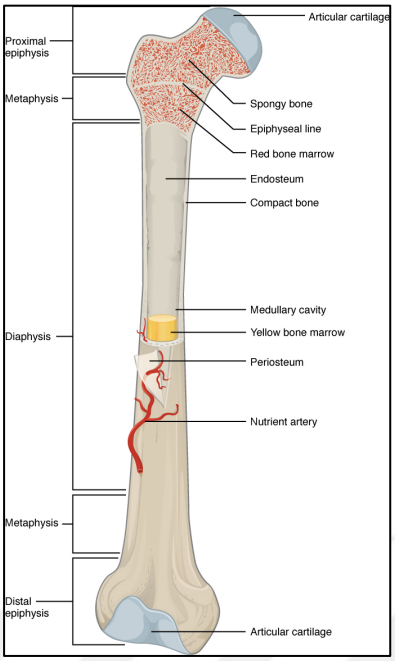


Figure 1.1 A long bone's anatomy [5]

There can be two different types of structure in the bone tissue: compact and spongy. The distribution and concentrations of the compact and spongy osseous tissue differ according to the function of the bone. The compact bone is located under the periosteum and in the diaphysis region of the long bones and exhibits a dense structure; it is also called the lamellar bone. Due to this structure, it shows resistance against compressive forces and provides support and protection. Spongy bone, or trabecular bone, is the type of bone that contains marrow spaces. Spongy bones and the medullar cavity contain veins to nourish the compact bone (Figure 1.2). The blood vessels in the periosteum continue into the spongy bone and spread from there to the marrow cavities, ensuring blood circulation. In this way, the osteocytes in spongy bone are also nourished. Spongy bone is metabolically more active than compact bone [3].

Aside from blood vessels, the neural network in bone is concentrated in the articular extremities [3], which is the metabolically more active region. The nerves in the periosteum are sensory nerves, so the pain related to a fracture is due to this signaling system [4]. The nerves not only feel pain but also take part in blood supply regulation and bone growth [5].

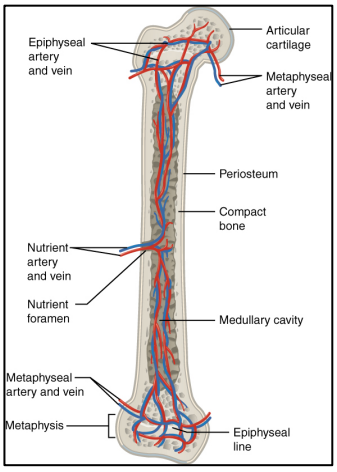


Figure 1.2 Blood and nervous system in bone [5]

1.1.2. Composition

Since there are few resident cells in the bone collagen fiber matrix, a surface is formed for the inorganic salt crystals to attach. Calcium carbonate and calcium phosphate combine to form hydroxyapatite. As a result, inorganic salt crystals are formed. Other inorganic salts employed in this process, like magnesium hydroxide, fluoride, and sulfate, crystallize or calcify on collagen fibers. Hydroxyapatite crystals provide hardness and strength to the bone, while collagen fibers provide flexibility to prevent the bone from breaking [5].

Bone is one of the hardest materials that can be synthesized biologically. Since the bone structure contains minerals and collagen, it has both stiffness and flexibility properties. As a composite material, 60% of the skeleton consists of inorganic minerals, 30% organic components, and the remaining 10% water [6]. The inorganic component of bone represents 60% of its dry weight. The vast majority of the inorganic component of the bone is hydroxyapatite ($Ca_{10}(PO_4)_6$ $(OH)_2$), the crystallized form of calcium phosphate, which has a fairly large surface area. Hyrodxyapatite is parallel to the collagen fibers [3]. The organic component of bone is represented by 40% of its dry weight. It is composed of collagen, proteoglycans, glycoproteins, phospholipids, and phosphoproteins. Collagen fibers are an important organic component of the bone matrix. Collagen type I is found in the bone; it is the primary constituent of bone, and this material can be dissolved in alkaline solvents [7]. Type I collagen forms an extensive part of the organic matrix that forms the structure of the bone. On behalf of collagen, the bone becomes more flexible and

contains peptides in its structure. The hydroxyapatite crystals are present among the collagen fibers, so in that way, collagen also has the capacity to bind calcium ions (Ca^{+2}) [8].

The second most common organic component in the bone is proteoglycans [9]. The unique mechanical and physical properties of the bone are due to the combination of collagen fibers and inorganic components in the structure, along with the proteoglycans that are found in the intercellular matrix. The tension force applied parallel to the bone axis is durable until 1,100 kg/cm^2, which is twice as high as porcelain or other ceramic products. With the crystal structure of the bone, its longitudinal compressive force can be up to 2,000 kg/cm^2.

The intercellular matrix in the bone structure contains 85% calcium phosphate, 10% calcium carbonate, 5% magnesium, and alkaline salts, respectively. The skeleton, which acts as calcium storage for the whole body, therefore serves as a source of calcium [1]. The 99% of calcium, 85% of phosphorus, and 40-60% of sodium and magnesium are stored in bones in the body [10]. In order to maintain the allostatic balance in the body, a regular exchange takes place between the blood and the skeleton. Besides the role of calcium in bones, its function in muscles is also very important. Even small changes in the level of calcium in the blood can cause cramps in the muscles. For this reason, when there is insufficient calcium intake in the body, it can utilize the calcium deposits located in the bones to maintain body balance [4].

1.1.3. Cells

The growth, regulation, healing, and all other functions of the bone are provided by three main cell types: osteoblasts, osteoclasts, and osteocytes (Figure 1.3). Osteoblast cells are derived from osteoprogenitor cells, also called osteogenic cells, which are stem cells of mesenchymal origin.

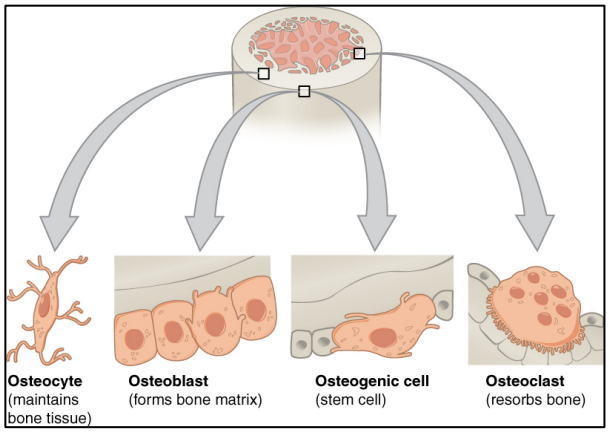


Figure 1.3 Bone cells [5]

The main task of osteoblast cells is to provide for the formation of new bone tissue. Osteoblast cells also take part in mineralization [3]. They are commonly found in the bone-growing areas. Its functions include the synthesis of unmineralized collagen tissue, thereby leading to the release of calcium phosphate; it also regulates osteoclast cells, functions in some immune functions, and provides hematopoiesis [11]. Based on the matrix produced by osteoblasts are layers of collagen fibers, which are generally type I. Osteoblasts are also responsible for producing proteoglycans. In that way, it can be said osteoblasts synthesize the main organic component of bone, which is also called osteoid [3]. Mineralization, another important task of osteoblasts, is carried out by the storage of calcium and phosphate molecules. Calcium phosphate molecules among the secreted collagen fibers are mineralized in hydroxyapatite form [4].

As long as this matrix structure secreted around the osteoblast cells is calcified, the osteoblasts are trapped in this secreted matrix structure, change their structure, and turn into osteocyte cells. Osteocytes are the main cells in the structure of mature bones and the cell type with the highest %age (nearly 90–95%) of bone cells [3]. There is mature bone tissue around each osteocyte cell, and it is responsible for preserving the mineral concentration of this matrix with the enzymes it secretes and also takes part in cell signaling. Osteocyte cells are cell types that extend along with the bone matrix so that cells can communicate with each other to exchange the necessary nutrients [5].

Both osteoblast and osteocyte cells cannot divide. Osteogenic cells are the only cell type that has the ability to divide between bone cells. Osteogenic cells initiate in the periosteum

or bone marrow, are not differentiated, and have very high mitotic activity. These stem cells differentiate and form osteoblast cells. If the osteogenic cells have the right stimuli, they can differentiate into osteoblasts, but first they become osteoprogenitor cells. These cell types can proliferate further, eventually becoming the osteoblast cell lineage [3].

If there is an old, damaged, or unnecessary part of the bone, this part is first destroyed to repair it. In this way, the bone acquires a dynamic structure and can constantly renew itself. It is the cell-type osteoclasts that are responsible for the destruction of bone. Unlike other bone cells, they are derived from monocytes or macrophages, which are immune system elements, not osteogenic cells [12]. In this multi-nucleated cell type, which varies from 3 to 25 nuclei per cell [3], there is also a lack of mitotic activity in osteoblasts and osteocytes. Osteoblasts and osteoclasts work together to maintain healthy bone tissue. Osteoclast cells destroy old bone tissue, while osteoblast cells create new bone tissue. The summary of all types of bone cell functions and their locations is presented in Table 1.1.

Table 1.1 Summary of bone cell functions and their locations [5]

Cell type	**Function**	**Location**
Osteogenic cells	Develop into osteoblasts	Deep layers of the periosteum and the marrow
Osteoblasts	Bone formation	Growing portions of bone, including periosteum and endosteum
Osteocytes	Maintain mineral concentration of matrix	Entrapped in matrix
Osteoclasts	Bone resorption	Bone surfaces and at the site of old, injured, or unneeded bone

1.1.4. Bone Defects

Problems in the bone can usually occur as a result of trauma, tumor formation, congenital disorders, an important infection, or surgery. Damage or disease in the bone structure significantly affects people's quality of life. Although it is a tissue that can renew and heal itself due to its structure, it cannot correct some major defects by itself, and a clinical intervention may be required for this. Due to the aging population and increased traffic accidents, ensuring bone regeneration has become one of the most important problems in the clinic. Osteoporosis, the bone defect of low bone mass and bone fragility, is one of the most common metabolic disorders [13]. In an American study of Caucasian women over the age of 50, nearly half of the women had osteoporosis. This ailment, which is generally thought to affect women, has also been found to affect them significantly [14]. The most common method used today for the treatment of bone defects is autologous bone grafts. An autograft is defined as the harvesting of bone from the patient’s own tissue. It has good osteoinductive and osteoconductive properties. Although it is the most frequently used method in the clinic, this method has important disadvantages, such as finding suitable donor tissue, needing an extra second operation for the tissue to be grafted, and some complications that may occur. The use of allograft may be considered an alternative to autologous use. An allograft is defined as harvesting bone from the same species, but in this treatment method, the sterilization methods applied to minimize the risk of donor incompatibility and infection cause a decrease in existing osteoinduction features. Another method of treatment is the use of xenografts. A xenograft is defined as harvesting bone from another species, but here too, the host tissue is more likely to refuse, which may cause infection or toxicity [13].

These limitations have been partially overcome by bone regeneration, which consists of a well-organized series of bone induction and conduction using a variety of bioactive implantable materials, cell types, and intracellular and extracellular molecular signaling pathways. It has been claimed that certain signaling pathways and their activated cascade pathways, as well as MSCs and their differentiation throughout remodeling processes, are involved in bone regeneration [15]. Studies in this field have gained speed in the last 20 years. Scaffolds are designed by cultivating cells that can be used instead of bone tissue [16].

1.2. BONE TISSUE ENGINEERING

Scaffolds are the basic component in TE. While scaffolds provide structural support for the tissue to be formed, they act as a temporary attachment and proliferation area for the cells and are also involved in the formation of the extracellular matrix (ECM) [17]. Some computer modeling methods can be used in the personalized design of biomaterials such as scaffolds or scaffold-like implants. Special scaffolds with porosity, geometric shape, interconnectivity, and size can be designed by modeling them on the computer [18].

The basis of the strong mechanical properties of bone is its ECM composition [19]. Organic and inorganic components in the structure of the bone are organized in a certain order, and bone cells in the structure can constantly renew themselves. In recent years, researchers have developed some TE approaches to imitate these incredible mechanical properties of bone. The goal of BTE is to provide natural bone regeneration for patients who have experienced large losses in bone tissue for various reasons, either by using only scaffolds or by combining scaffolds with cells and SFs. There are some terms used for this in BTE: osteogenic, bone-forming substances; osteoconductive, the release of bone-forming cells into the new bone tissue over time; and osteoinductive, healing or repairing the area where MSCs are located [20]. Due to the bone's ability to regenerate on its own, these structures, which have been developed with TE, induce regeneration even if they cannot completely imitate the structure of the bone. In recent years, 3D *in vitro* bone model studies have gained speed in BTE. These models facilitated the regeneration, healing, and replacement of bone tissue [21]. The bone models developed in 3D should be able to imitate the natural ECM in the structure of the bone, comply with its composition and organization, and be able to meet its mechanical properties [22].

The requirements for an ideal scaffold in BTE can be listed as follows:

- Biocompatibility: It is required to permit sufficient incorporation into the host tissue without harmful impacts (genotoxic or cytotoxic) or a potentially insusceptible reaction.

- Porosity: It is critical to get open and interconnected pores to advance vascularization, to permit the dissemination of supplements and gases, and to

permit the evacuation of metabolic squanders because of cell movement. The ideal pore size for BTE varies between 200 and 900 μm.

- Surface properties: Both chemical and superficial properties affect the attachment and proliferation of cells. While chemical properties are effective in the adhesion of cells on the material, topographic properties are effective in bone formation.
- Osteoinductivity: It is essential to induce osteogenesis.
- Mechanical properties: Since the mechanical properties of the bone are the most important part, they must withstand mechanical forces and adapt to the implanted area.
- Biodegradability: It is necessary for the material to completely dissolve *in vitro*. When the wounded area heals completely because of the controlled degradation, the scaffold disappears and is replaced with new bone tissue [18].

1.2.1. Cell Source

It is very important to select the cell source to be used in BTE. Some issues need to be considered when choosing a cell source: it should be suitable for tissue collection, the number of isolated cells should be at the maximum level, and it should not cause an immune reaction. Cells used in BTE can be classified into three categories; autologous cells are cells obtained from the patient itself, allogenic cells are cells from the same species other than the person itself, and xenogenic cells are cells of a different species [23].

Osteoblast cells come to mind as the cell type to be used in BTE studies. Osteoblast cells can be easily obtained from patients by biopsy. It is possible to increase their number by reproducing *in vitro* after the biopsy. Despite these advantages, it cannot be said that it is frequently preferred in TE applications. Because the procedure for cell isolation during biopsy should be performed within a certain period of time, although it can be proliferated *in vitro*, its capacity is limited, it may be insufficient to heal the damaged area, and the cells may enter senescence [24].

The capacity of proliferating completely differentiated cells *in vitro* is very limited, so their use in TE applications has been limited. Undifferentiated cells have a very high

proliferation capacity and are therefore a more suitable option for TE applications. The necessary stimuli factors can be given to the *in vitro* environment to differentiate these cells into the desired cell type, or a study performed in an *in vivo* environment can benefit from the physiological factors present [25].

Stem cells are a special undifferentiated cell type that can renew themselves. According to their differentiation abilities, they are examined in three different groups: (i) totipotent, (ii) pluripotent, and (iii) multipotent.

In the totipotent cell type, all living organisms can arise from a single cell. All multicellular creatures are created by a zygote, a totipotent cell. Until it reaches the blastocyst stage, the formed zygote is totipotent. A pluripotent cell type can transform into all embryonic cells; they are stem cells, but those cannot be transformed into "totipotent" and non-embryogenic cells. After the blastocyst stage, the embryo turns into a hollow cell ball, and its inner surface is covered with cells. This inner surface becomes a source for embryonic stem cells (ESCs) in the following stages and exhibits pluripotent features. While it can transform into all cell lines *in vivo*, it can also differ from a wide range of cell types *in vitro*.

Although ESCs are seen as a very suitable cell resource for TE due to their high proliferation and differentiation capacities, there is a risk of this cell type turning into unwanted cells and forming a tumor due to its differentiation ability. At the same time, the use of ESCs brings with it some ethical problems. Therefore, using adult stem cells seems to be safer and ethically acceptable [25].

Multipotent stem cells are stem cells that can be transformed into a limited number of cell types within a specific lineage. Stem cells in adult tissues can be given as examples. These cells are found to heal problems caused by tissue damage, disease, or aging. Adult stem cells can transform into cells in the same germ layer from which they were formed [26].

The MSCs are the adult stem cell type found in the connective tissues of the cells. It can also be known as stromal stem cells, connective tissue stem cells, or stromal fibroblastic stem cells. MSCs can differentiate into bone, cartilage, and fat cells. This type of stem cell, which can also be found in the bone marrow, provides hematopoiesis and acts as a source of cells for the regeneration of tissues [27,28].

Bone marrow, adipose tissue, and dental tissue are frequently preferred as the sources of MSC. Each of them has different advantages and disadvantages. In MSCs obtained from adipose tissue, morphological changes can be observed after 5 passages, the number of isolated cells is low, and the number of studies *in vivo* is low. In addition, high-yield cell isolation is possible in bone marrow MSCs, since there are many *in vivo* and *in vitro* studies and much supportive evidence to compare, but there is an invasive approach to harvesting and it is difficult to expand cells *in vitro* [29]. The most commonly used area as a MSC source is bone marrow. With a biopsy, MSCs can be obtained from there. Hematopoietic stem cells (HSCs) are also found in the bone marrow. Blood cells and osteoclast development are generated from HSCs [28,30]. When trying to obtain MSCs from bone marrow, separation is necessary because these two cell types are present together. While MSCs are the type of cells that can attach, HSCs are suspended cells, so they can be easily separated from each other in cell culture. Flow cytometry can also be used to separate these cell types. CD90, CD44, CD105, CD106, CD146, and CD166 are markers specific to the surfaces of MSCs, while CD34, CD45, CD19, and CD14 are HSCs' cell surface markers. Due to the proliferation capacities of MSCs, they can be cultured *in vitro* in large numbers, which facilitates their use in TE applications [29–31].

The cell type to be chosen in BTE is very important, but cells alone are not sufficient for tissue regeneration. There is a need for a three-dimensional scaffold where cells can attach, proliferate, and differentiate. At this point, it is concluded that the properties of the scaffold, such as its material, design, and production methods, must be planned and selected correctly.

1.2.1.1. Stem Cell Differentiation into the Osteoblast Lineage

Differentiation of MSCs into osteoblast cells occurs through various steps and factors. First of all, the MSC's immature osteoprogenitor differentiates into the cell through various transcription factors. This cell has a very high proliferation ability, while its self-healing ability is limited, and subsequently mature osteoprogenitor cells differentiate into the cell. This cell type differs in preosteoblasts and eventually in mature osteoblasts. Runt-related transcription factor 2 (Runx2), or Cbfa1, is a type of protein encoded by the Runx2 gene found in humans. It is one of the most important transcription factors in osteoblast differentiation [32]. Studies have proven that deletion of the Runx2 gene prevents bone formation [33]. Another important factor in differentiation is bone morphogenetic proteins

(BMPs). They are involved in the differentiation of mature osteoprogenitor cells into osteoblasts and the formation of the bone matrix [28,29].

Several markers are used to distinguish MSCs from desired osteoblast cells. These can be surface or cell markers. Surface markers are not often preferred because they can hold not only immature osteoprogenitors but also MSCs. Besides, cellular and molecular markers are very important. Alkaline phosphatase (ALP) is accepted as the first and most important marker. ALP is a kind of enzyme involved in bone mineralization [34]. While it is expressed by mature osteoblast cells, it cannot be synthesized from MSCs. As osteoblast differentiation increases, ALP expression in the environment also increases [28].

Collagen type 1 is the basic protein found in the bone matrix because it is the most frequently expressed protein from osteoblast cells [35]. Collagen type 1 cannot be expressed by MSCs, but it is possible to express differentiated forms of MSCs in other cell lines [28]. Therefore, it cannot be used as a definitive marker for the presence of osteoblast cells in the environment.

Osteocalcin is a common noncollagenic protein expressed by osteoblast cells. It is also known as "bone Gla-Glu protein". It makes up 20% of the non-collagenic proteins in the bone, but its function has not been fully explored [36]. Since it is not synthesized by all osteoblasts, it seems more appropriate to use it qualitatively rather than quantitatively.

Bone sialoprotein is a non-collagenic protein found in the bone matrix and is synthesized by cells in the osteoblast lineage, including in preosteoblasts. It contains 5-10% of the non-collagenic proteins in the bone. It has the capacity to bind calcium and collagen [37].

Calcium phosphate is found in mineralized matrix tissue formed by osteoblasts. It can be detected by various immunological stains (e.g., alizarin red) [28].

1.2.2. Scaffolds

Biomaterials are substances that are used to perform the functions of living tissues in the human body and that are in contact with fluids in the body continuously or for a certain period of time [38]. Scaffold is a structure with mechanical and chemical properties that is responsible for providing the appropriate microenvironment in order for the cells to adhere,

reproduce, and regenerate and heal the tissue itself. The purpose of designing the biomaterial is to protect the structural integrity of the damaged tissue or organ and to trigger mechanisms that can physiologically renew the tissue. In order to ensure complete tissue integration, the material should be degradable and not cause any side effects. Many materials are developed for these purposes. These materials must have appropriate physical, chemical, and biological signals so that a suitable microenvironment for regeneration is provided. Features that a scaffold must have include a suitable surface for cells to attach and proliferate, an induction and differentiation environment that will enable tissue growth, stimulation of cellular response, biocompatibility and biodegradability, easy reproducibility, porous structure, mechanical strength, and sterility [39]. Biomaterials that can be used for scaffolds are examined in four main groups: (i) ceramics can be combined with materials such as hydroxyapatite or calcium phosphate that exhibit osteoconductive properties to form a suitable bone scaffold; (ii) natural polymers are biocompatible and produce minumum immune reactions, and ECM proteins such as collagen, elastin, and alginate are generally used as a scaffold; (iii) synthetic polymers can be a variety of macromolecules, the properties of these macromolecules depend on the monomer from which they are formed, the copolymer ratios, the methods of synthesis; (iv) hydrogels are formed by hydration of a polymer chain and provide a suitable environment for cells [40]. All of these materials serve as supports for the attachment of cells and other ECM proteins while also facilitating the migration of cells and the participation of bioactive molecules in the structure.

1.2.2.1. Polymeric Scaffolds

Polymeric scaffolds are the most frequently used materials in TE. They can be natural or synthetic. Natural polymeric materials used in BTE can generally be protein-based, such as collagen or silk, or polysaccharide-based, such as chitosan, alginate, or gelatin. The use of natural polymers has many advantages, such as being affordable, not requiring an environmentally hazardous process for production, easy to manufacture, low toxicity, and high renewability. On the biological level, due to the natural molecules in the structure of these materials, communication with the cells is easier, and it can trigger the biological signaling mechanisms. However, despite their advantages, their low mechanical properties, their chemical stability, and their ability to cause an immune reaction limit their use. To

overcome these disadvantages, some physical or chemical modifications can replace natural polymers or composites with synthetic polymers [41].

The physical, chemical, and degradation properties of synthetic polymers can be designed specifically for each application according to the desired need and produced in the desired size or shape. The range of synthetic polymers is quite wide, with copolymers, polymer blends, and composites made with other materials. The risk of an immune reaction seen in natural polymers is lower in synthetics. A pure synthetic polymer has a nontoxic effect and is unlikely to cause infection. However, there are no biological cues that can provide cell responses or biological stimuli that change cellular responses [41]. Some chemical groups can be added to the material surface to overcome this disadvantage. Functional groups such as carboxyl, hydroxyl, or peptide sections are added to the structure to provide a biological cue [42]. Poly(-hydroxyacids) are the most commonly used synthetic polymers for scaffold production in bone and cartilage TE. Poly(α-hydroxyacids) shows biodegradable properties. The mechanism of degradation occurs at the exterior surface, not inside, which is defined as bulk degradation. The inside of the material begins to degrade when the outer surface degradation is finished, and it causes the loss of molecular weight of the polymer step by step. The degradation rate depends on chemical structure, porosity, crystallinity, molecular weight, and pH. Poly(glycolic acid) (PGA), poly(lactic acid) (PLA), and poly(lactic-co-glycolic acid) (PLGA) copolymers are the most commonly used in the literature. These materials, as well as some materials made with their copolymers, are United State Food and Drug Administration (FDA) approved, biodegradable, biocompatible, processable, and can be used to make sutures, wound dressings, and stents [39,41].

PLA

PLA, also known as polylactide, is a synthetic biodegradable aliphatic polyester that is widely used in research. PLA can be used as a substitute for petrochemical-based polymers in industrial applications and is preferred as an important biomaterial, especially in many healthcare applications [43].

PLA is one of the thermoplastics, a group of plastics that soften when heated and harden again when cooled. Thermoplastics can be recycled due to these properties. PLA is used in medical products because of its biocompatible and biodegradable properties, as well as its

high strength and modulus. It is easy to manufacture it in various forms such as film, fiber, and piece. As a biodegradable material, PLA is also important due to the nontoxicity of its degradation products [44].

PLA polymer is synthesized from lactic acid (2-hydroxypropionic acid) monomer. The chemical representation of lactic acid is CH_3–CHOHCOOH, and it is a chiral molecule. This molecule, which has two different enantiomers, L and D-lactic acid, can also be in mesoform. In mesoform, the D (-) and L (+) isomers are found in equal amounts and are called equimolar or racemic mixtures [45]. Two stereoforms of the lactide molecule are shown in Figure 1.4.

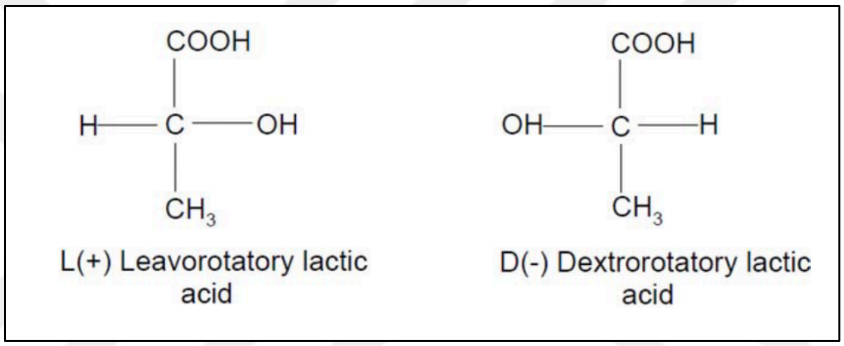


Figure 1.4 Two enantiomer forms of lactic acid [46]

PLA synthesis is possible through the polymerization of lactic acid. Just as lactic acid has different enantiomers, the PLA molecule also has different stereoisomers. These are presented in Figure 1.5 and defined as poly (L-lactide) (PLLA), poly (D-lactide) (PDLA), and poly (DL-lactide) (PDLLA). PLLA and PDLA polymers are isotactic, that is, when the side groups from the polymer chains are located in one direction below or above a plane on the main chain, and optically active crystal molecules, while PDLLA is optically inactive and in amorphous form [45]. L-isomer is a biological metabolite. PLA produced from renewable sources is usually in this form because lactic acid is usually in L- form in biological sources [43].

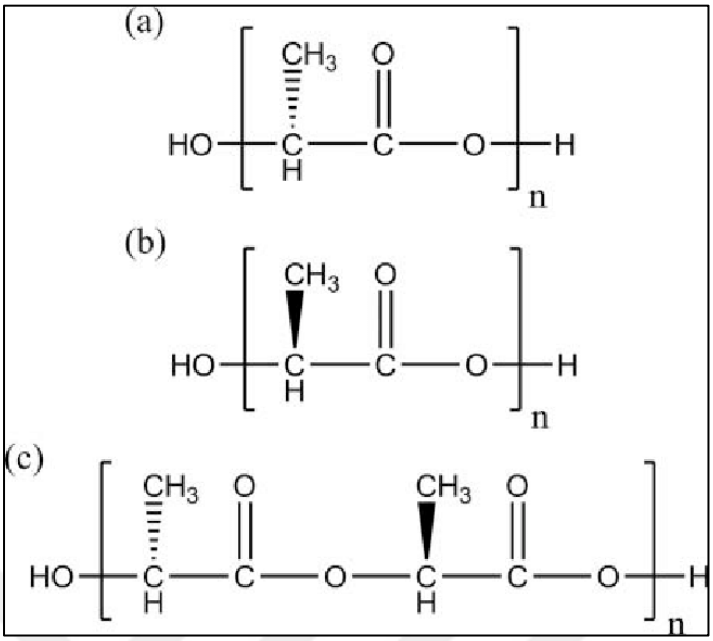


Figure 1.5 Chemical structure of (a) PLLA, (b) PDLA, (c) PDLLA [47]

With the approval of the FDA for use as a food coating product [48], studies on lactic acid have expanded and accelerated, especially in different areas such as medical applications. With its widespread application in various industries, the production of industrial-grade lactic acid-based polymers has increased in the last two decades.

The construction of PLA offers many benefits over the manufacture of other biopolymers. They are:

- Ecofriendly: PLA polymer can be obtained from renewable sources such as corn and wheat. It is in harmony with nature as it shows biodegradable, transformable, and compostable properties [44]. Also, carbon dioxide absorption occurs during production.

- Biocompatible: Biocompatible material is accepted by the physiological environment of the living creature and does not cause a toxic effect on the tissue. Besides, degradation products do not prevent tissue healing. When the PLA material is implanted into the tissue, it hydrolyzes to its monomers, lactic acid, and these degradation products are removed from the body by participating in the tricarboxylic acid cycle. Its final products are carbon dioxide and water, which are

nontoxic, making PLA a suitable material for biomedical applications [39,49]. The PLA's contact with the biological environment has been approved by the FDA.

- Processible: PLA is easier to manufacture than other biopolymers. It can be processed in many different ways. Examples of the methods used are injection molding, film extrusion, fiber spinning, and fiber forming [50].

- Energy saver: High energies may be required to synthesize petroleum-based polymers. The 25-55% less energy is required for PLA production compared to these. It is thought that the energy needed for production can be reduced by 10% with the studies conducted [49]. Since it requires less energy, its cost is also more affordable.

Despite all these mentioned advantages, PLA also has some disadvantages, and these limit the application areas.

- Poor toughness: PLA is a very fragile material, despite its high tensile strength and elastic modulus. The material's elongation at break is less than 10% [50]. Due to this weak toughness feature, it cannot be preferred for materials that require high stress levels, such as screws and broken fixation plates.

- Slow degradation rate: It degrades by hydrolyzing ester groups in the PLA structure. Crystal structure, molecular weight and distribution, morphology, the water absorption rate of the polymer, and stereoisomeric content determine the degradation rate. The degradation rate is very important for biomedical applications, and material selection is carried out accordingly. A material with a slow degradation rate can remain *in vivo* for a long time. For PLA, this period can be extended up to 3-5 years [49].

- Hydrophobicity: PLA's water contact angle has been measured at 80°, and with this value, it can be said that the material has a partial hydrophobic property. Cells like hydrophilic surfaces. Due to partial hydrophobicity, cell adhesion decreases and, in some cases, can cause an infectious reaction.

- Lack of reactive groups: PLA polymer is a chemically inert material. It has no reactive side-chain group in its structure, which makes it difficult to modify [51].

PLA draws attention as a great support structure because of the environment it creates for the natural tissue to renew itself later on by degrading in the implanted area [43]. Due to its biocompatibility, it has become a preferred polymer in TE applications [52]. The 3D porous scaffold structure can be used in cardiovascular diseases, muscle tissue, bone, and cartilage regeneration by cultivating many different cell types. The chemical composition, porous structure, and crystallinity of the PLA determine its degradation time, which can extend from ten months to four years [43]. In addition to providing tissue regeneration, PLA can also be used as a drug delivery system. It has become a preferred material in transplantation with the release of drugs such as pain relievers, anti-inflammatory drugs, and antibiotics [44].

The production of biomedical instruments with 3D printers has become quite simple as technology has advanced. When this technology combines the features of PLA, it has been seen that customized materials can be developed, and it has been used in a wide range of areas, from industrial to architectural [53]. Especially in biomedical applications, scaffolds printed with PLA have become the only examples of their kind, and TE application is used frequently. The methods used in PLA printing are generally direct or indirect 3D printing or fused deposition modeling (FDM) [54].

1.2.2.2. Production Methods

Along with the material chosen for the scaffold, the production method is also of great importance. The size, shape, and interconnectivity of the pores are crucial for tissue growth. The biggest problem is maintaining a mechanical structure while creating a porous scaffold [55]. Various methods have been developed over time for the production of scaffold (Figure 1.6). With these methods, the production of two- or three-dimensional scaffold became possible. The most commonly used method in the production of two-dimensional scaffolds is electrospinning [56–58]. In 3D scaffold production, solvent casting, freeze drying, particle/salt leaching, chemical/gas foaming, thermally induced phase separation, and the foam-gel technique are frequently used [59].

In the solvent casting-particle leaching technique, the polymer is dissolved in a solution, and porogen particles are added to the solution. The solvent is extracted from this mixture. The remaining porogen particles are removed from the medium by washing them out to obtain a porous structure. This method could be applied to any polymer that is soluble in a solvent.

In the freeze-drying technique, the polymer dissolved in the solvent is taken to a cold environment and frozen. In this way, ice crystals form in the solvent. The solvent is then removed under vacuum, and a porous structure remains.

In the supercritical fluid technique, the polymer sample is saturated with high pressure CO_2 at the point where the critical pressure increases, and then the nucleation of the CO_2 bubbles occurs by reducing the pressure.

In the phase separation technique, polymer-rich and polymer-poor phases are separated from each other by thermodynamic interactions.

In the wet spinning technique, the polymer is dissolved in the solvent and a polymer solution is obtained. This solution is continuously transferred to the coagulation bath with a thin tip, and fiber formation is observed. Due to the ongoing fibers, the superimposed structure forms the 3D structure.

Electrospinning is the accumulation of the polymer solution from the syringe in a high electric field created by high voltage and accumulating in a fiber structure on a collector field. The fibers obtained by electrospinning have high surface-to-volume ratios and good porosity.

In the melt molding technique, the mold is first coated with polymer powder, and porogen is added to the medium. By applying pressure to this mixture, the polymer is heated up to the glass transition temperature. Then the porogen is washed away from the environment, and a porous structure is obtained.

In the solid free form technique (SFF), 3D modeling is done by using computer-aided design (CAD) software on the computer or by using the image obtained using medical imaging methods, and the image is divided into layers. The resulting models are printed in 3D using SFF devices, and scaffolds are obtained for TE. In this technique, while the material itself can be printed, the cells or the cell scaffold can also be printed together [41,60]. While the traditional techniques used are frequently preferred due to the ease of production conditions, low cost, and simple equipment usage, they also have some disadvantages. These are the difficulties in controlling porosity, adjusting the pore diameter, determining the pore geometry, and providing interconnectivity. In traditional production methods, it is not possible to add cells during the production process.

New methods are being developed to overcome the disadvantages mentioned above. Chuck Hull discovered the first of these methods in 1986 [61]. The method is known as stereolithography (SLA). With subsequent studies, new techniques such as selective laser sintering (SLS), melt extrusion, FDM, and three-dimensional printing (3DP) have been developed [18,62,63]. The most recently developed method, 3DP, was found in 1994 by the Massachusetts Institute of Technology (MIT) [64]. This technique, which is frequently used in TE today, has become an important choice.

All of these listed techniques are based on a 3D CAD model designed on the computer. With these methods, it is easier to produce sensitive, high-resolution, and reproducible materials. The fact that the data obtained by medical imaging can be integrated has increased its effect, especially in the field of medicine [18].

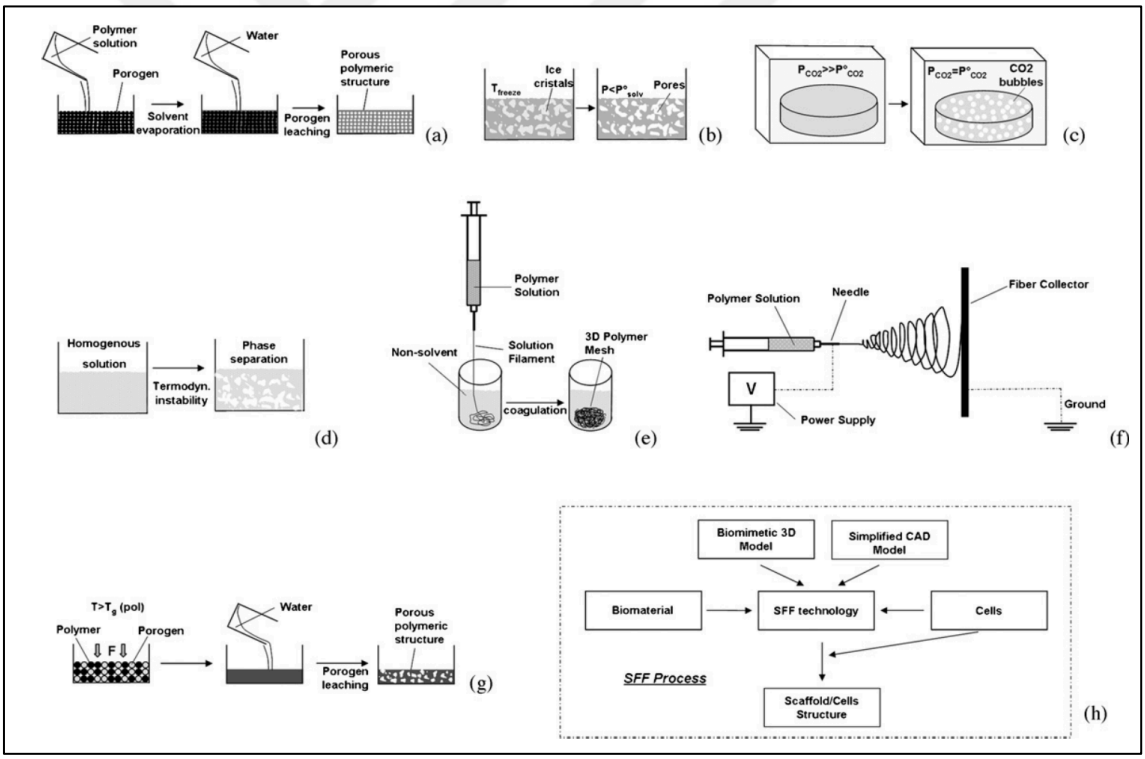


Figure 1.6 Scaffold production techniques: (a) solvent casting-particle leaching process (b) freeze drying process (c) supercritical fluid technology (d) phase separation technology (e) wet spinning process (f) electrospinning process (g) melt molding technique (h) layout of Solid Free Form (SFF) process [41]

3D Printing Technologies

With the use of 3D printing technologies developed in recent years, the structures of scaffolds have become micro-controllable. As the variety of materials available for CAD software and 3D printing has increased, the range of things that can be done with the 3D printer has also expanded. In this way, patient-specific, complex 3D materials can be developed. Today, there are many 3D printer technologies of different types. Knowing the advantages and disadvantages of each of these technologies makes it easy to design the scaffold to be used in BTE with the required level and features. There are four types of 3D printing technologies that are known and used today: SLA, FDM, SLS, and 3DP (Figure 1.7).

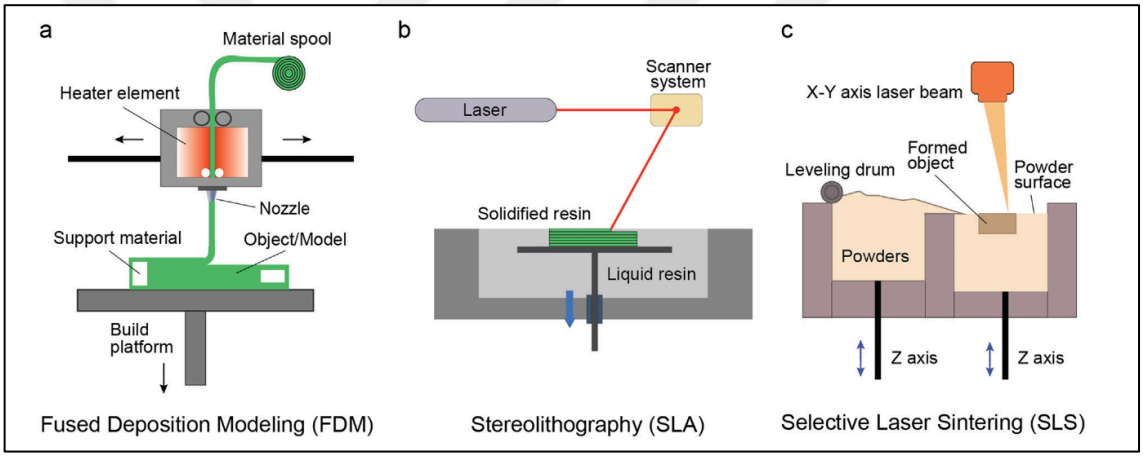


Figure 1.7 A schematic representation of three commonly used additive manufacturing processes also referred to as 3D printing for bone engineering: fused deposition modeling, stereolithography, and selective laser sintering [63]

In addition to being the first 3D printer technology developed, SLA is also the first printer technology used in BTE. In this method, each layer of the photosensitive polymer selected using an ultraviolet light or laser source is polymerized [18]. With the precision of SLA fabrication, micro- or nanosized structures can be printed. It is possible to print tens or even hundreds of times more precisely with extrusion-based printers. With SLA, it is possible to print even very complex designs in the finest detail [27]. Due to its high resolution and sensitivity, SLA has become a suitable technology for BTE. Although it is possible to print a scaffold with the desired details, there are some limitations to scaffolds printed with SLA. First of all, there are very few compatible materials with SLA in BTE.

In general, the viscosity and stability of the materials used cannot adapt to technology such as SLA. Another constraint is the thickness of the layers encountered in the scaffold, which is produced at the microlevel. There may be some residues in the layers polymerized with SLA, which is a micro-level problem. When an encapsulated group of cells is desired, the presence of ultraviolet light may cause cytotoxicity. Indirect SLA methods have been developed to overcome these limitations, but these methods are very expensive, take a long time, and require extra products [65].

FDM technology involves the printing of the desired 3D structure with an ongoing filament output. The basis of the technique is the heating of small beads or a polymer filament through a small tip, then hardening this material into a solid form. For this reason, the materials used generally show thermoplastic properties. With this technology, the thickness, width, angle, pore size, morphology, and interconnectivity of the material desired to be printed can be adjusted [66]. Due to these features, it is possible to produce 3D materials with complex structures, which are quite difficult to produce with traditional methods, with FDM technology. Thermoplastic materials such as poly(caprolactone) (PCL), PLA, PLGA can be used to make scaffolds for TE applications. These materials are melted using the melting temperatures they possess, the desired shape is given, and then they are solidified [54]. Many studies on the production of scaffolds have been started for use in bone regeneration using FDM technology [67–69]. The limitation of FDM technology, as with any method, is that the structure that can be produced must be in a specific way, or a standard structure. FDM technology has a low resolution compared to SLA because the melting of the material used prevents the desired resolution from being reached [54]. At the same time, the high temperatures that need to be removed to melt the material usually range from 120 to 300 ^{o}C, making it impossible to use cells or drugs with the scaffold [70].

In SLS technology, powder is sintered by a laser so that the material is combined and a solid structure is obtained. The treatment of small particles of a material such as thermoplastic, metal, or ceramic with a high power CO_2 or Nd:YAG laser forms the basis of the principle [18]. These parts combine with the laser applied to small particles. After the first layer is sintered, a new powder layer is laid, and this layer is treated with laser again. As each layer forms, a new layer of powder is laid, and this process is continued until the structure is complete [70]. Metallic scaffolds that can be used for BTE

applications can be produced with SLS technology [71]. When the polymer is chosen as the material, it does not require an organic solvent, which is also an advantage. Using SLS, composite scaffolds with mechanical properties similar to trabecular bone can also be printed. The main disadvantage of this technology is that the temperature rises significantly as a result of the laser intervention, so the cells cannot be added to the environment during production [72]. Another limitation is that the characteristic properties of the particles in the powder were used to affect the pore diameter of the scaffold [53].

In recent years, the use of 3D bioprinters has been increasing in regenerative medicine, especially in TE applications. With the possibilities that this technology brings, artificial implants and tissues can be printed in 3D with live cells, ECM, and other biomaterials that can be used simultaneously during this printing. In the field of BTE, these printers have started to be used frequently. The most important reason for this is that the cells used while printing scaffolds can be distributed evenly throughout the structure [73]. Various bioinks are being developed for bone regeneration. Today, 3D bioprinter devices can be used in three different ways. These are: inkjet-based bioprinting, extrusion-based bioprinting, and laser-based bioprinting [63].

The extrusion-based printing method is an improved version of the inkjet method. With this method, it is now possible to use viscous materials that cannot be used in inkjet printers. The basis of the technique is the use of an air pump or a mechanical screw plunger. With the help of this material, the bioink can be extruded from the cartridge. The ongoing power that gives the bioink its shape emerges as fibers rather than drops. The majority of currently available commercial bioprinters, such as the NovoGen 3D Bioprinting Platform (Organovo, San Diego, USA) and Bioplotter (EnvisionTec, Gladbeck, Germany), are based on extrusion technology [73].

1.2.3. Stimulating Factors

Various SFs are used to differentiate a precursor cell into the desired cell. With this differentiation, it is possible to create newly formed tissue. Since osteoblast cells are intended to be used in BTE, various methods have been used to transform the precursor cells into osteoblast lineages. These approaches could involve physical or biochemical content and are defined as "SF." The effect of SFs on cell differentiation is incredibly high.

Environmental characteristics of the implanted scaffold can change cell differentiation. When changing the material properties of the tissue scaffold, it can be modified in the transformation to the desired cell pathway too [74].

Biochemical stimulants can control effects such as cell migration, adhesion, and differentiation [75]. Although many materials are used as biochemical stimulants, the most frequently used are GFs. While the studies conducted with GFs can achieve very successful results *in vitro*, it was observed that the same success could not be achieved *in vivo*. For this reason, few of the studies have been able to get to the clinical stage. Even if it can be used in the clinic, the amount that should be used to affect the GFs is far above the physiological level. It is thought that this may cause side effects in the long term [76].

Small molecules are defined as substances with a molecular weight less than 1,000 daltons. It is able to direct and differentiate various cells to the osteoblastic pathway for use in BTE. Compared to GFs, it shows many advantages, such as easier production, stability, price, and effectiveness. Due to these advantages, it has been frequently preferred in recent years. There are some small molecules that have been found to be used in BTE. These molecules can activate various pathways that trigger bone formation and affect regeneration [74].

1.2.3.1. Growth Factors

When damage to the bone tissue occurs, a complex process involving different steps of recovery begins. Many cell types take part in this process. These cells can be referred to as inflammatory cells, vascular cells, mesenchymal precursor cells, and osteocytes. During these molecular pathways involved in healing, their production increases by stimulating inflammatory, angiogenic, and osteogenic GF [77]. GFs show their activity by binding to cell surface receptors. They upregulate or downregulate cellular activity. They can be counted in the transcription of various genes that are effective in growth and development, as well as in mechanisms influenced by GFs. GFs can not only increase cellular proliferation, differentiation, and adhesion but also reduce them [76].

The effect of GFs in TE studies covers an undeniable area. Fibroblast GFs (FGF), BMPs, vascular endothelial GF (VEGF), insulin-like GF (IGF), transforming GF-β (TGF-β), platelet-derived GF (PDGF), parathormone (PTH), parathormone-related protein (PTHrP), and Wnt proteins are examples of GFs commonly used in bone regeneration [78–80].

While these GFs can act alone, they can also be used in various combinations in some TE applications. While GFs can be delivered directly to the desired region, they can also be given indirectly through carrier systems [79]. BMP-2 and BMP-7 are the two most important GFs in BTE. Research is focused on these two GFs. These GFs, which are preferred in bone regeneration, also have FDA approval.

1.2.3.2. Small Molecules

The use of GFs in bone regeneration is a frequently used method as it positively affects bone formation. GFs, despite their benefits, have some limitations. These are: high production costs; shortness of half-life due to its instability; contamination problems that may occur due to the production of bacteria; and the possibility of causing immune responses. In order to prevent these problems, new approaches have been studied. In recent years, a multitude of new small molecules have been found for this purpose and included in the literature [14,81].

The use of small molecules can ensure bone regeneration. It has an advantage over GFs due to its effects, such as its use as a dose-dependent or prompt response because it provides a rapid effect [82]. Besides, it is easy to manufacture and cost-effective. The effects of small molecules can be reversible. It can be designed and synthesized in different forms for various therapeutic approaches. Since it is a material that is easy to study and access, it can be started more quickly in *in vivo* models. In addition, small molecules can be used to understand bone regeneration metabolism in detail. Despite all these advantages, it has some limitations or side effects. These can be said to have toxic effects when used in high doses or cause damage to other tissues and organs [83].

There are some basic signal pathways known for bone regeneration today. The main purpose of stimulation factors is to activate or inactivate these pathways. The most commonly used pathways in bone healing are Wnt/-catenin, BMP/TGF-, mitogen-activated protein kinase (MAPK), PDGF, IGF, FGF, and Notch [15]. By activating the transcription factors present in these signal pathways, bone regeneration can be controlled. Small molecules cannot be said to activate this mechanism directly. They act as auxiliary activators or inhibitors [83]. There are some small molecules used in bone regeneration like melatonin, purmophamine, and resveratrol [74]. There are also natural small molecules such as decalpenic acid, flavonoids, quinones, lipids, and synthetic small molecules such as

GSK-3 inhibitor, Wnt antagonist sFRP-1 inhibitor, DKK-1 inhibitor, and cathepsin K inhibitor [83].

DIPQUO

Cook et al. [84] discovered a new small molecule in 2019 among 47,000 compounds and identified a small-molecule activator of ALP, 6,8-dimethyl-3-(4-phenyl-1H-imidazol-5-yl)quinolin-2(1H)-one (DIPQUO), which promotes and accelerates osteoblast differentiation and maturation *in vitro* and *in vivo* (Figure 1.8). As part of the DIPQUO signal pathway, the β isoform p38 acts on MAPK and increases the activity of this pathway. In this way, it is thought that it can be used in skeletogenesis studies. When DIPQUO is optimized, it is predicted that it may have various therapeutic effects. The MAPK-extracellular signal-regulated kinase pathway acts as a bridge between the cell surface and the nucleus. This signal pathway regulates cell proliferation, differentiation, and death [85,86]. In addition, the MAPK pathway can cross-talk with various molecular pathways. In this way, it has an important effect on bone formation. The MAPK pathway can activate GFs or various adhesion molecules by stimulating various signals during bone regeneration. Examples of these molecules are EGF, FGF, IGF α2, and α5 integrins [15]. DIPQUO's mechanism for osteoblast differentiation and maturation is the p38 MAPK pathway. It activates the p38- β pathway and provides osteogenesis.

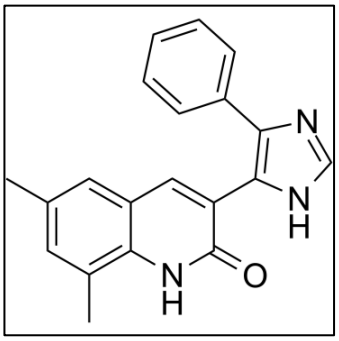


Figure 1.8 Molecular structure of DIPQUO [84]

The osteogenic effect of DIPQUO is quite strong. DIPQUO promotes progenitor cell differentiation and participates in calcium storage. It participates in notochord formation and stimulates osteoblast formation for new bone tissue.

GS4012

Today, zebrafish are often used for various modeling studies. Zebrafish chemical imaging is also used to investigate the effectiveness of small molecules. In 2004, the study was carried out by applying this method again in zebrafish, and a new small molecule called GS4012 was found that provides vascularization (Figure 1.9). The GS4012 upregulates VEGF, the main factor in vascularization, by allowing to pass through the cell membrane. GS4012 is a pyridinyl-thioether compound molecule. It activates VEGF by blocking the extracellular signal-regulated kinase (ERK) pathway [87]. In the study, human umbilical cord vein endothelial cells were used, and it was observed that tube formation increased with the increase of VEGF expression [88]. When the genes involved in angiogenesis are examined, it is seen that the mechanism of action of GS4012 is by increasing the expression of VEGF [89,90].

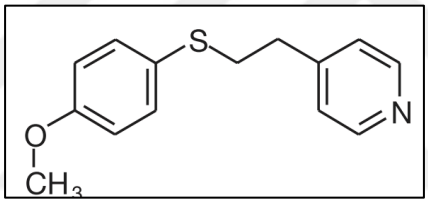


Figure 1.9 Molecular structure of GS4012 [88]

VEGF is the most effective GF in vascular development and angiogenesis. Angiogenesis is an indispensable factor for osteogenesis since bone tissue has a normally highly vascularized structure, so cells are easily nourished. Therefore, VEGF is also important for bone regeneration. The effect of VEGF on bone regeneration is not only related to vascular formation but can also be involved in bone formation. VEGF is involved in the differentiation of stem cells in the bone marrow into the desired cell line. When the VEGF level in the environment decreases, MSCs may differentiate into adipogenic cells, which are not desired for bone regeneration [91,92].

1.2.3.3. Nanoparticles

Since SF delivery is important in many ways, various researches have been made in this area, and some methods have been developed. These methods are the physical trapping of SF into the scaffold, ensuring a covalent bonding with the scaffold, and using micro or nanoparticles (NPs) as carriers (Table 1.2). A wide range of delivery methods have been

developed for SFs of various molecular structures [93]. One of the delivery methods is to establish a bond between the surface of the scaffold and SF through the reactive groups found. Accordingly, SF should be modified, and a reactive group should be added [94]. With this method, a slow release can be achieved by staying longer on the SF scaffold, while at the same time, the side effects of a sudden release are prevented [95]. The release usually takes place by hydrolysis, reduction reactions, or enzymatic factors. Although the benefits of this method are intriguing, the method's long time requirement, increased workload, and high cost limit its use. In addition, the region to which the modified SF covalent bond binds can limit the activation of the protein and therefore reduce its effect [94]. With non-covalent bonding, another method of delivery, SFs are physically trapped inside the scaffold structure. For this, physical encapsulation, protein adsorption, or ionic interactions can be used. With these methods, SF is immobilized in the 3D matrix structure. However, in this method, it is very difficult to control since the release rate depends on diffusion, and accordingly, burst release can occur [96]. Another and final method of SF delivery is to combine NPs with scaffold. By integrating SFs into NPs, a highly controlled release can be achieved, and long-term release profiles can be provided depending on the desired application area [97]. The NPs to be produced can be synthesized with various natural or synthetic materials and using different methods [93]. While PLA, PCL, PEG, PLGA, PHBV, and PLL can be used synthetically, it has been observed that albumin, alginate, silk fibroin, hydroxyapatite, chitosan, and arabic gum are used naturally [93,98]. With various combinations of these materials, it covers the scaffold surface and makes the SF release controlled. Among the materials used as SF carriers, chitosan stands out as a natural material. The advantages obtained with chitosan NPs and chitosan composite NPs have been proven by studies in the literature [97,99–103]. There are many advantages to using NPs. It is known that mechanical strength is very important in BTE. Mechanical properties can be improved with the help of nanotechnological approaches. According to some studies, adding NPs to scaffolds increased their mechanical strength [104].

The use of NPs creates an environment that enhances the adhesion and proliferation of cells. By mimicking natural bone surrounding tissue, it improves osteointegration, osteoconduction, and osteoinduction [105]. NPs are small in size, so they have a large surface area. It maintains the effectiveness of the loaded material. The degradation of SFs

in the NPs by enzymes *in vivo* environment is prevented, and long-term protection is provided [77]. It is possible to control the release rate, which usually depends on the size of the particle [93]. It is possible to release more than one molecule by using micro- or NPs. However, the production of NPs means extra production steps, and sometimes chemical materials can be used during their production. However, due to all the advantages it provides, the use of NPs is very important in SF delivery [93].

Table 1.2 Advantages and disadvantages of SF delivery [93]

	Advantages	Disadvantages
Covalent binding	No SF diffusion out of scaffold	Loss of SF bioactivity
Non-covalent binding	Maintained SF bioactivity	Diffusion and degradation mediated release Rapid burst release Difficult to control release rate
Micro/nanoparticle	Better control of SF release rate Possibility for sequential release of multiple SFs	Additional fabrication steps Usage of harsh chemicals

In this study, it was aimed to use a PLA scaffold, which was produced with a 3D printer, for bone regeneration. The MSCs were isolated from rat bone marrow (rBM) and then seeded into scaffolds produced. For angiogenesis, GS4012, and for osteogenesis, DIPQUO, small molecules were encapsulated in chitosan NPs, and the cells differentiated into bone tissue by controlled release. The osteogenic capability of these TE constructs was investigated throughout the research.

With this study, bone-like tissue, which is the most important step in BTE studies, was created, and in that way, the failure rate associated with inadequate vascularization will be reduced, the healing process of bone damage will be accelerated, and the patient's recovery period will be shortened. In addition, with this BTE design, the need for implants and prostheses, which we are dependent on abroad, will be reduced, and this will contribute economically to our country.

2. MATERIALS

2.1. CHEMICALS

- Acetic acid (27225, Sigma-Aldrich)
- Chitosan (CS, Deacetylation degree of 75-85% and medium molecular weight, 448877,Aldrich)
- Crystal Violet (C3886, Sigma)
- DAPI (D9542, Sigma)
- Dexamethasone (18660, Serva)
- Dil-Ac-LDL (L3484, invitrogen)
- DIPQUO (HY-128591, MedChemExpress)
- DMEM (1X, with high glucose + GlutaMAXTM, Gibco, USA)
- DMEM (1X, with low glucose + GlutaMAXTM, Gibco, USA)
- Dulbecco's Phosphate Buffer Saline (DPBS, 14190-094, Gibco, Germany)
- EGM^{TM}-2 MV Microvascular Endothelial SingleQuotsTM (CC-4147, Lonza)
- Endothelial Cell Growth Basal Medium (EBM-2, CC-3156, Lonza)
- Fetal Bovine Serum (FBS, 10500-064, Gibco, Germany)
- Formaldehyde (15512, Riedel-de Haen)
- Goat anti-mouse IgG (A11001, invitrogen)
- GS4012 (676491, Sigma-Aldrich)
- Histopaque 1083 (10831, Sigma)
- IBMX (sc-201188A, ChemCruz)

- Indomethacin (sc-200503A, ChemCruz)
- Insulin (19278, Sigma)
- ITS premix (354352, Corning)
- L-ascorbic acid 2-phosphate (113170-55-1, Sigma)
- L-proline (147-85-3, Sigma)
- N-(3-dimethylaminopropyl)-N-ethylcarbodiimide (EDC, 39391, Aldrich)
- Na-pyruvate (P2256, Sigma)
- Oil red O dye (O0625, Sigma)
- PE mouse anti-rat CD31 (555027, BD Pharmingen)
- Penicillin-Streptomycin (Sigma-Aldrich Corporation, Germany)
- Poly lacric acid (PLA, Ultrafuse, white, 1,248 kg/m3, 1.75 mm, BASF; Luminy LX175, Corbion, Netherlands)
- Prolong Diamond Antifade Mountant (P36961, invitrogen)
- Proteinase K (P6556, Sigma)
- Sodium hydroxide (NaOH, B0311362, Merck)
- Sodium tripolyphosphate (TPP, Mw= 367.86, 72061, Sigma-Aldrich)
- Transforming growth factor beta (TGF-β, PRP100190, Abbkine)
- Triton X-100 (TB0198, BioBasic)
- Trypsin-EDTA (Sigma-Aldrich Corporation, Germany)
- Tween 20 (P9416, Sigma)
- β-glycerophosphate (36002191, AppliChem)

2.2. KITS

- Alcian Blue Stain (RRSK6, Atom Scientific)
- Alizarin Red Solution (2003999, Merck)
- Cell Proliferation CellTiter 96® Aqueous One Solution Assays (G3581, Promega)
- easy-spin™ Total RNA Extraction Kit (17221, intron)
- *in Vitro* Angiogenesis Assay (ECM630, Merck)
- iScript cDNA Synthesis Kit (1708891, BioRad)
- Live-Dead Viability-Cytotoxicity (L3224, ThermoFisher Scientific)
- Maxima SYBR Green qPCR Master Mix (K0252, ThermoScientific)
- PicoGreen Assay (Quant-iT™ PicoGreen® dsDNA Assay Kit, Thermo Fisher Scientific, Waltham, MA, USA)
- QuantiChromTM Calcium Assay Kit (DICA-500, BioAssay Systems)
- Rat Gla-Osteocalcin High Sensitive EIA Kit (MK126, Takara)
- Rat Glu-Osteocalcin High Sensitive EIA Kit (MK146, Takara)
- Red Fluorescent Cell Linker Kit (PKH26GL, Sigma-Aldrich)
- SIGMA*FAST*™ p-nitrophenyl phosphate tablets (N2770, Sigma–Aldrich)
- von Kossa Kit (Diagnostic Biosystems, KT028-IFU, USA)
- VybrantTM DiO Cell-labeling Solution (V22886, invitrogen)

2.3. CD MARKER ANTIBODIES

- CD29 (BD Pharmingen, USA)
- CD34 (Novus Biological, USA)

- CD45 (BDPharmingen,USA)
- CD90 (BDPharmingen,USA)

2.4. INSTRUMENTS

- 24 deep-well Cell Culture Plates (ThinCert ™ Multiwell Plates, Greiner Bio One, Germany).
- 8.0 µm ThinCert™ Inserts (Greiner Bio One, Germany)
- Brightfield Microscope (TS100 Eclipse, Nikon)
- Centrifuge (Rotofix 32A, Hettich)
- CFX96 Touch™ Sequence Detection System (Bio-Rad, USA)
- CO_2 Incubator (CCL-170B-8, ESCO)
- Contact Angle Measurement System (CAM100, KSV Instruments, Helsinki, Finland)
- Countess II FL Automated Cell Counter (Thermo Fisher Scientific, USA)
- DSC131 (Setaram, KEP Technologies, France)
- Elisa Plate Reader (VarioSkan Lux, Thermo Scientific)
- Flow Cytometer (FACSCalibur, BD Biosciences)
- Fluorescence Microscope (VertA1, Zeiss, Germany)
- Freeze-dryer (Thermo Savant MODULYOD230, USA)
- Inverted Microscope (VertA1, Zeiss, Germany)
- Laminar Flow Cabinet (AC2-4E 8, Sentinal Gold, ESCO)
- Magnetic Stirrer (MSH-20D, Wisd)
- Mechanical Analyzer (Instron Universal Testing System 5966, USA)

- Nanodrop Spectrophotometer (Nanodrop 2000, Thermo Scientific, USA)
- Nicolet iS50 FT-IR Spectrophotometer (Thermo Scientific)
- pHmeter (HI2002, Hanna)
- Refrigerated Centrifuge (3-18KS, Sigma)
- Scanning Electron Microscope (Zeiss EVO40, Germany)
- Shaking Water Bath (WNB 14, Memmert)
- Sputter Coater (Leica EM ACE200)
- TEM (JEM 2100PLUS)
- Zaxe X1 3D Printer (Istanbul, Turkey)
- Zetasizer Nano ZS (Malvern Instruments)

3. METHODS

3.1. PLA SCAFFOLD PREPARATION AND CHARACTERIZATION

3.1.1. Design and Fabrication of PLA Scaffold

Within the scope of the study, scaffold production was carried out using two different PLA filaments. One of them is the commercial filament of the brand BASF (Ultrafuse, white, 1,248 kg/m^3, 1.75 mm). The other polymer, PLA Corbion (Luminy LX175) polymer beads, was converted into filament form using a twin screw extruder.

Ultrafuse PLA filament was used to fabricate scaffolds with a Zaxe X1 3D printer (Istanbul, Turkey). A three-dimensional cylinder model with a diameter of 10 mm and a height of 2.5 mm was used in .stl format. The scaffold was sliced into 42 layers with a layer thickness of 0.05 mm. Its interior design was determined to be a 0°/90° crosshatch pattern. The internal fill rate of the scaffold selected with Xdesktop software v2.1.6 of the device was determined as 50, 60, 70, 80, and 90%, and scaffolds with five different pore sizes were printed in that way (Figure 4.1A). The melted PLA was extruded through a nozzle with a diameter of 0.4 mm, while the printing temperature was set to 210 °C and the printing plate was heated to 60 °C.

After the optimum pore size was determined as 60%, the work was continued with the PLA filament of the Corbion brand under the same conditions, and scaffold production was made.

3.1.2. Characterization of Scaffold

3.1.2.1. SEM

The morphological analysis of the 3D-printed PLA scaffolds was examined using a scanning electron microscope (SEM, Carl Zeiss EVO, Germany) to evaluate the architecture and surface morphology. The scaffolds were coated with gold (Sputter Coater,

Baltec SCD 005, Germany) and imaged under a vacuum at 2 kV voltage. ImageJ (NIH, USA) software was used to calculate the diameter of the pores.

3.1.2.2. Fourier Transform Infrared Spectrophotometer (FT-IR)

Chemical characterization of PLA was performed via the Nicolet iS50 FT-IR spectrophotometer (Thermo Scientific). The device was set with a resolution of 4 cm^{-1} and a frequency range of 4,000–400 cm^{-1}. The data were processed using OMNIC software (ThermoFisher Scientific Inc.).

3.1.2.3. Differential Scanning Calorimetry (DSC)

DSC was performed to determine the glass transition and thermal energy at the printing temperature by using DSC131 (Setaram, KEP Technologies, France) to obtain the potential printing temperature range. Before and after the printing, PLA (10 mg) was accurately weighed and sealed in aluminum pans. The thermogram was recorded in a range of 20–210 °C with a heating rate of 10 °C/min under nitrogen gas. The resulting DSC curves were analyzed to determine the glass transition (T_g) temperature, crystallinity (X_c), and melting temperature (T_m) of the polymer.

3.1.2.4. Contact Angle Measurement

The surface hydrophilicity of the samples was investigated by a contact angle measurement system (CAM100, KSV Instruments, Helsinki, Finland) at RT. The water droplets were placed on three different scaffolds for each specimen. The analysis of the contact angle was done with the Attention Theta program. All experiments were measured in triplicate for each of the samples.

3.1.2.5. Mechanical Analysis

The compressive and tensile strengths of the 3D-printed PLA scaffolds were determined using a mechanical analyzer (Instron Universal Testing System 5966, USA) with a 10 kN load cell for compression analysis and a 1 kN load cell for tensile analysis. Without preloading, the samples were analyzed at a speed of 1 mm/min^{-1}. Stress–strain data were obtained from load–displacement measurements. All experiments were measured in triplicate for each of the samples.

The compressive modulus was determined using the slope of the drawn stress–strain curve. For each scaffold, three cylindrical scaffolds (10 x 10 x 2.5 mm^3) were analyzed. The

actual dimensions of the scaffolds printed in 3D were measured with a caliper before the test.

The dog bone shape file was designed in. stl format, similar to those used in the literature, and printed with different fill rates for tensile stress analysis. The tensile modulus was also determined using the slope of the stress–strain curve. For each scaffold, three dog-bone-shaped scaffolds (84.56 x 13.97 x 2.5 mm^3) were tested. The actual dimensions of the scaffolds printed in 3D were measured with a caliper before the test.

3.1.2.6. In vitro Degradation Analysis

The scaffolds were placed in 5 mL of PBS (0.09% sodium azide in 10 mM D-PBS, pH 7.4; Sigma–Aldrich, St. Louis, MO, USA) and shaken at 37 °C at 80 rpm for *in vitro* degradation. The original weight of each scaffold was recorded. The PBS solution was not renewed to follow the pH changes. The pH values of the PBS solution were measured after 3, 7, 15, 30, 60, 90, 120, and 150 days to observe the effect of degradation on pH. Afterward, scaffolds were removed from the solutions at the same time points, dried with filter paper, and then their weights were measured on the balance scale. After measuring the wet weight, the scaffolds were frozen at -80 °C and then lyophilized (Thermo Savant MODULYOD230, USA) to determine the dry weight. All experiments were measured in triplicate for each sample. Since no change was observed in *in vitro* degradation, an enzymatic degradation study was also performed.

The enzymatic degradation profile of the PLA scaffolds was analyzed. Scaffolds were weighed and incubated in the 24 well plates containing 0.05 M Tris–OH buffer solution (pH 8.6), 0.2 mg/mL of proteinase K, and 0.2 mg/mL sodium azide. The enzymatic degradation analysis was carried out in the water bath at 37 °C at 100 rpm. The enzymatic degradation solution was changed each day to obtain the enzymatic activity at a high level. On the 5^{th} and 10^{th} days, the samples were freeze-dried, and their weights were recorded. Also, changes in the pH were determined at each time point. All experiments were measured in triplicate for each sample.

3.2. NANOPARTICLE PREPARATION AND CHARACTERIZATION

3.2.1. Preparation of Nanoparticles

Chitosan NPs were synthesized by Calvo's ionic gelation method. With this method, chitosan NPs containing no material (blank) (NP), osteogenic factor DIPQUO loaded (D-NP), angiogenic factor GS4012 loaded (G-NP), and these two small molecules dually loaded (DG-NP) were synthesized (Table 3.1).

For blank CS-NP synthesis, TPP was added dropwise to the chitosan solution. The chitosan:TPP mass ratio was adjusted to 3.33, the pH of the medium was adjusted to 4.8, and the study was continued for 30 mins at 400 rpm on a magnetic stirrer.

For GS4012-loaded NP synthesis, GS4012 was directly added to the chitosan solution and mixed for 30 mins for homogenous distribution. For DIPQUO-loaded NP synthesis, DIPQUO was added to the chitosan solution containing 0.1% Tween 20 to form a complex and mixed for 30 mins for homogeneous distribution. Finally, TPP was added to those mediums for NP synthesis. For the dual encapsulation study, DIPQUO was added to the chitosan solution containing 0.1% Tween 20, and then GS4012 and TPP complex were added dropwise to this mixture on the magnetic stirrer to form NP (Figure 3.1).

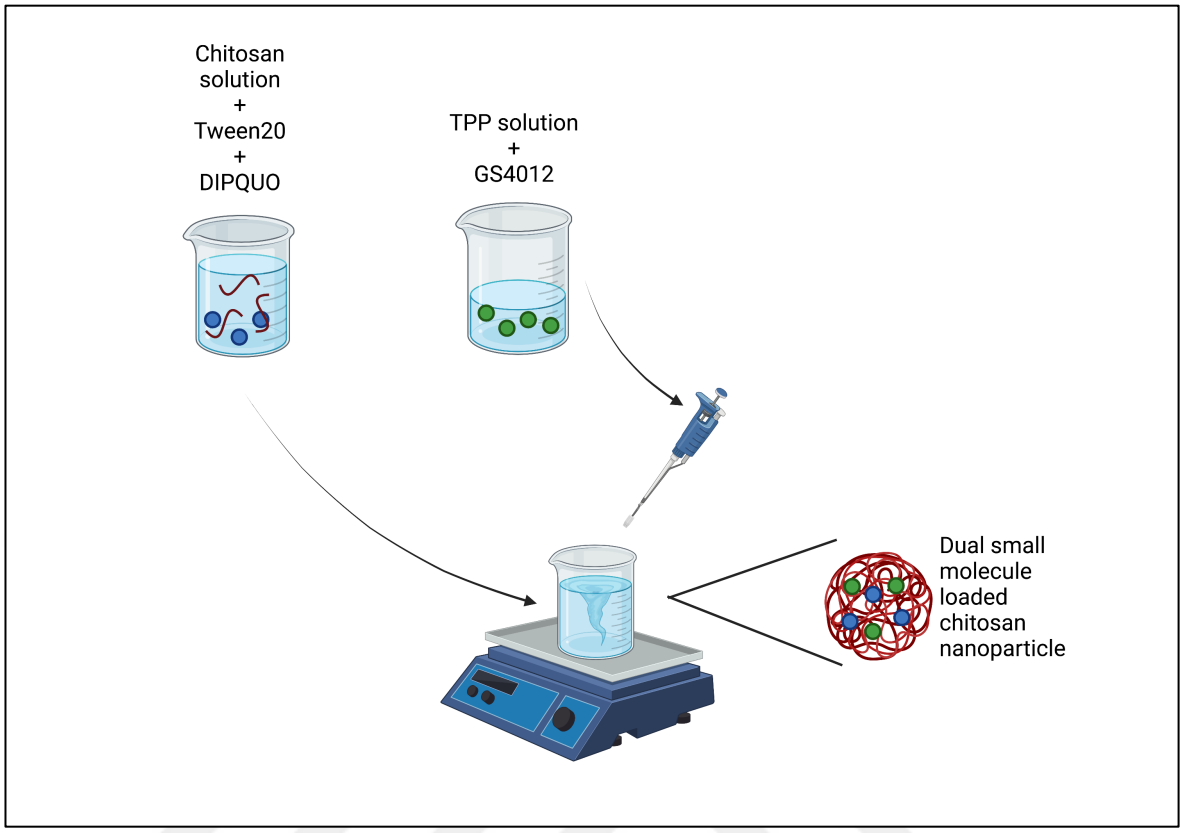


Figure 3.1 Schematic representation of dual small molecule loaded chitosan nanoparticle synthesis. Created with BioRender.com

After the synthesis, the NP solution was centrifuged at 13,000 rpm at +4 °C for 30 mins. After the supernatant was removed, the same process was repeated several times for washings. Finally, the pellet was freeze-dried at -80 °C and stored for further analysis.

Table 3.1 NP synthesize conditions.

Sample	CS:TPP mass ratio	Magnetic Stirrer	Sonicator	BSA (mg/mL)	β-cyclodextrin (mg)	Tween 80 (μl)	Tween 20 (μl)	DIPQUO (μM)	GS4012 (μg/mL)
NP1	1.67	30 min-500 rpm	50W-5 min						
NP2	2.50	30 min-500 rpm	50W-5 min						
NP3	3.33	30 min-500 rpm	50W-5 min						
NP4	5.00	30 min-500 rpm	50W-5 min						
NP5	10.00	30 min-500 rpm	50W-5 min						
NP6	3.33	30 min-400 rpm							
NP7	3.33	30 min-400 rpm							
NP8	3.33		50W-5 min						
B-NP1	3.33	30 min-400 rpm		1					
B-NP2	3.33	30 min-400 rpm		3					
B-NP3	3.33	30 min-400 rpm		5					
B-NP4	3.33	30 min-400 rpm		10					
D-NP1	3.33	30 min-400 rpm	50W-5 min					10	
D-NP2	3.33	30 min-400 rpm	50W-5 min			50		10	
D-NP3	3.33	30 min-400 rpm	50W-5 min				50	10	
D-NP4	3.33	30 min-400 rpm	50W-5 min		7.5	50		10	
D-NP5	3.33	30 min-400 rpm	50W-5 min		7.5		50	10	
D-NP6	3.33	30 min-400 rpm	50W-5 min			50		10	
D-NP7	3.33	30 min-400 rpm						10	
D-NP8	3.33	30 min-400 rpm				50		10	
D-NP9	3.33	30 min-400 rpm					50	10	
D-NP10	3.33	30 min-400 rpm			7.5	50		10	
D-NP11	3.33	30 min-400 rpm			7.5		50	10	
D-NP12	3.33	30 min-400 rpm					100	10	

D-NP13	3.33	30 min-400 rpm					25	10	
D-NP14	3.33	30 min-400 rpm					12.5	10	
D-NP16	3.33	30 min-400 rpm					50	5.5	
G-NP1	3.33	30 min-400 rpm							2.5
G-NP2	3.33	30 min-400 rpm							5
G-NP3	3.33	30 min-400 rpm							10
G-NP4	3.33	30 min-400 rpm							15
G-NP5	3.33	30 min-400 rpm							20
G-NP6	3.33	30 min-400 rpm							25
DG-NP1	3.33	30 min-400 rpm					25	10	15
DG-NP2	3.33	30 min-400 rpm					50	10	15
DG-NP3	3.33	30 min-400 rpm					25	10	5
DG-NP4	3.33	30 min-400 rpm					25	10	10
DG-NP5	3.33	30 min-400 rpm					50	10	10
DG-NP6	3.33	30 min-400 rpm					50	10	5
DG-NP7	3.33	30 min-400 rpm					25	5	15
DG-NP8	3.33	30 min-400 rpm					25	5	20
DG-NP9	3.33	30 min-400 rpm					25	5	25
DG-NP10	3.33	30 min-400 rpm					50	5.5	15
DG-NP11	3.33	30 min-400 rpm					50	5.5	20
DG-NP12	3.33	30 min-400 rpm					50	5.5	25

NP:blank CS NP
B-NP: BSA loaded CS NP
D-NP: DIPQUO loaded CS NP
G-NP: GS4012 loaded CS NP
DG-NP: DIPQUO and GS4012 loaded CS NP

3.2.2. Characterization of Nanoparticles

3.2.2.1. Zeta-sizer

Zetasizer Nano ZS (Malvern Instruments) was used for the characterization of particle size, zeta potential, and polydispersity index (PDI) of blank and loaded NPs. The dynamic light scattering (DLS) technique was used to calculate the average size of CS NPs. NP solution was loaded directly into the disposable cuvette of the Zetasizer ZEN0040.

3.2.2.2. TEM

TEM (JEM2100 PLUS) was used to determine the morphological characteristics of NPs. For TEM analysis, one drop of freshly prepared NPs was dropped onto the grid and the liquid part evaporated at RT.

3.2.2.3. FT-IR

Chemical characterization of NPs was performed via the Nicolet iS50 FT-IR spectrophotometer (Thermo Scientific). The device was set with a resolution of 4 cm^{-1} and a frequency range of 4,000–400 cm^{-1}. The data were processed using OMNIC software (ThermoFisher Scientific Inc.).

3.2.2.4. DSC

NPs heat capacity changed by temperature was determined using DSC131 (Setaram, KEP Technologies, France). The phase behavior of CS, TPP, Tween 20, blank NP, D-NP, G-NP, and DG-NP was recorded. About 5 mg of samples for each were accurately weighed and sealed in an aluminum pan. A thermogram was taken with a temperature range of 25-300 °C and a heating rate of 10 °C/min. The resulting DSC curves were analyzed to determine the glass transition (T_g) temperature, crystallinity (X_c), and melting temperature (T_m) of the polymer.

3.2.2.5. Evaluation of NP Yield Analysis

The reaction yield (RY) analysis of the CS NPs was determined by a gravimetric method. The CS-NP suspension was centrifuged at +4 °C and 13,000 rpm for 30 min in a high-speed centrifuge (3-18 KS, Sigma, Germany) with a 50-mL falcon tube. The supernatant was removed, the pellet was washed several times, and the remaining pellet suspensions

were lyophilized (Savant Modulyo, Thermo Scientific). Fully dried NPs were weighed on a precision scale. The yield was calculated using the following equation (3.1).

$$RY\ (\%) = \frac{weight\ of\ nanoparticles}{total\ weight\ of\ solids} \times 100 \quad (3.1)$$

3.2.2.6. Evaluation of NP Encapsulation Efficiency and Loading Capacity

The encapsulation efficiency (EE) and loading capacity (LC) of the CS NPs were measured using the supernatant collected after centrifugation of the NPs.

The absorbance value of the obtained supernatants was measured at their specific absorbance values. For this purpose, spectrum scanning was performed for DIPQUO and GS4012 molecules. Specimens were prepared by dissolving them in their own solvents and placing them in quartz cuvettes, and spectrum scanning was performed at all wavelengths. With the graphs drawn with the received data, the peak points of the samples were determined as absorbance values. The EE and LC were calculated using the equation (3.2) and (3.3).

$$EE\ (\%) = \frac{total\ BSA/small\ molecule\ amount - BSA/small\ molecule\ amount\ in\ supernatant}{total\ BSA/small\ molecule\ amount} \times 100 \quad (3.2)$$

$$LC\ (\%) = \frac{total\ BSA/small\ molecule\ amount - BSA/small\ molecule\ amount\ in\ supernatant}{weight\ of\ nanoparticles} \times 100 \quad (3.3)$$

3.2.2.7. In vitro Release Study of the CS Nanoparticles

For *in vitro* release study, CS NP was put in a beaker that contains 3 mL PBS with 0.01% sodium azide (pH 7.4) solution. The sample was sonicated and placed on a dialysis membrane (Molecular weight-cutoff (MWCO): 14 kDa, MC18, Membra-cel Dialysis membrane, Viskase). The dialysis membrane was placed in a beaker containing 17 mL of PBS. The temperature of the shaking water bath was adjusted to 37 °C, and agitation was started at 100 rpm. Samples were withdrawn at specific time intervals, and the same volume of fresh PBS solution was replaced each time. The concentrations were determined by UV spectrophotometry. A calibration curve was plotted with known concentrations of DIPQUO and GS4012 at the appropriate wavelength to determine the amount of small molecule released.

3.2.3. Determination of Half-Maximum Inhibitory Concentration

In order to determine the half-maximum inhibitory concentration (IC50) value of the small molecules to be used in the study, 160 μM of DIPQUO and 160 mg/mL of GS4012 were prepared, diluted in descendent concentrations, and added to 5,000 cells seeded in a 96-well plate. At the end of 24 and 48 h, the viability of the cells that were exposed to these small molecules was determined by MTS.

The IC50 values of small molecules were calculated by using the log (small molecule concentration) vs. normalized response-variable slope analysis for the non-linear fit using Prism 8.0 (GraphPad Software, San Diego, CA, USA).

3.3. NP COATING OF SCAFFOLDS

The synthesized NPs were coated on the surface of PLA scaffolds printed with a 3D printer. Within the scope of the study, more than one method was tried for coating. These include: EDC bonding to the scaffold surface; surface etching with acetone-water mixture; adding NPs directly to the scaffolds; drying the scaffolds mixed with NPs by a magnetic stirrer in a desiccator or freeze-dryer; and treatment with alkaline methods. As a result of the preliminary studies, it was decided to proceed with alkali treatment. With this method, PLA, an inert material, was modified and OH-groups were attached to its surface. In the study, scaffolds were treated with NaOH by choosing 2 different concentrations (0.5 and 1.25 M) and times (2 and 4 h). These scaffolds were coated with NPs either by mixing them on a magnetic stirrer and then air-drying them or by adding the NPs directly and drying them in a vacuum desiccator.

All experimental groups and conditions used in the study are given in Table 3.2.

Table 3.2 Experimental groups used in the study.

Sample	Conditions
Untreated	Empty PLA scaffold
Uncoated	Alkali treated PLA scaffold
Blank coated	Alkali treated PLA scaffold + CS NP

D-NP coated	Alkali treated PLA scaffold + D-NP
G-NP coated	Alkali treated PLA scaffold + G-NP
DG-NP coated	Alkali treated PLA scaffold + DG-NP

3.4. *IN VITRO* CELL CULTURE STUDIES

3.4.1. Isolation and Characterization of rBMSCs

Rat bone marrow MSCs (rBMSCs) were isolated from the bone marrow of 6–8-week-old Sprague-Dawley rats. The animal was put into an anesthesia chamber and anesthetized for around five mins. The rats' femoral and tibial bones were separated from their back limbs, and then the skin and muscles were removed. The bones were placed in a medium containing 10% penicillin-streptomycin (10,000 U/mL) (DMEM (1X) with low glucose and GlutaMAX^{TM}, Gibco, USA). The bones were cut open from two ends with a scissor, and the bone marrow was ejected with the help of a sterile syringe in a laminar flow cabinet (ESCO). The extracted bone marrow was centrifuged at 1,800 rpm for 5 mins. The pellet was dissolved in the growth medium (GM) (DMEM (1X) and GlutaMAX^{TM} with 10% fetal bovine serum (FBS), 100 units/mL penicillin, and 100 units/mL streptomycin) and incubated at 37°C, 5% CO_2, and 90% humidity in an incubator. The culture medium of the rBMSCs was changed every three days. The study protocol was reviewed and approved by the Yeditepe University Ethics Committee for Experimental Animal Use.

In order to prove that the isolated cells were MSCs, the multipotent differentiation potential of the cells was determined. For this, three different differentiation media were prepared, and the differentiation of cells was characterized with various dyes. Cells were seeded at a concentration of 2 x 10^4 cells in each well of 24-well plates. After the cells were kept in GM for 3 days, either GM or differentiation medium was changed according to the determined groups, and studies were continued for 7, 14, and 21 days for each group.

3.4.1.1. Osteogenic Differentiation

For osteogenic differentiation, Dulbecco's Modified Eagle Medium (DMEM) with low glucose content, containing 100 nM dexamethasone, 10 mM β-glycerophosphate, 50 μg/mL ascorbic acid, 10% FBS, and 100 u/mL penicillin-streptomycin, was prepared, and the GM of the cells was replaced with this osteogenic medium (OM).

Calcium deposits were shown by von Kossa staining at the determined time points. First, the cells were washed twice with PBS and fixed in a 3.7% formaldehyde solution at RT for 45 mins. Staining was performed with the modified von Kossa kit (Diagnostic Biosystems, KT028-IFU, USA). Silver nitrate (5%) was added to the wells and kept under UV light for 30 to 60 mins. After the washing steps, a 5% sodium thiosulfate solution was added, waited for 2–3 mins, and then washed under running tap water for 2 mins. Finally, nuclear fast red solution was added, waited for 5 mins, and washed until the redness disappeared. Images were taken under an inverted microscope.

Alizarin red solution (Merck) was used to stain calcium-containing osteocytes. This solution was added to the fixed cells and left at RT for 45 mins. Images were taken under an inverted microscope after washing steps.

3.4.1.2. Chondrogenic Differentiation

For chondrogenic differentiation, DMEM with high glucose content, containing 1% ITS premix, 100 nM dexamethasone, 50 μg/mL L-ascorbic acid 2-phosphate, 40 μg/mL proline, 10 μg/mL Na-pyruvate, 10 ng/mL TGF-β and 100 u/mL penicillin-streptomycin, was prepared, and the GM of the cells was replaced with this chondrogenic medium (CM).

Alcian blue stain kit (Atom Scientific) was used to stain acidic mucopolysaccharides. Alcian blue stain was added to the fixed cells, and incubated for 10 mins. Periodic acid dye (1%) was added to the cells, which were washed with distilled water, and waited for 5 mins. After washing, Schiff reagent was added, and 20 mins were allowed to pass. The wells were washed under running water until the color turned magenta. Images were taken under an inverted microscope.

3.4.1.3. Adipogenic Differentiation

For adipogenic differentiation, DMEM with high glucose content, containing 1 μM dexamethasone, 100 μM indomethacin, 500 μm IBMX, 10 μg/mL insulin, 10% FBS, and

1% penicillin-streptomycin, was prepared, and the GM of the cells was replaced with this adipogenic medium (AM).

Oil-red-O dye (Sigma) was used to stain lipids in differentiated cells. Isopropanol (60%) was added to the fixed cells for 5 mins before being pulled out of the wells to dry at RT. After 30 mins, the Oil-red-O solution was added. The wells were thoroughly washed. Images were taken under an inverted microscope.

3.4.1.4. Flow Cytometry Analysis

The immunophenotypic characterization of the cells was achieved through flow cytometry analysis. To confirm their mesenchymal origin, the cells were tagged with unique cell surface markers. CD29 (BD Pharmingen, USA) and CD90 (BDPharmingen, USA) were chosen as positive markers, while CD34 (Novus Biological, USA) and CD45 (BDPharmingen, USA) were chosen as negative markers.

3.4.2. Isolation and Characterization of rPBECs

Endothelial cells were isolated from the peripheral blood of 6–8-week-old Sprague-Dawley rats. Histopaque 1083 (Sigma) was used to isolate mononuclear cells from blood. The blood taken from the hearts of the rats was put into blood tubes containing EDTA to prevent coagulation. The collected blood was diluted with the same amount of PBS (15 mL) and added slowly to the falcon containing histopaque (15 mL), not allowing them to mix with each other (Figure 3.2a). At RT, it was centrifuged at 400 x g for 30 mins. After centrifugation, the opaque interphase layer containing mononuclear cells was transferred to a new falcon (Figure 3.2b). The cells were centrifuged at 250 x g for 10 mins after being thawed in PBS (15 mL). The supernatant was removed, the cells were resuspended in 5 mL of PBS, and they were centrifuged again at 250 x g for 10 mins. The supernatant was removed, and the washing steps were repeated. Cells were transferred to a T25 flask that was coated with collagen type 1. Cells incubated at 37°C with 5% CO_2 and 90% humidity in an incubator. The endothelial cell growth basal medium (EBM-2, Lonza) was completed with EGM™-2 MV Microvascular Endothelial SingleQuots™ (Lonza) added to flasks. Rat peripheral endothelial cells's (rPBECs) medium was changed every three days. The study protocol was reviewed and approved by the Yeditepe University Ethics Committee for Experimental Animal Use.

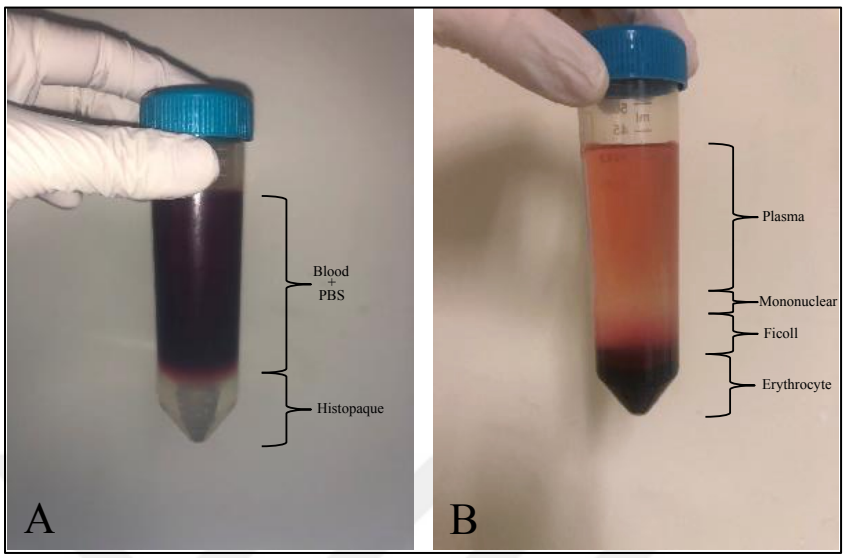


Figure 3.2 Isolation of endothelial cells from rat peripheral blood (A) before and (B) after centrifugation.

3.4.2.1. CD31 (PECAM-1)

rPBECs were seeded in 48-well plates at a density of $2x10^4$. Staining was performed two days later. Briefly, after the cells were washed with PBS, they were incubated in a 3.7% formaldehyde solution for 30 mins at RT. They were incubated in permeabilization solution (0.1% Triton X-100 (BioBasic) in PBS) for 5 mins and then in blocking solution (3% FBS in PBS) for 10 mins. Washes were performed between all treatments, and the study was carried out at RT. PE mouse anti-rat CD31 (BD Pharmingen) was diluted 1:25 with antibody solution (1.5% FBS in PBS). The diluted antibodies were added to the cells, and after treatment at RT for 1 h, unbound conjugates were washed away. Secondary goat anti-mouse IgG (Invitrogen) was diluted 1:1000 in antibody solution. This antibody was also added to the cells and kept at RT for 1 h. After washing, DAPI (Sigma) diluted at 1:1,000 was added to the wells and incubated for 15 mins. Prolong Diamond Antifade Mountant (Invitrogen) was dropped on the samples, and images were taken under a fluorescent microscope.

3.4.2.2. Dil acetylated low-density lipoprotein (Dil-Ac-LDL)

rPBECs cells were seeded at a density of 2×10^4 in 24-well plates. After 2 days, staining was performed to determine the Dil-Ac-LDL uptake capacity of the cells. Cells were

washed twice with Ca^{+2} and Mg^{+2} containing PBS with 1% BSA. To starve the cells, they were kept overnight in an incubator in 0.05% FBS medium. The medium was removed, and the cells were kept in complete medium containing 10 μg/mL Dil-Ac-LDL (Invitrogen) in an incubator at 37 °C for 3 h. Washing was performed several times. Cells were fixed in a 3.7% formaldehyde solution for 30 mins at RT. Following washing, DAPI diluted 1:1000 was added and allowed to sit for 15 mins. Prolong Diamond Antifade Mountant was dropped on the samples, and images were taken under a fluorescent microscope.

3.4.3. Cell Labeling

3.4.3.1. Labeling of rBMSCs

Red Fluorescent Cell Linker Kit (Sigma-Aldrich) was used to label rBMSCs. For this, cells were suspended in serum-free medium at a concentration of 1 x 10^6 cells/mL. Cells were centrifuged for 5 mins at 400 x g. All of the supernatant was removed carefully after centrifugation. Diluent C (100 μL) was added and pipetted slowly until cells were homogeneously dispersed. In another eppendorf, 0.4 μL of dye solution was dissolved in 100 μL of Diluent C. The cell suspension was mixed with the dye solution and pipetted. It was mixed periodically for 5 mins. The same amount of FBS was added to the medium to stop staining. Cells were centrifuged for 10 mins at 400 x g. After removing the supernatant, it was resuspended in GM and centrifuged again. The washing steps were repeated two more times. Cells were seeded in a well plate. Images were taken the next day with a fluorescent microscope.

3.4.3.2. Labeling of rPBECs

Vybrant™ DiO cell-labeling solution (Invitrogen) was used to label rPBECs. For this, cells were suspended in serum-free medium at a concentration of 1 x 10^6 cells/mL. Cell labeling solution (5 μL) was added and incubated in the incubator for 20 mins. Labeled cells were centrifuged for 5 mins at 1,500 rpm, the supernatant was removed, and the cells were resuspended in completed EBM medium. The washing steps were repeated two more times. Cells were seeded in a well plate. Images were taken the next day with a fluorescent microscope.

3.5. *IN VITRO* MATERIAL-CELL INTERACTIONS

Scaffolds sterilized in 70% ethanol for 1 h at +4 °C. After sterilization, scaffolds were washed with Dulbecco's phosphate-buffered saline (DPBS) several times, transferred into well plates, and maintained in 0.5 mL of growth media per well for overnight prior to cell seeding.

After determination of the optimal cell seeding density, the cells were trypsinized and centrifuged at 1,800 rpm for 5 mins. The cells were counted with the Countess II FL Automated Cell Counter (Thermo Fisher Scientific, USA). rBMSCs were seeded from the top surface and incubated at 37 °C for 3 h to allow for cell attachment. The cell-seeded scaffolds were incubated at 37 °C in a CO_2 incubator for further experiments.

For cell attachment and proliferation studies, the cells were cultured in GM for 21 days. For differentiation studies, the cells were cultured in GM for three days before being switched to OM for another 21 days. The media is refreshed every three days.

3.5.1. Cell Viability by MTS Assay

CellTiter 96® Aqueous One Solution Assay (Promega) was performed on days 1, 7, 14, and 21 to determine cell viability on scaffolds. Briefly, cell-seeded scaffolds were incubated in a mixture of medium/MTS assay reagent (5:1 v/v) for 2 h at 37 °C in a CO_2 incubator. Afterwards, 200 μL of the mixture was transferred into a 96-well plate and the absorbance was measured at 490 nm using the Elisa Plate Reader (VarioSkan Lux, Thermo Scientific). Corresponding cell numbers to absorbance values in each scaffold were determined after calibration curve construction.

3.5.2. Live-Dead Assay

Live-Dead Viability-Cytotoxicity Kit for mammalian cells (ThermoFisher Scientific) was used to determine the viability of cells in a population based on plasma membrane integrity. Briefly, scaffolds were washed with PBS, Calcein-AM, and Ethidium Bromide,

diluted in PBS, added to scaffolds, and incubated in 5% CO_2 at 37 °C for 45 min. Images were taken with a fluorescence microscope (VertA1, Zeiss, Germany).

3.5.3. Cell Proliferation by PicoGreen Assay

To determine the cell proliferation in scaffolds, the PicoGreen assay kit (Quant-iT™ PicoGreen® dsDNA Assay Kit, Thermo Fisher Scientific, Waltham, MA, USA) was used. In the first step, 500 µL of cell lysis buffer was added to each well-containing scaffold. Afterward, the samples were deep-frozen at 60 °C and then thawed at 37 °C for three cycles. The amount of DNA was determined according to the manufacturer's instructions. The fluorescence intensity was measured on a plate reader (VarioSkan Lux, Thermo Scientific) at λ_{ex}=480 nm, λ_{em}=520 nm. To determine the amount of DNA, a DNA standard curve was constructed using the given lambda DNA.

3.5.4. Alkaline Phosphatase Activity

Cell seeded scaffolds were incubated with OM for 3, 7, 14, and 21 days. The activity of ALP was measured spectroscopically using SIGMA*FAST*™ p-nitrophenyl phosphate tablets (Sigma–Aldrich). One tablet from each pNPP and Tris buffer was dissolved in deionized water and then added to the wells. The plate was incubated in 5% CO_2 at 37 °C for 1 h. Absorbances were measured at 405 nm using the Elisa Plate Reader (Varioskan Lux, Thermo Scientific). To calculate the ALP activity of samples, the necessary calculations were performed, and a graph of normalized values vs. time was plotted.

3.5.5. Calcium Assay

The cells were seeded at a concentration of 50,000 cell/scaffold and incubated in OM for 7, 14, and 21 days. The QuantiChrom™ Calcium assay kit (BioAssay Systems) was used for the quantitative determination of the calcium ion Ca^{+2}. For this, equal amounts of reagents A and B were mixed. It was added to the scaffolds and left in the incubator for 30 mins. Absorbances were measured at 612 nm using the Elisa Plate Reader. The Ca^{+2} concentration in the medium was determined by the calibration curve.

3.5.6. Osteocalcin Analysis

Cell culture supernatants were used for OCN detection. For this purpose, the media of the scaffolds seeded with rBMSCs (50,000 cells/scaffold) were taken from the wells at the end of days 7, 14, and 21 and immediately stored at -20 °C. Rat Gla-Osteocalcin High Sensitive EIA Kit (Takara) and Rat Glu-Osteocalcin High Sensitive EIA Kit (Takara) were used for the study. All reagents and samples were brought to RT. Samples (100 µl) were added to the antibody-coated plate through a 12-channel pipette, and the reaction was carried out for 1 h at RT. After washing with the washing solution (0.1% Tween 20 in PBS), 100 µl of labeled antibody solution was added, and the reaction was allowed to run for 1 h at RT. Following the washing steps, 100 µl of substrate solution was added to the wells and allowed to react for 15 mins at RT. Finally, stop solution was added to the wells, and they were mixed carefully. Absorbances were measured at 450 nm using the Elisa Plate Reader. The standard solution for the standard curve was prepared with serial dilutions. The same protocol was applied for both EIA kits.

3.5.7. Realtime-PCR

For this analysis, rBMSCs (100,000 cells/scaffold) were seeded into scaffolds in a 24-well cell culture plate. OM was used during the 21-day incubation period and freshly added to the medium on each medium change day. After 7, 14, and 21 days of incubation, the expression levels of bone-specific genes (ONC, Runx2, and Collagen Type I) were determined by real-time PCR analysis.

For this purpose, firstly, total RNA was isolated from the cells on the scaffolds using the easy-spin™ Total RNA Extraction Kit (Intron). Then, RNAs were converted to cDNA with the iScript cDNA synthesis kit (BioRad). Primers designed for bone-specific genes (Table 3.3) and real-time PCR using the Maxima SYBR Green qPCR Master Mix (ThermoScientific) kit were performed using the CFX96 Touch™ Detection System. Real-time PCR results were normalized using GAPDH, a housekeeping gene. For calculations, at the end of this study, fold-change graphs were drawn by subtracting the value of the expression results of all experimental groups from the value of the expression results of only the scaffold group.

Table 3.3 Sequences of the primers used for the Real Time PCR.

Primers		Sequence (5'→3')
GAPDH	F	TGGTGAAGGTCGGAGTGAAC
	R	CACCCCATTTGATGTTGGCG
ALP	F	GGGTACACCATGATCTTGCCA
	R	CGTCTTGGAGAGAGCCACAAA
Osteocalcin	F	AAGTCCCACACAGCAACTCG
	R	GTCCTGGAAGCCAATGTGGT
Osteonectin	F	CACTGGCTGTGTTGGAAACG
	R	GTGGAGGAGACAGCAAGGTC
Runx2	F	TCACTACCAGCCACCGAGAC
	R	ACGCCATAGTCCCTCCTTTT
Collagen Type I	F	GCCTGCACATGTGTGGCCG
	R	CTGCCCCTCGCAGGGGTTT

3.5.8. von Kossa Staining

Prior to staining, cells or scaffolds were washed several times with PBS, and cells or cells on scaffolds were fixed with 2% (w/v) paraformaldehyde for 1 h. Then, fixed cells were washed with distilled water (dH_2O). Diagnostic Biosystems kit was used for staining according to the manufacturer's instructions (3.4.1.1). Images of the mineralized scaffolds were taken with a digital camera or inverted microscope.

3.5.9. Alizarin Red Staining

Prior to staining, cells or scaffolds were washed several times with PBS, and cells or cells on scaffolds were fixed with 2% (w/v) paraformaldehyde for 1 h. Then, fixed cells were washed with distilled water (dH_2O). The alizarin red staining kit was used as directed by the manufacturer (3.4.1.1). Images of the mineralized scaffolds were taken with a digital camera or inverted microscope.

3.5.10. *In Vitro* Angiogenesis

The fibrin *in vitro* angiogenesis assay kit (Merck) was used to prove the effect of the small molecules and NPs used on vascularization. The role of rPBECs in tube formation was observed with this method. The fibrinogen solution was thawed in a 37°C shaking water bath, while the thrombin solution was at RT. The fibrinogen solution (30 µl) was added to the 96-well plate. Thrombin (20 µl) was added to it, and it was polymerized for 60 mins at 37 °C. Only EBM medium, 30 ng/mL VEGF in EBM, 10 µg/mL GS4012 in EBM, 10 µg/mL GS4012-loaded NP in EBM, and a 1:100 diluted positive control in EBM were determined as sample groups.

rPBECs were prepared at 5 x 10^4 cells/mL. Cells of 100 µl were added to each well of the 96-well plate on top of the polymerized fibrinogen-thrombin solution. They were kept in the incubator overnight. The next day, the well plate was inverted onto sterile gauze, and the medium was completely removed from the environment. Another 30 µL of fibrinogen was added to each well, followed by addition of 20 µL of thrombin, and it was kept at 37°C for 5 mins to polymerize. Each well received 100 µL of each of the determined sample groups. The samples were then transferred to a 37 °C, 5% CO_2 incubator. At the end of 48 and 120 h, images were taken with an inverted microscope.

3.5.11. Migration Assay

Insert-wells were used for this assay. rPBECs (50,000 per insert) were seeded in each insert. Only EBM medium, VEGF (30 ng/mL) in EBM, GS4012 (10 µg/mL) in EBM, and GS4012-loaded (10 µg/mL) NP in EBM were determined as sample groups. It took 72 h for the cells to migrate to the well's surface. At the end of the period, the cells in the inserts were washed with PBS and fixed with 3.7% formaldehyde. Crystal violet dye was added to the fixed cells, and incubated for 10 mins. Following the washing, images of the cells in the inserts and well plate surfaces were captured using an inverted microscope.

3.5.12. Immunofluorescence Staining of Coated Scaffolds

With this analysis, the migration of rPBECs onto the scaffold was characterized by IF staining. For this purpose, red fluorescent-stained (3.4.3.1) rBMSCs were seeded at a concentration of 50,000 cells per scaffold. Green fluorescent-stained (3.4.3.2) rPBECs were seeded into inserts with a 0.8 μm pore at a density of 50,000 cells per insert. One day later, the experiment was started by placing the inserts on the scaffolds. At the end of days 3, 7, and 14, images of the scaffold surfaces were taken with a fluorescent microscope.

4. RESULTS

4.1. PLA SCAFFOLD CHARACTERIZATION

PLA filaments of two different brands (BASF and Corbion) were used in the studies carried out in this section. Characterizations were carried out for PLA polymers belonging to these two brands.

4.1.1. Bright Field and Scanning Electron Microscope Analysis

Digital, optical microscope, and SEM images of the PLA (BASF) scaffolds with different filling rate structures are presented in Figure 4.1 B-D. Pore diameters calculated using the ImageJ program are shown in Table 4.1. When the digital images in Figure 4.1A were investigated, it was seen that high resolution, smooth surfaces, and desired sizes of scaffolds can be produced by means of a 3D printer. It correlates with the digital images taken with the BF microscope, as seen in Figure 4.1B. It can be distinguished that the sizes of all pores were equal, the pores were homogeneously distributed, and the fiber thicknesses were equal and smooth. SEM images of the scaffolds were recorded to analyze the structure in 3D (Figure 4.1D). PLA scaffolds had well-defined structures with a pore size range of 103.8 ± 22.45 and 556.9 ± 17.79 μm. Fiber thickness was calculated from the SEM images, and actual fiber thickness was obtained as 249.6 ± 9.57 μm.

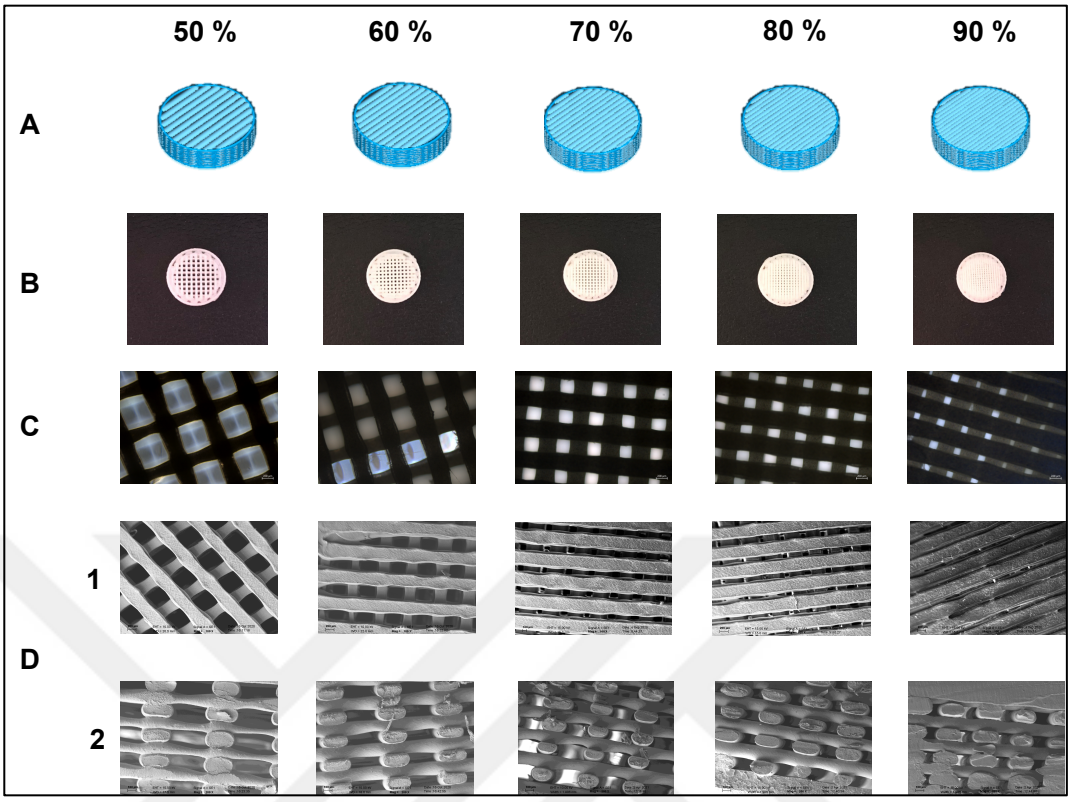


Figure 4.1 Structural and morphological characterization of a 3D-printed PLA (BASF) scaffold with different pore sizes (50, 60, 70, 80, and 90%). (A) CAD design of the 3D-printed scaffolds, (B) Digital images of 3D-printed scaffolds, (C) BF images of 3D-printed scaffolds, scale: 200 µm, (D) SEM analysis of 3D-printed scaffolds : (1) Top view images of the 3D-printed scaffolds, scale: 200 µm, (2) Cross-section images of the 3D-printed scaffolds, scale: 100 µm.

Table 4.1 Porosity, fill rates, and pore sizes (top view and cross-section) of the 3D-printed scaffold.

	SEM				**BF**		
Filling rates of scaffolds %	**Pore sizes (µm)**	**Pore sizes (cross-sections µm)**	**Porosity %**	**Fill rate %**	**Pore sizes (µm)**	**Porosity %**	**Fill rate %**
50	556.90 ± 17.79	477.40 ± 37.12	35.11	64.08	690.68 ± 8.65	42.47	56.97
60	467.10 ± 35.73	371.50 ± 37.68	24.60	75.11	444.99 ± 17.97	26.32	71.01
70	226.22 ± 10.19	279.93 ± 21.02	5.75	N/A	310.90 ± 13.00	19.82	80.80

80	165.60 ± 28.78	195.22 ± 18.14	3.11	N/A	236.00 ± 17.59	14.33	87.50
90	103.80 ± 22.45	197.18 ± 5.48	N/A	N/A	155.30 ± 8.88	5.62	94

The study was continued with Corbion PLA after the optimum pore size was determined. Digital, BF, and SEM images of the scaffold of Corbion PLA with a 60% fillling rate are shown in Figure 4.2 A-D. With the ImageJ analysis of the images taken from the top, it was seen that the pore diameter was 464.30 ± 10.60, and the size of the pores in the cross-section was 346.46 ± 26.46. Porosity was calculated as 43.8%.

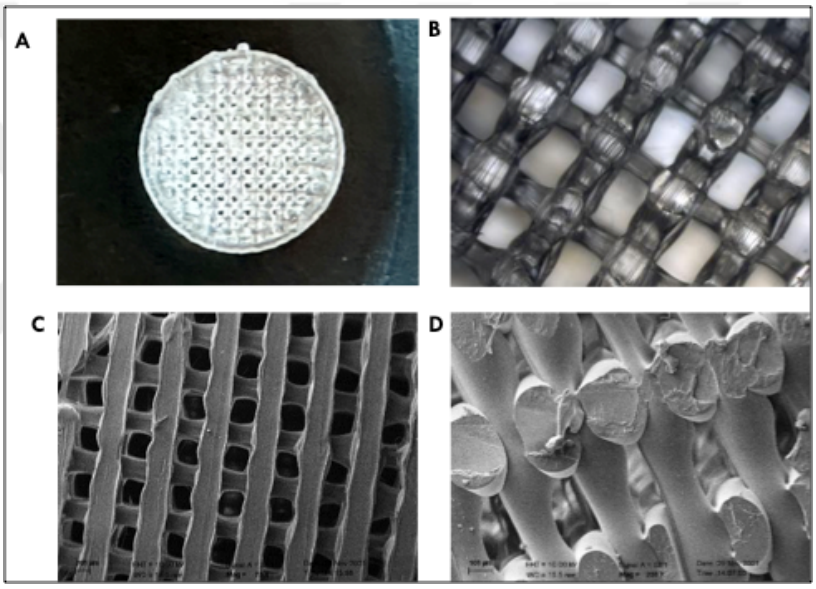


Figure 4.2 Structural and morphological characterization of 3D-printed PLA (Corbion) scaffold with 60% filling rate. (A) Digital image, (B) BF image, scale:200 μm, (C) SEM analysis, top view image, scale: 200 μm, (D) SEM analysis, cross-section image, scale: 100 μm.

4.1.2. Fourier Transform Infrared Spectrophotometer (FT-IR)

Chemical characterization of the PLA scaffold was carried out with FT-IR analysis. The specific groups for the PLA structure are indicated in Figure 4.3. The peaks at 2,953 and 2,916 cm^{-1} belong to the C–H stretching of PLA. The specific resonance of the carbonyl (C=O) was detected at 1,741 cm^{-1}. Also, the carboxyl group of the PLA was observed at 1,176 cm^{-1}. The peak at 1,073 cm^{-1} represented the –OH group of the PLA.

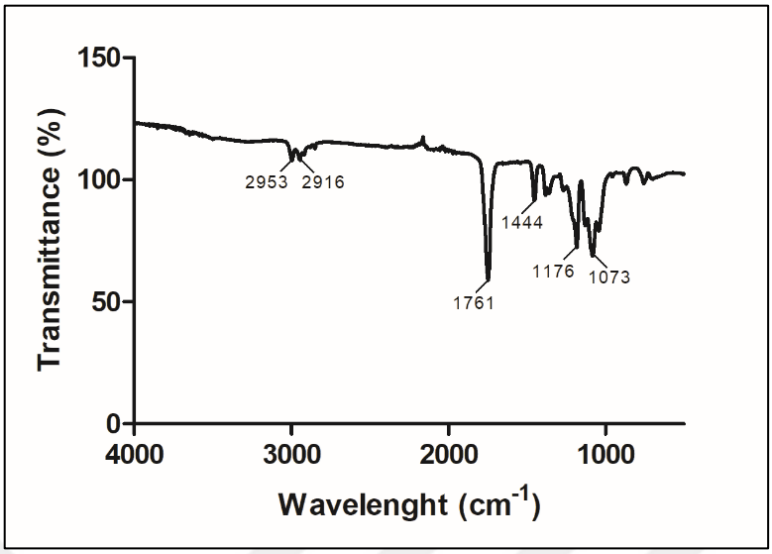


Figure 4.3 FT-IR spectrum of PLA.

4.1.3. Differential Scanning Calorimetry (DSC)

Thermal characteristics of PLA samples both pre and post-processing were determined with the DSC analysis (Figure 4.4). DSC analysis showed that the printing process decreased T_g ~ 15 °C (Table 4.2). It also confirmed that the crystalline fraction of PLA did not change significantly when the polymer was processed. Moreover, there was no significant difference between the melting temperature values before and after the process.

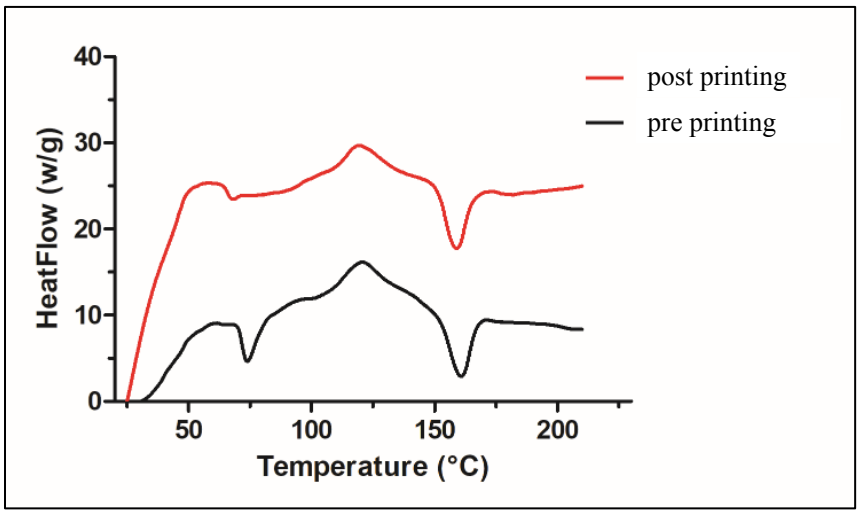


Figure 4.4 DSC thermograms of pre and post printing of PLA, respectively.

Table 4.2 DSC measurements of pre and post printing of PLA.

	Tg (°C)	Crystallinity (°C)	Tm (°C)
Pre printing	73.01	116.38	159.22
Post printing	60.62	111.68	155.40

4.1.4. Contact Angle Measurement

Hydrophilic properties of five different scaffold types were investigated by a contact angle study (Figure 4.5 A,B). The contact angle degrees of the scaffolds were found to be 87.90 ± 4.32, 86.96 ± 8.01, 96.33 ± 0.70, 83.93 ± 5.06, and 85.46 ± 3.79, respectively. There was no significant difference between groups.

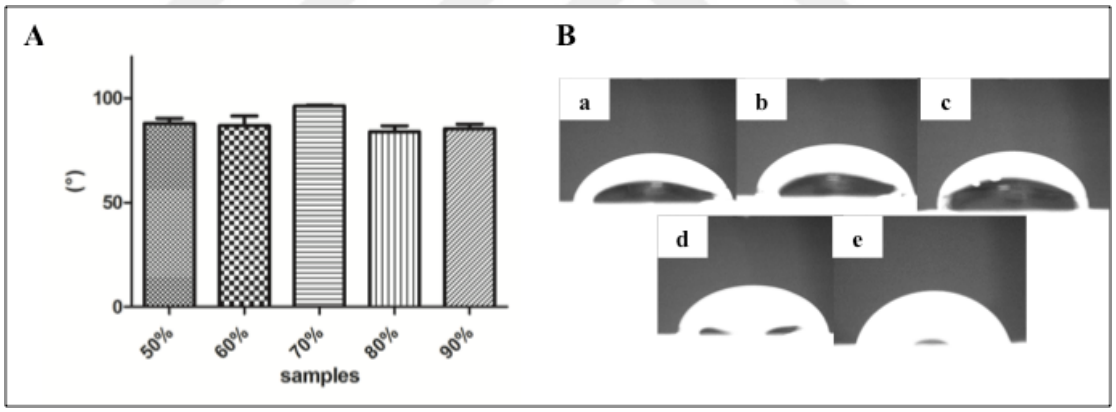


Figure 4.5 Contact angle measurement analysis of 3D-printed scaffolds. (A) Values of the contact angle of the 3D-printed scaffolds with different filling rates, (B) Images of the droplet of the 3D-printed scaffolds with a filling rates of (a) 50%, (b) 60%, (c) 70%, (d) 80%, and (e) 90%.

4.1.5. Mechanical Analysis

Compression and tensile tests were performed on scaffolds with different filling rates (Figure 4.6 A,B). The analysis was continued until the scaffold broke in the compression test and in the tensile test.

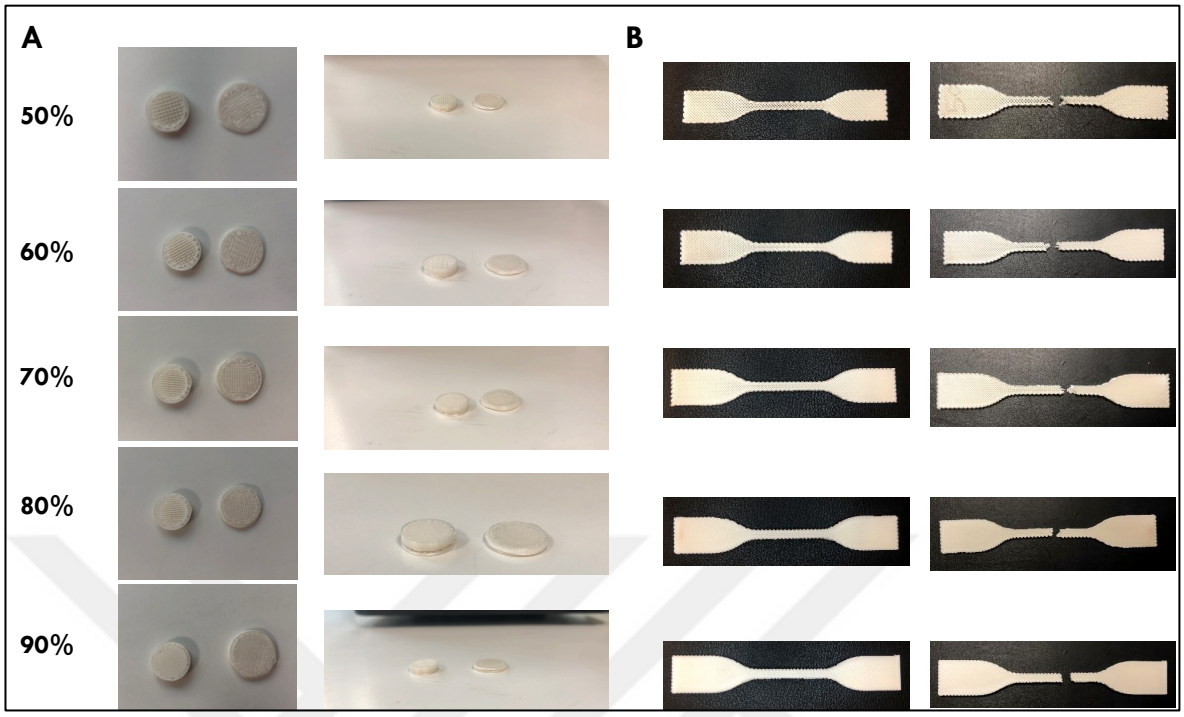


Figure 4.6 Digital images of scaffolds before and after mechanical analysis: (A) compression and (B) tensile analyses.

Data on compression modulus, yield strength, and compressive strength for scaffolds are shown in Figure 4.7 A–C. The compression modulus of PLA scaffolds increased as the fill rate increased. The compression modulus varied between 3,032.96 ± 541.39 and 10,688.23 ± 1,194.38 MPa. The compressive Young's modulus of the scaffold with a 90% filling rate was significantly different from the others. While yield power increased with the filling rate, it was seen that the compressive strength at yield and load values at the breaking point were not significantly affected by the filling rates. In Figure 4.7D–F, tensile modulus, ultimate tensile strength, and fracture strength data for the scaffolds are also shown. It can be seen that the tensile modulus of PLA scaffolds also increased significantly with the filling rate. The tensile modulus varied between 323.11 ± 22.78 and 924.24 ± 29.56 MPa. Likewise, ultimate tensile and fracture strengths increased with the filling rate. Unlikely, ultimate tensile strength showed significant differences between the groups, and with respect to fracture strength, only the scaffold with a 90% filling rate showed a significant difference.

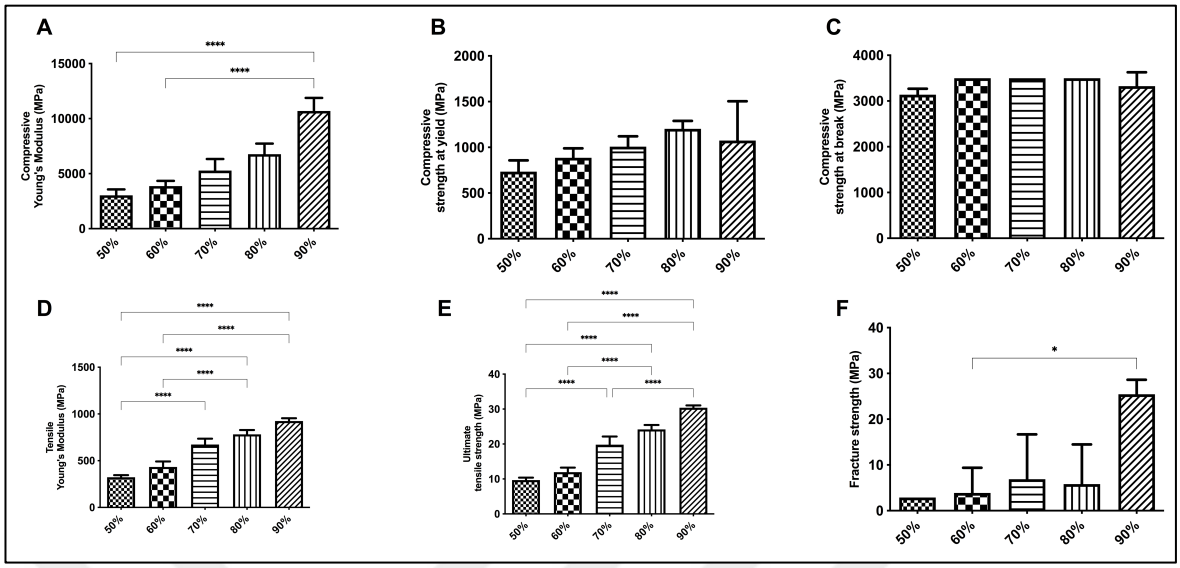


Figure 4.7 Mechanical analysis of 3D-printed PLA scaffolds with different filling rates. (A) Compressive Young's modulus, (B) Compressive strength at yield, (C) Compressive strength at break, (D) Tensile Young's modulus, (E) Ultimate tensile strength, (F) Fracture strength of the 3D-printed PLA scaffold with different filling rates; n=3, $p < 0.0001$. *$p < 0.05$; ****$p < 0.0001$.

4.1.6. *In vitro* Degradation Analysis

After *in vitro* degradation analysis, it was seen that the weight loss of the scaffolds was not even 1% throughout the 120 days of incubation. Especially on scaffolds with the higher filling rates (70, 80, and 90%), weight loss was found to be zero. It was seen that PLA scaffolds could swell up to 0.3 times their own weight over time. When the swelling ratios were compared with each other, it was seen that the swelling amount decreased up to 10% as the fill rates of the scaffold increased. When the pH changes of scaffolds were examined, it was seen that by day 120, the lactic acid release as a result of degradation did not change the pH of the environment significantly and that the pH of the environment was preserved (Figure 4.8 A-C).

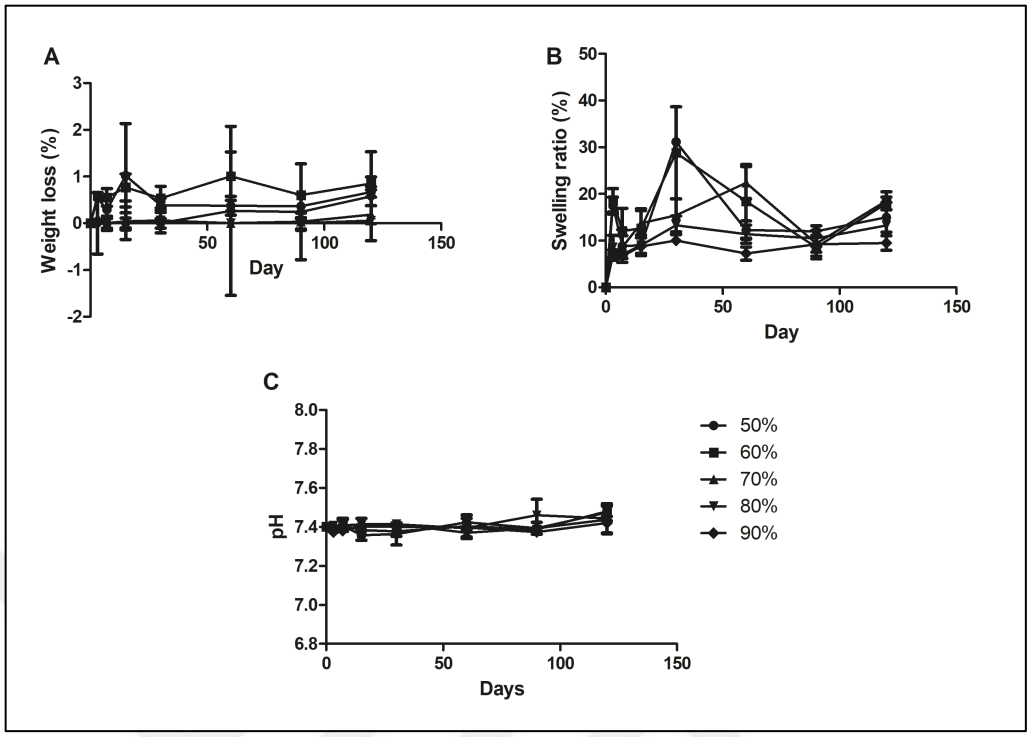


Figure 4.8 *In vitro* degradation behavior of 3D-printed PLA (BASF) scaffolds with different filling rates in PBS solution at 37 °C with respect to (A) weight loss (%), (B) swelling ratio (%), and (C) pH changes throughout 120 days of incubation.

After enzymatic degradation, 10–16% weight loss was observed in the scaffolds at the end of day 5. It was observed that this loss increased between 19 and 30% after day 10 (Figure 4.9). After 5 days of enzymatic degradation, the mean weight loss of the PLA scaffold groups was recorded as 16.76 ± 1.32, 15.80 ± 1.78, 13.11 ± 0.57, 11.74 ± 0.23, and 10.02 ± 0.68%, respectively. After 10 days, the weight losses of the scaffolds were 30.87 ± 5.69, 29.05 ± 1.99, 24.68 ± 1.25, 21.22 ± 0.68, and 18.61 ± 1.47%, respectively. It was observed that the weight loss accelerated 1.5 times, especially in the samples with a lower filling rate (Figure 4.9A). While the initial pH value of the enzymatic degradation solution was 8.4, it was observed that this value dropped dramatically to 5 due to the lactic acid release (Figure 4.9B). At the end of day 5, the pH value changes of the samples with increasing pore size were 4.92 ± 0.13, 5.19 ± 0.15, 4.76 ± 0.33, 5.26 ± 0.34, and 5.1 ± 0.06, respectively. After day 10, the pH changes of the samples with increasing pore sizes were found to be 5.44 ± 0.33, 5.12 ± 0.07, 6.23 ± 0.10, 5.28 ± 0.04, and 6.26 ± 0.34, respectively.

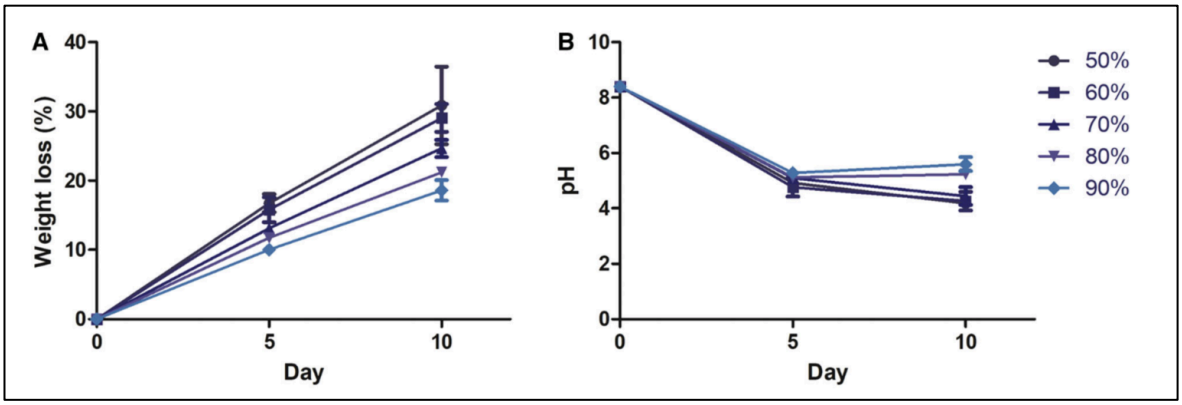


Figure 4.9 Enzymatic degradation behavior of 3D-printed PLA scaffolds with different filling rates in enzyme solution at 37 °C with respect to (A) weight loss (%), and (B) pH changes throughout 10 days of incubation.

The *in vitro* degradation study of the scaffold produced with Corbion PLA with a 60% filling rate was used in the continuation of the study. At the end of day 120, it was observed that the original weight of the scaffold decreased by only 1% and swelled by 6-8%. The pH value of the medium decreased from 7.4 to 7.2 (Figure 4.10).

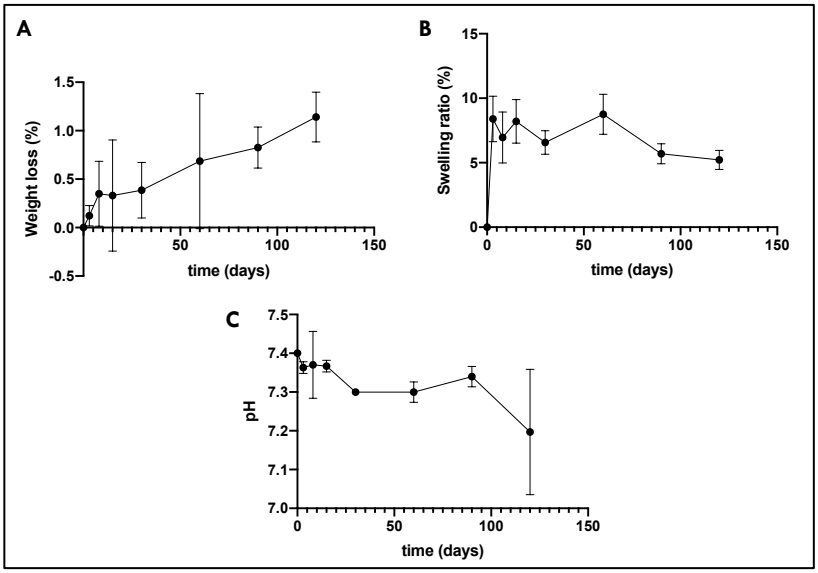


Figure 4.10 *In vitro* degradation behavior of a 3D-printed PLA (Corbion) scaffold in PBS solution at 37 °C with respect to (A) weight loss (%), (B) swelling ratio (%), and (C) pH changes throughout 120 days of incubation.

An enzymatic degradation study was performed for untreated Corbion PLA, uncoated PLA, and NP coated PLA scaffold (Figure 4.11). Samples were analyzed at the end of days 5, 10, and 15. The scaffold, which had a 60% filling rate, was degraded, losing 14% of its weight. While the uncoated scaffold lost 7% at the end of the day 5, this loss reached 16% at the end of the day 15. At the end of the study, there was a 12% degradation in the NP coated scaffold.

While the swelling rate increased to 5% on day 5, especially in the NP coated scaffold, the swelling rates on the last day of the study could not be calculated due to weight losses. It was observed that the pH value, which was 8.4 in all sample groups, decreased to 4, with a sharp decrease from the first days.

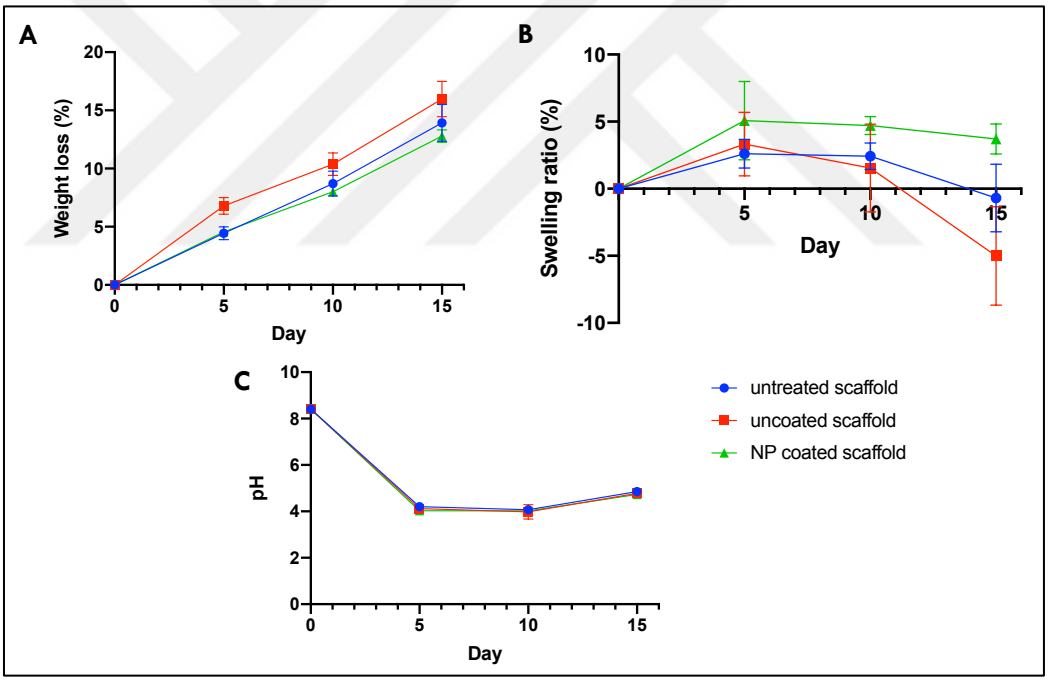


Figure 4.11 Enzymatic degradation behavior of 3D-printed PLA scaffolds in enzyme solution at 37 °C with respect to (A) weight loss (%), (B) swelling ratio (%), and (C) pH changes throughout 15 days of incubation.

4.2. NANOPARTICLE CHARACTERIZATION

4.2.1. Zeta-sizer

After synthesizing of CS NPs, the first step was to determine their size. Size charts of NPs taken directly from the post-synthesis medium were shown in Figure 4.12 and Figure 4.13. The size, PDI, and zeta potential results obtained from the Zeta device were shown in Table 4.3. Although the initial result for blank Np (NP1–8) was insignificant, synthesis was performed on average at around 100–150 nm when the conditions were changed. In the synthesis studies performed with BSA before small molecule loading with the optimum conditions of blank NP (BNP1–4), synthesis was realized on a large scale with the amount of material placed in the 150–350 nm range. In the synthesis of DIPQUO loaded NP (D-NP1–16), GS4012 loaded NP (G-NP1–6), and dually loaded NP (DG-NP1–12), particle syntheses starting from 100 nm to micron sizes were performed. As a result of these, optimum conditions were determined. In optimized conditions, NPs with an average size of 100–150 nm and a PDI value of 0.2–0.3 were synthesized from blank and loaded NPs. While blank NPs were around 100 nm, it was observed that their size increased up to 150 nm with the encapsulation of molecules. At the same time, the PDI values did not change much.

Table 4.3 Physicochemical properties of CS NPs.

Sample	Zavg (nm)	PDI	Intensity (nm)	RY (%)
NP1	2182 ± 84.15	0.978 ± 0.03	369.3	72.50
NP2	106.40 ± 0.39	0.248 ± 0.01	131.1	52.14
NP3	110.90 ± 2.50	0.306 ± 0.03	134.9	56.92
NP4	142.10 ± 11.72	0.361 ± 0.05	174.2	50.00
NP5	158.30 ± 0.07	0.485 ± 0	226.9	33.64
NP6	113 ± 1.57	0.256 ± 0.01	152	40.00
NP7	139.60 ± 2.22	0.231 ± 0.01	179.5	50.77
NP8	182.90 ± 3.28	0.484 ± 0.01	297.6	30.00
B-NP1	98.19 ± 0.58	0.324 ± 0.04	134.5	30.00
B-NP2	155.10 ± 4.83	0.194 ± 0.01	178.9	21.88
B-NP3	282.10 ± 14.55	0.288 ± 0.01	382.9	26.67
B-NP4	343.90 ± 18.27	0.399 ± 0.01	493.4	34.78

D-NP1	172.70 ± 1.80	0.397 ± 0.02	280.3	36.15
D-NP2	124.10 ± 8.29	0.409 ± 0.05	162.6	12.31
D-NP3	134.40 ± 10.91	0.350 ± 0.03	157.8	26.15
D-NP4	126.50 ± 10.54	0.366 ± 0.02	136.1	26.92
D-NP5	124.90 ± 3.49	0.471 ± 0.04	184.4	13.08
D-NP6	211.20 ± 37.51	0.459 ± 0.16	310.4	23.08
D-NP7	161.10 ± 8.99	0.369 ± 0.02	197.9	40.77
D-NP8	136.80 ± 0.87	0.272 ± 0.01	180.6	72.31
D-NP9	151.20 ± 2.30	0.328 ± 0.05	210.2	46.92
D-NP10	249.80 ± 9.41	0.437 ± 0.02	379.9	73.85
D-NP11	270.50 ± 8.13	0.442 ± 0.01	476.2	70.77
D-NP12	131.50 ± 0.21	0.312 ± 0.03	178.3	55.38
D-NP13	126.60 ± 4.03	0.260 ± 0.01	163.5	53.85
D-NP14	146.50 ± 3.25	0.303 ± 0.05	189	49.23
D-NP16	139.90 ± 2.70	0.300 ± 0.05	156.6	60.77
G-NP1	151.10 ± 3.56	0.270 ± 0.02	203.4	45.38
G-NP2	102.90 ± 2.35	0.272 ± 0.02	136.3	61.54
G-NP3	105.70 ± 1.61	0.286 ± 0.01	149.1	72.31
G-NP4	157.30 ± 3.32	0.305 ± 0.03	215.2	41.54
G-NP5	759.8	0.639	307.3	71.54
G-NP6	3944	1	106.3	70.77
DG-NP1	128 ± 1.08	0.265 ± 0.01	170.3	32.31
DG-NP2	121.50 ± 0.88	0.286 ± 0.01	169.8	47.69
DG-NP3	130.30 ± 3.42	0.306 ± 0.03	150.9	26.15
DG-NP4	118.50 ± 3.26	0.287 ± 0.03	145.2	24.62
DG-NP5	124.40 ± 0.78	0.288 ± 0.01	172.1	58.46
DG-NP6	120.60 ± 2.10	0.279 ± 0.00	167.1	59.23
DG-NP7	106.20 ± 1.56	0.205 ± 0.01	131.1	34.62
DG-NP8	127 ± 3.32	0.264 ± 0.03	165.5	33.85
DG-NP9	125.40 ± 1.50	0.204 ± 0.01	154.2	46.92
DG-NP10	111.30 ± 2.29	0.249 ± 0.04	141.9	60.00
DG-NP11	138.30 ± 3.067	0.351 ± 0.04	197.8	56.15
DG-NP12	121.70 ± 1.74	0.331 ± 0.03	177.6	38.46

Size distribution results of blank NPs synthesized at the end of different methods are given in Figure 4.12. In the results obtained with Zetasizer, a single peak was seen for all NPs. This peak indicated that the NPs in the suspension were uniformly distributed.

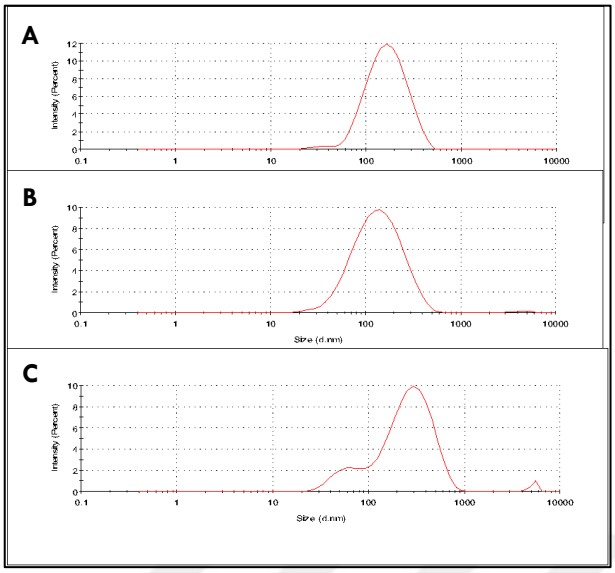


Figure 4.12 Size distribution graphs of blank NPs with ionic gelation method using (A) magnetic stirrer, (B) burette, and (C) sonicator.

The size distribution results of blank, BSA, DIPQUO, GS4012, and dual small molecule loaded NPs are given in Figure 4.13.

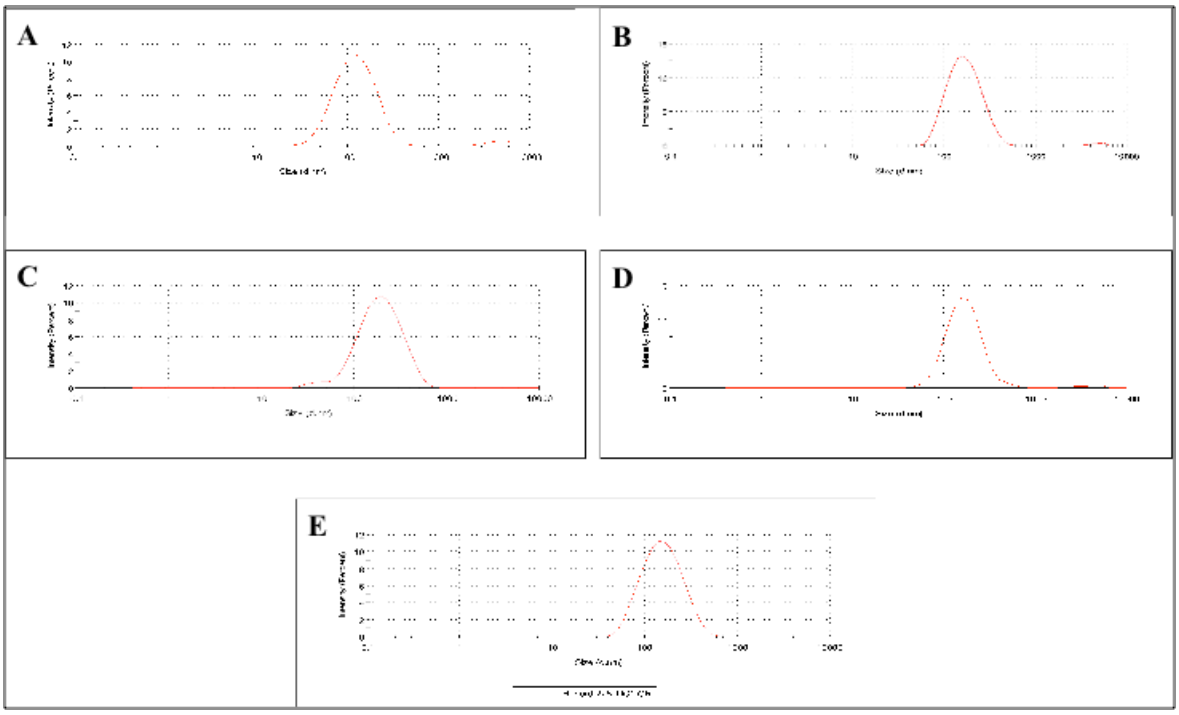


Figure 4.13 Size distribution graphs of NPs synthesized with magnetic stirrer (A) blank NP, (B) BSA-NP, (C) D-NP, (D) G-NP, and (E) DG-NP.

The zeta potential distribution results of blank, BSA, DIPQUO, GS4012, and dual small molecule loaded NPs are given in Figure 4.14. The zeta potential results obtained from optimized conditions were shown in Table 4.4. While the zeta potential value was 14 mV in the blank NPs, this value increased slightly in the NPs after the molecule was loaded, but this increase was not significant.

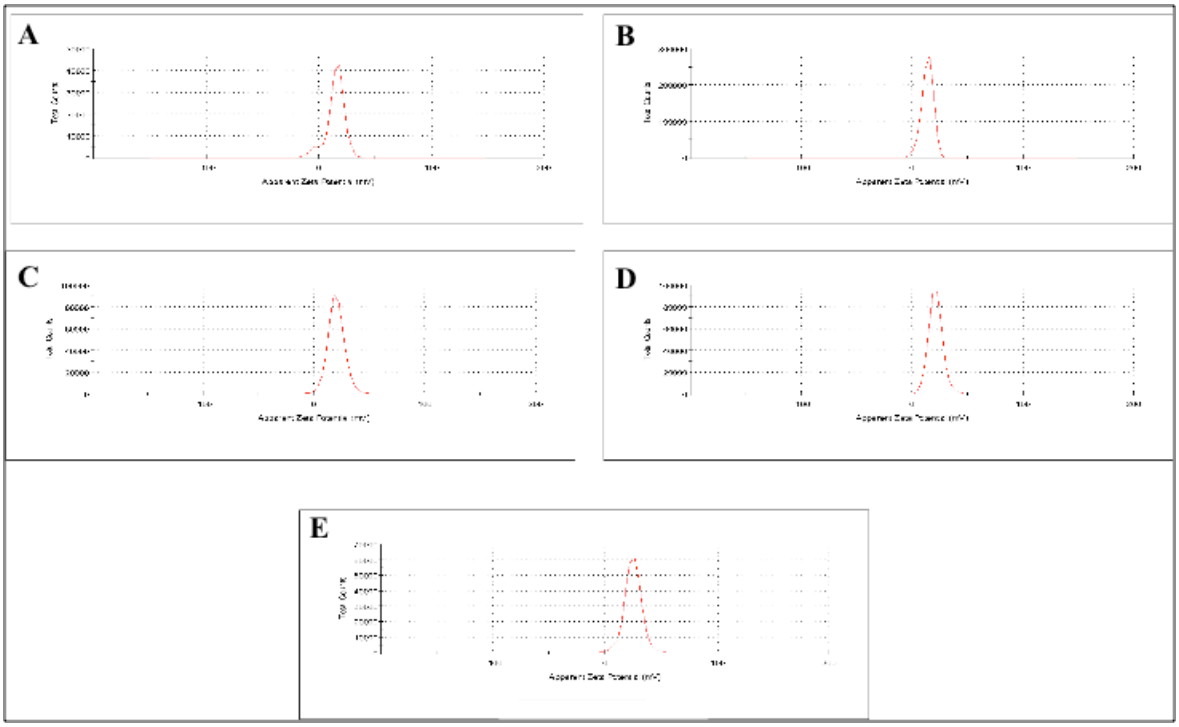


Figure 4.14 Zeta potential distribution graphs of (A) blank NP, (B) BSA-NP, (C) D-NP, (D) G-NP, and (E) DG-NP.

Table 4.4 Zeta potential results of NPs.

Sample	**Zeta Potential (+, mV)**
Blank-NP	14.8±2.18
D-NP	17.8±0.361
G-NP	21.1±0.361
DG-NP	18±0.737
B-NP	13.90 ± 0.25

4.2.2. TEM

The TEM micrographs for blank CS NPs are shown in Figure 4.15. The results showed that blank CS NPs had an average size distribution of 150 nm.

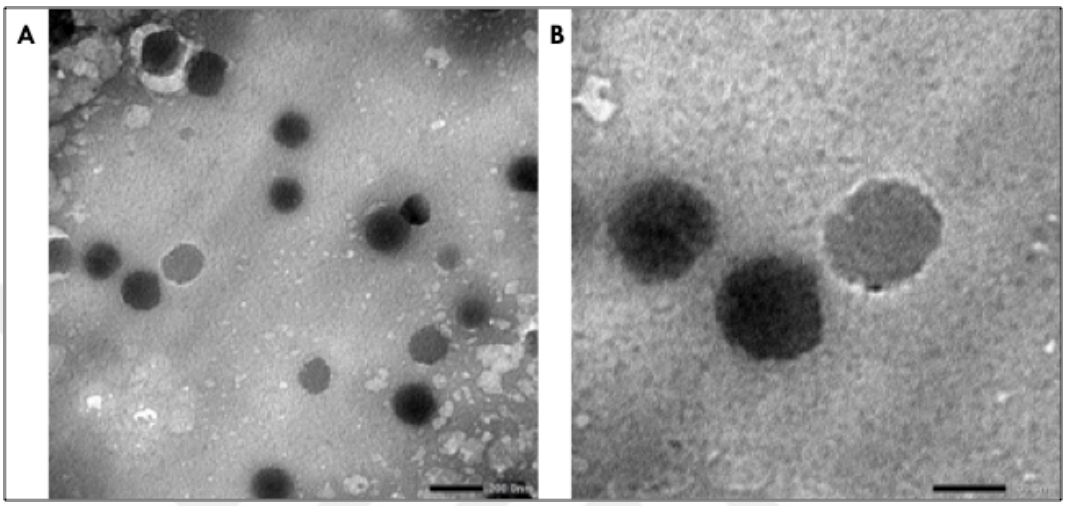


Figure 4.15 TEM micrographs of blank chitosan nanoparticles with a scale of (A) 200 nm, and (B) 100 nm.

4.2.3. FT-IR

The FT-IR spectra of CS, TPP, Tween 20, DIPQUO, GS4012, blank, DIPQUO-loaded, GS4012-loaded, and dual-loaded CSNPs are shown in Figure 4.16. The characteristic absorbance peaks of CS with medium molecular weight were 3,313 and 3,262 cm^{-1}, which are due to -NH and -OH stretching in CS. These peaks might also be due to hydrogen bonds in the molecule. The 2,888 and 2,853 cm^{-1} peaks were -CH symmetric and asymmetric stresses, respectively. These bands are characteristic of polysaccharides and are also found in other polysaccharides. As residues of N-acetyl groups of CS structure peaks were found at 1,633 cm^{-1} (C=O stretching), 1,538 cm^{-1} (-NH stretching), 1,366 cm^{-1} (-CN stretching), and 1,010 cm^{-1} (C-O stretching) [106].

The TPP molecule exhibited characteristic peaks in FT-IR spectroscopy at 1,168, 1,128, 1,089, and 878 cm^{-1}. Stress vibrations of the group P=O appeared at 1,168 cm^{-1}, while the

peaks at 1,128 and 1,089 cm^{-1} belonged to PO_2 and PO_3 symmetric and asymmetric stresses, respectively. Asymmetric P-O-P stretching was presented at 878 cm^{-1} [107].

For Tween 20, the peak at 3,453 cm^{-1} was due to –OH stretching. The 2,880 and 2,851 cm^{-1} peaks were $–CH_2$ symmetric and asymmetric stresses, respectively. Besides, 1,729 cm^{-1} (C=O stretching), 1,448 cm^{-1} (bending of CH_2), 1,240 cm^{-1} (C-O ester bonds), and 1,084 cm^{-1} (C-O-C) peaks were observed [108,109].

In the single band region of DIPQUO, there was -OH stretch at 3,269 cm^{-1} and a C-H terminal stretch at 3,024 cm^{-1}. The peak originating from C=C strength was seen at 1,637 cm^{-1}. Primary and secondary amine stresses of 1,614 cm^{-1} and 1,574 cm^{-1}, respectively, were caused by the NH bend. In the fingerprint region, there was a C-O stretch at 1,147 cm^{-1} and 1,096 cm^{-1} and an alkyine C-H bend at 628 cm^{-1} [110].

C-H stretch in the terminal region of GS4012 at 3,052 cm^{-1}, C-H asymmetric and symmetrical stretches at 2,950 cm^{-1} and $N-CH_3$ stretch at 2,829 cm^{-1} were observed. In the double band region, alkenyl C=C at 1,632 cm^{-1} and C=C-C stretch at 1,594 cm^{-1} could be seen. The peaks found in the fingerprint region were 1,237, 800 and 637 cm^{-1}, showing aromatic ethers, aliphatic chloro compounds, and thioethers (C-S stretch), respectively [110].

The peaks originating from -NH and -OH stretching in the CSNPs were found to expand to 3,381, 3,256 and 3,147 cm^{-1} peaks, respectively, for blank NPs. Although, the peakt at 1,633 cm^{-1} in the CS was found to be protected in NPs, the peak at 1,538 cm^{-1} shifted to 1,535 cm^{-1}. A new peak formation originating from the P=O bond was observed at 1,193 cm^{-1} [111].

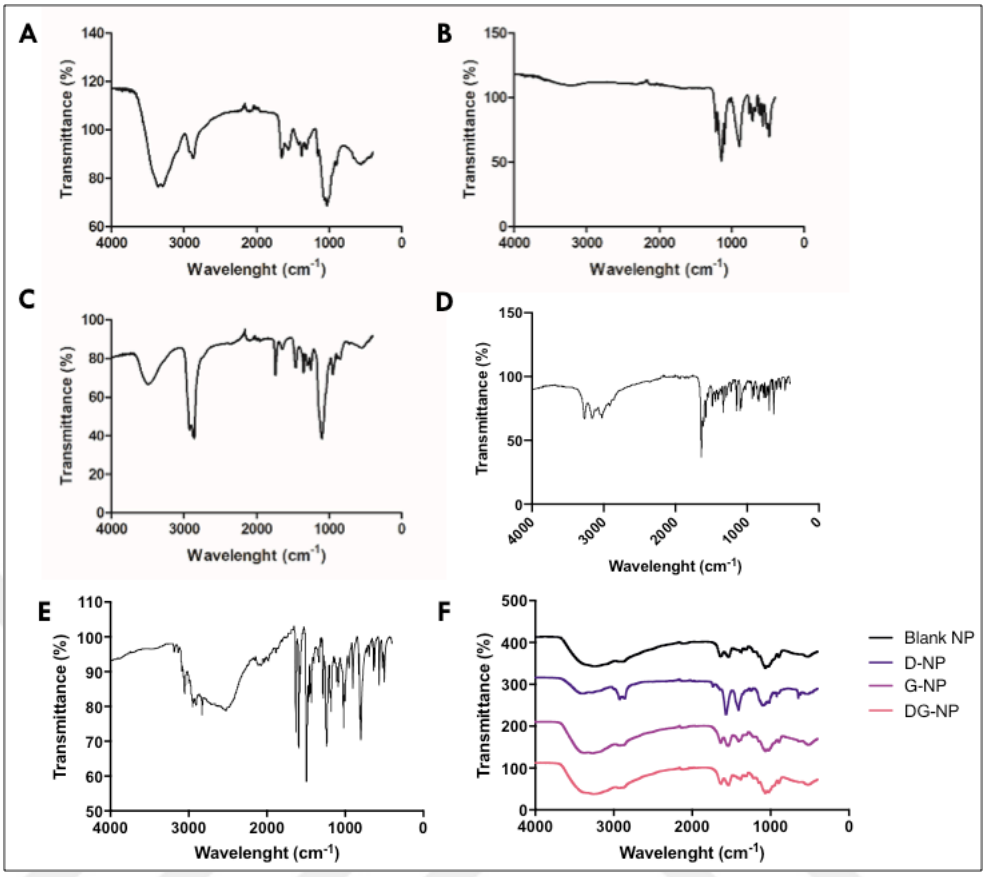


Figure 4.16 FT-IR spectra of (A) chitosan, (B) TPP, (C) Tween 20, (D) DIPQUO, (E) GS4012, and (F) blank and loaded NPs.

4.2.4. DSC

The phase transition curves of CS, TPP, and Tween 20 together with blank, and loaded NPs are presented in Figure 4.17. In the CS thermogram, an endothermic peak occurred at 115°. One endothermic peak at 90° was revealed by a Tween 20 thermogram. In addition, the thermogram of TPP showed two endothermic peaks at 37° and 119°.

Blank NPs had a single sharp endothermic peak at 67° and a wide peak at 117°. D-NP had endothermic peaks at 67° and 122°, and G-NP had an endothermic peak at 90° and an exothermic peak at 249°. Like the blank NP, the DG-NP showed a sharp endothermic peak at 66° and a broad peak at 133°.

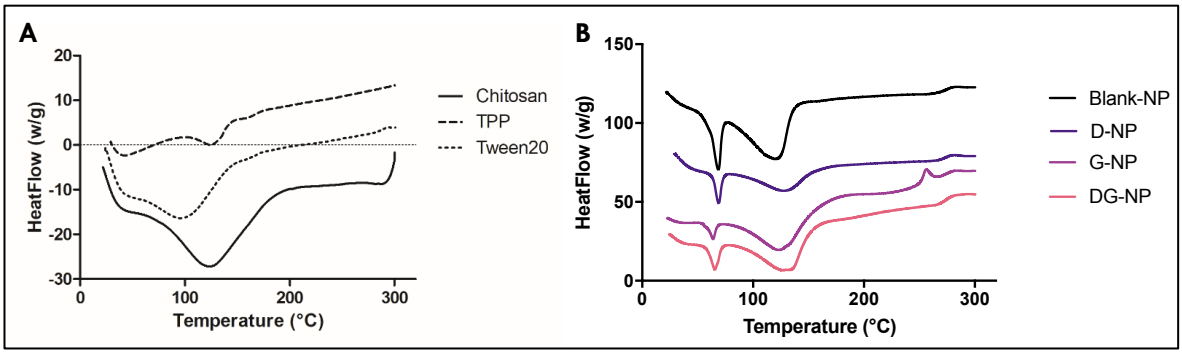


Figure 4.17 DSC spectra of (A) chitosan, TPP, and Tween 20, and (B) blank and loaded NPs.

4.2.5. Evaluation of NP Encapsulation Efficiency and Loading Capacity

As a result of the spectra scanning, the absorption peaks for DIPQUO were found to be 261 and 363 nm, while this value was determined as 252 nm for GS4012 (Figure 4.18).

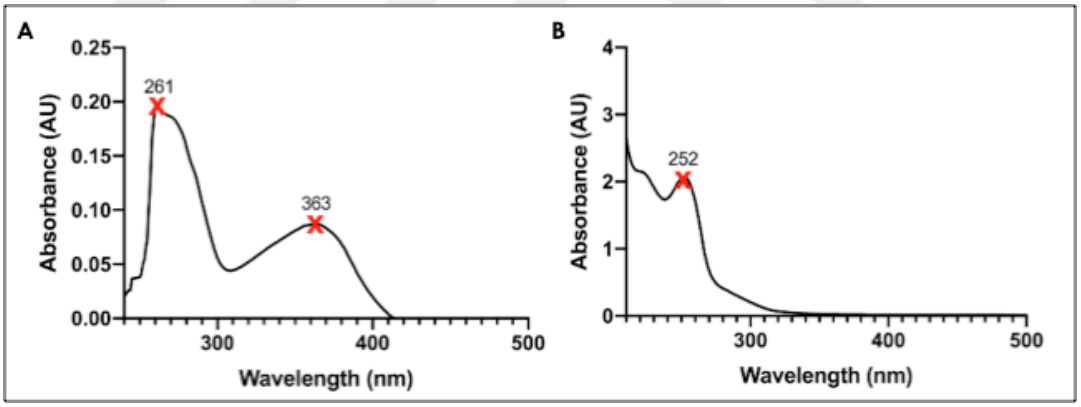


Figure 4.18 Absorbance peaks of (A) DIPQUO, and (B) GS4012.

EE and LCs of NPs synthesized under different conditions are shown in Table 4.3. While the encapsulation efficiency was 87% on average for DIPQUO under optimum conditions, this value decreased to 80% during dual encapsulation. For GS4012, while the EE value was around 89% in single encapsulation, this value decreased to 75% during dual encapsulation. The LC values of the synthesized NPs varied between 18-60% (Table 4.5).

4.2.6. Evaluation of NP Yield Analysis

Yield analyses of NPs synthesized under different conditions are shown in Table 4.5. It was seen that the reaction yield varied between 50 and 70% under optimum conditions.

Table 4.5 Reaction yield, encapsulation efficiency and loading capacity results of NPs.

Sample	Reaction Yield(%)	EE (%)	LC (%)
Blank-NP	52.46 ± 3.10		
D-NP	69.54 ± 8.23	87.67 ± 13.39	32.32 ± 17.71
G-NP	56.03 ± 2.02	89.97 ± 8.44	59.50 ± 19.07
DG-NP	60.58 ± 7.47	79.37 ± 13.84[1] 75.15 ± 10.95[2]	41.52 ± 4.22[1] 17.36 ± 0.86[2]
B-NP	28.33 ± 5.44	28.56 ± 3.31	30.43 ± 9.24

[1]This data belongs to DIPQUO

[2]This data belongs to GS4012

4.2.7. *In vitro* Release Study of the CS Nanoparticles

As a result of the *in vitro* release study, it was seen that the NPs released 37% of the BSA content with a rapid release in the first 3.5 h, then the release slowed down and 50% was released at the end of day 3, then it took a total of 20 days to complete (Figure 4.19A).

As a result of the *in vitro* small molecule release study, it was seen that the NPs released 71% of the DIPQUO content with a rapid release in the first 3 h, then the release slowed down and 76% was released at the end of day 1, then it took a total of 11 days to complete. In the GS4012 loaded NPs, 38% of the GS4012 content was released rapidly in the first three h, then the release slowed and 54% was released at the end of day one, taking a total of 13 days to complete. In dual NPs, DIPQUO content released quickly (69% in 3 h) but took 11 days to complete release, whereas GS4012 content released quickly (41% in 3 h) but took 13 days to complete (Figure 4.19B).

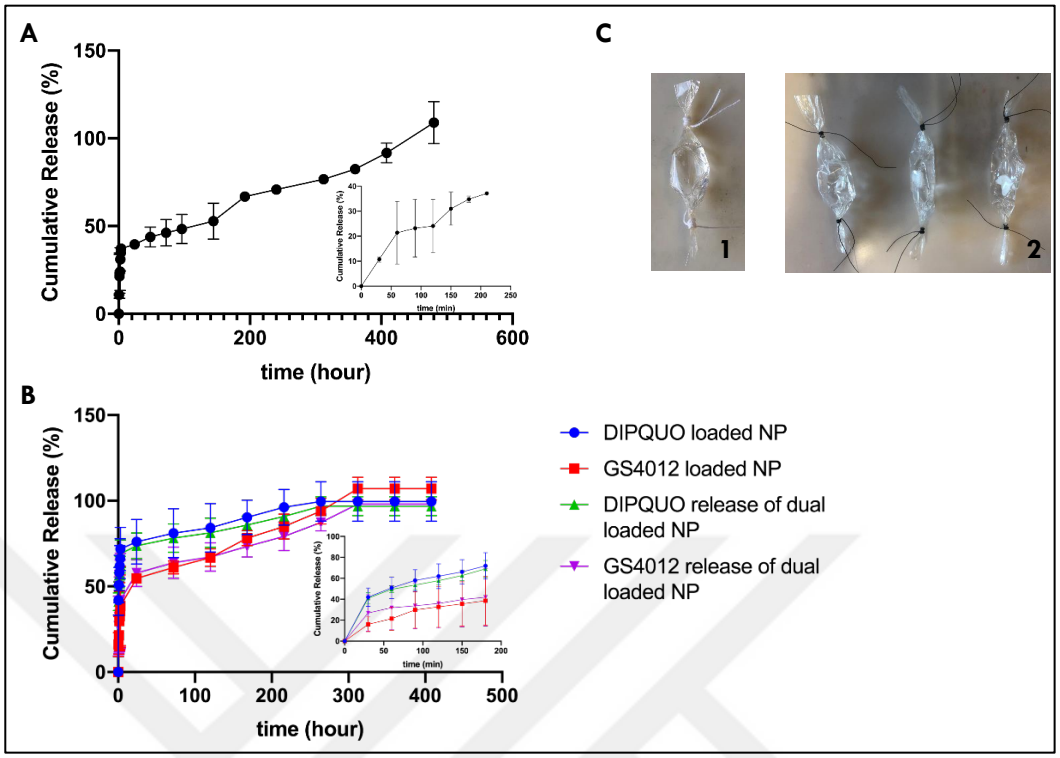


Figure 4.19 *In vitro* release study of (A) BSA loaded chitosan NP, and (B) small molecule loaded chitosan NP, (C) Dialysis bags with (1) BSA loaded NPs and (2) small molecules loaded NPs.

4.2.8. Determination of Half Maximal Inhibitory Concentration

The half maximal inhibitory concentration values of the small molecules were calculated, and a log concentration graph was drawn against the normalized absorbance values (Figure 4.20). As a result of the study, the IC50 value of DIPQUO was found to be 5.47 µM (1.72 µg/mL), while that of GS4012 was found to be 25.18 µg/mL (89.36 µM).

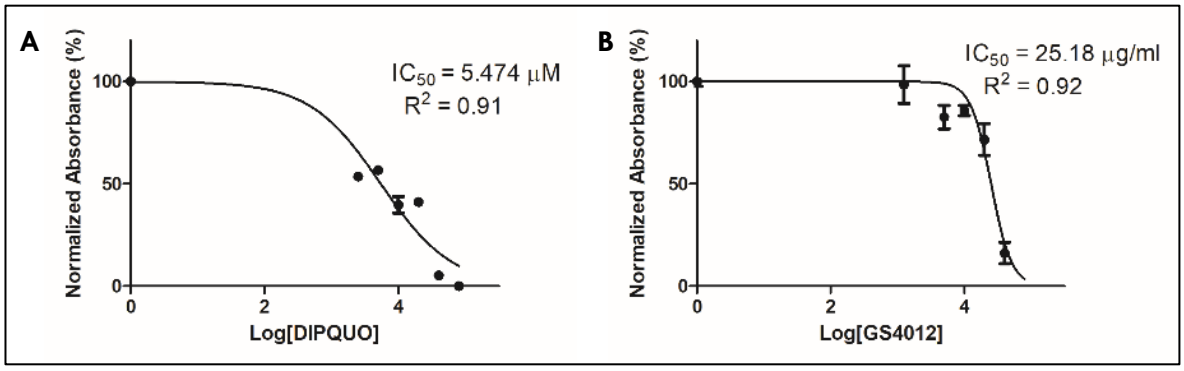


Figure 4.20 The half maximal inhibitory concentration graphs of (A) DIPQUO, and (B) GS4012.

4.3. NP COATING OF SCAFFOLDS

While the surface of the scaffolds was coated, several different methods were applied. Then, the quantity of NP adhered to the surface was examined by the SEM analysis (Figure 4.21). The best results were obtained after treating the scaffolds with 0.5 M NaOH for 4 h, adding NPs directly to the treated scaffolds, and then drying them with a vacuum dry dessicator.

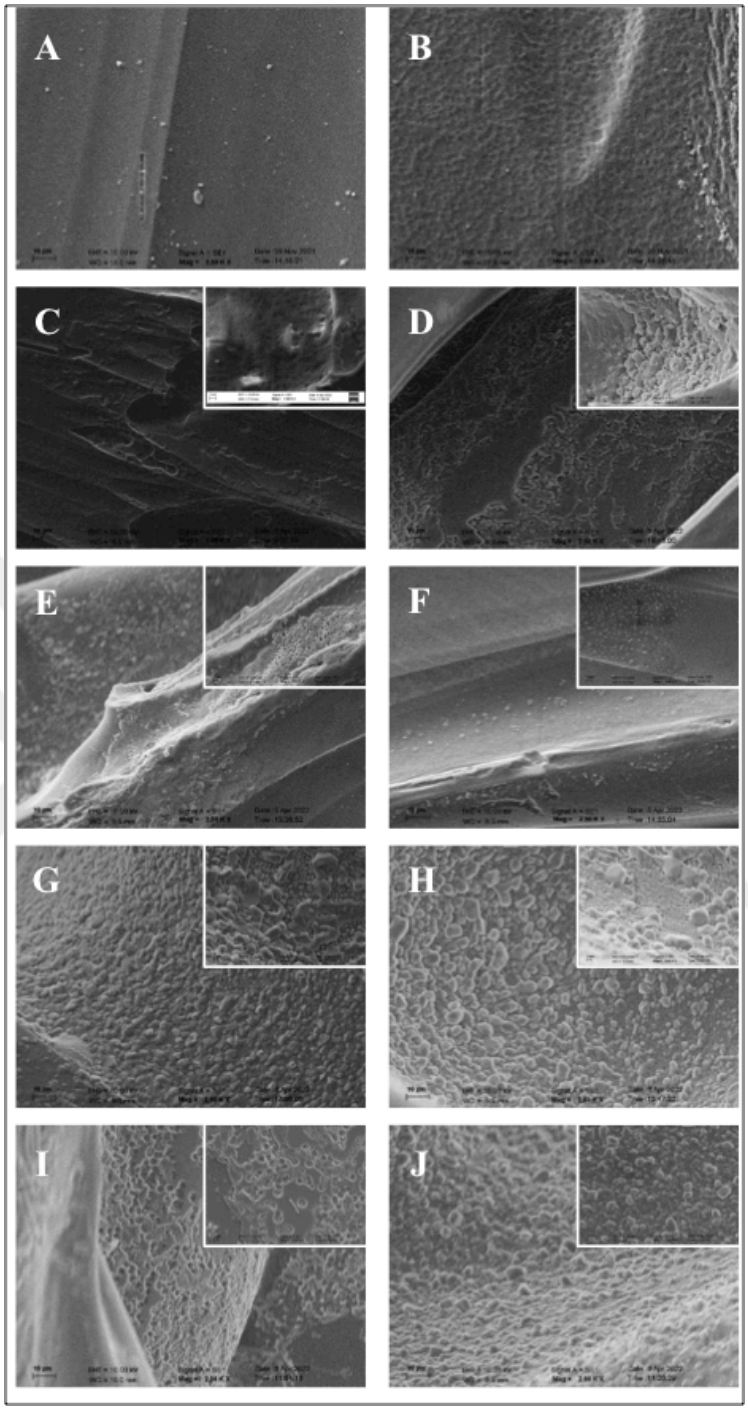


Figure 4.21 Scanning electron micrographs of (A) untreated, and (B) alkaline treated (0.5 M NaOH for 4 h) scaffolds that were coated with NPs either by mixing them on a magnetic stirrer and then air-drying (C, D, E, F) or by adding them directly and drying in a vacuum desiccator (G, H, I, J). Scaffolds treated with (C, G) 1.25 M NaOH for 2 h, (D, H) 1.25 M NaOH for 4 h, (E, I) 0.5 M NaOH for 2 h, and (F, J) 0.5 M NaOH for 4 h. Scale: 10 μm and indent scale: 2 μm.

4.4. *IN VITRO* CELL CULTURE STUDIES

4.4.1. Characterization of rBMSCs

rBMSCs were stained with von Kossa, alizarin red, alcian blue, and oil red O to confirm the multipotent capacity of cells for differentiation.

4.4.1.1. Osteogenic Differentiation

The osteogenic differentiation capacity of rBMSCs was evaluated using von Kossa and alizarin red staining at 7, 14, and 21 days in culture. When the microscope images of von Kossa staining are examined (Figure 4.22A), it was observed that, as the day progressed, the mineralization in the OM group was considerably higher than in the GM group. The mineralized parts were observed in gray, while the cell cytoplasm appeared in pink. Alizarin red was used to stain calcium deposits (Figure 4.22B). Also, the red areas in the OM group increased, indicating that the mineralization increased with time and rBMSCs differentiated into osteoblasts.

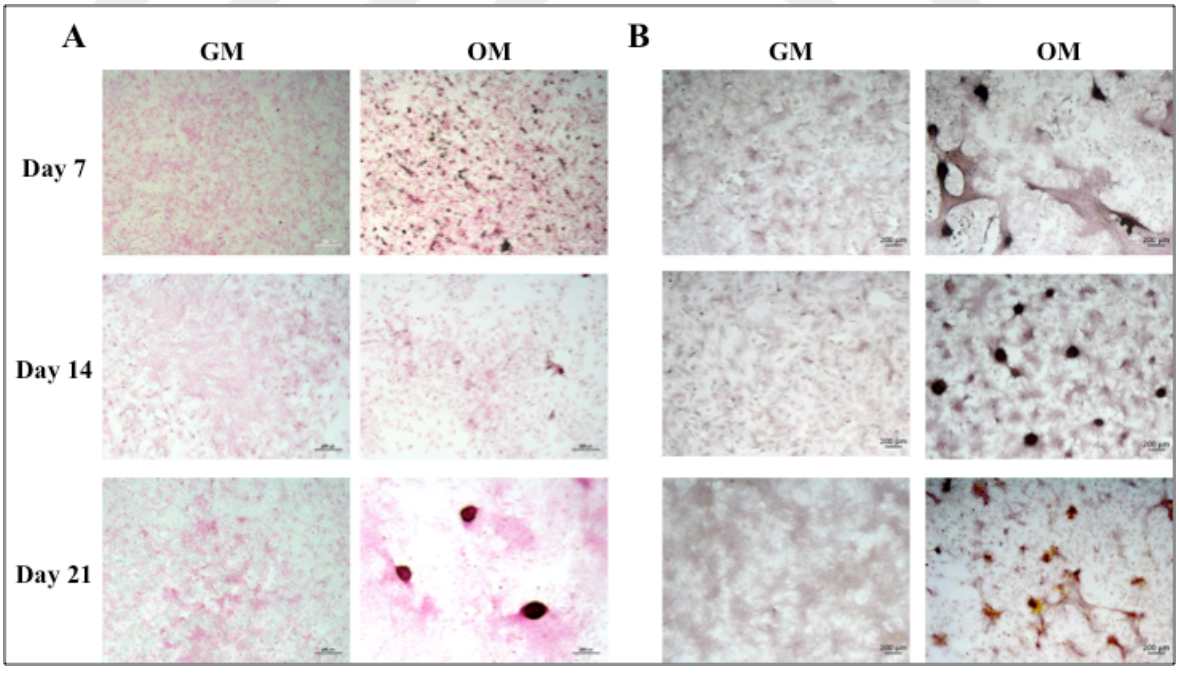


Figure 4.22 Osteogenic differentiation stainings of rBMSCs in GM and OM by (A) von Kossa, and (B) alizarin red stainings, scale: 200 μm.

4.4.1.2. Chondrogenic Differentiation

The chondrogenic differentiation capacity of rBMSCs was evaluated using alcian blue-PAS staining at 7, 14, and 21 days in culture. In this staining, acid mucins and proteoglycans are stained blue, while cell nuclei are stained pale blue, and neutral mucins, glycogen, and various glycoproteins are stained pink/red. Looking at the microscope images of the alcian blue staining, it was observed that as the day progressed, the ECM secreted from the chondroblasts in the CM group was considerably higher than in the GM group. Especially at the end of 21 days, it was observed that rBMSCs differentiated into chondrocytes in cell culture, forming ECM (Figure 4.23).

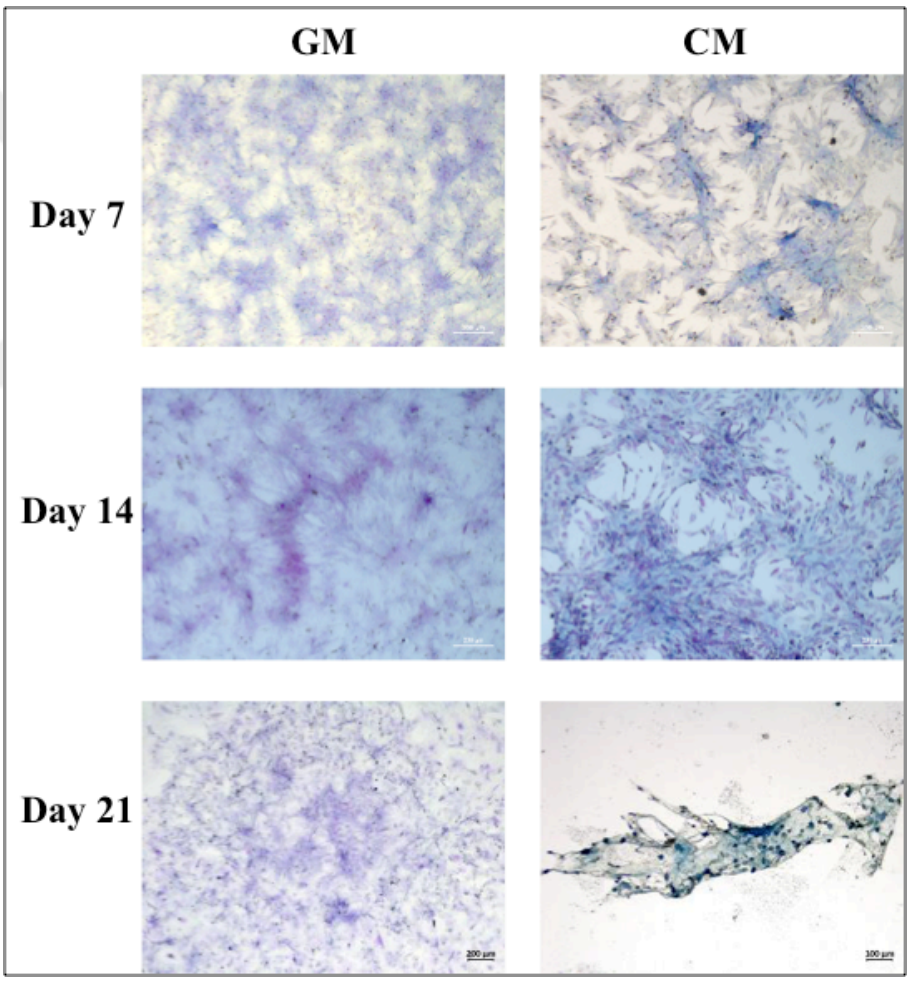


Figure 4.23 Chondrogenic differentiation of rBMSCs in GM and OM bu alcian blue-PAS staining, scale: 200 µm.

4.4.1.3. Adipogenic Differentiation

The adipogenic differentiation capacity of rBMSCs was evaluated using oil red O staining at 7, 14, and 21 days in culture. Lipid materials were stained with oil red O dye and these lipids were observed with a red-orange color. When the microscope images of the stains were examined, it was observed that the number of oil drops in the AM group was higher than the GM group as the day progressed. Especially at the end of 21 days, the oil droplets in the cells were clearly observed. rBMSCs exhibited oily vesicles and lipid droplets, which are similar to those of adipocyte cells (Figure 4.24).

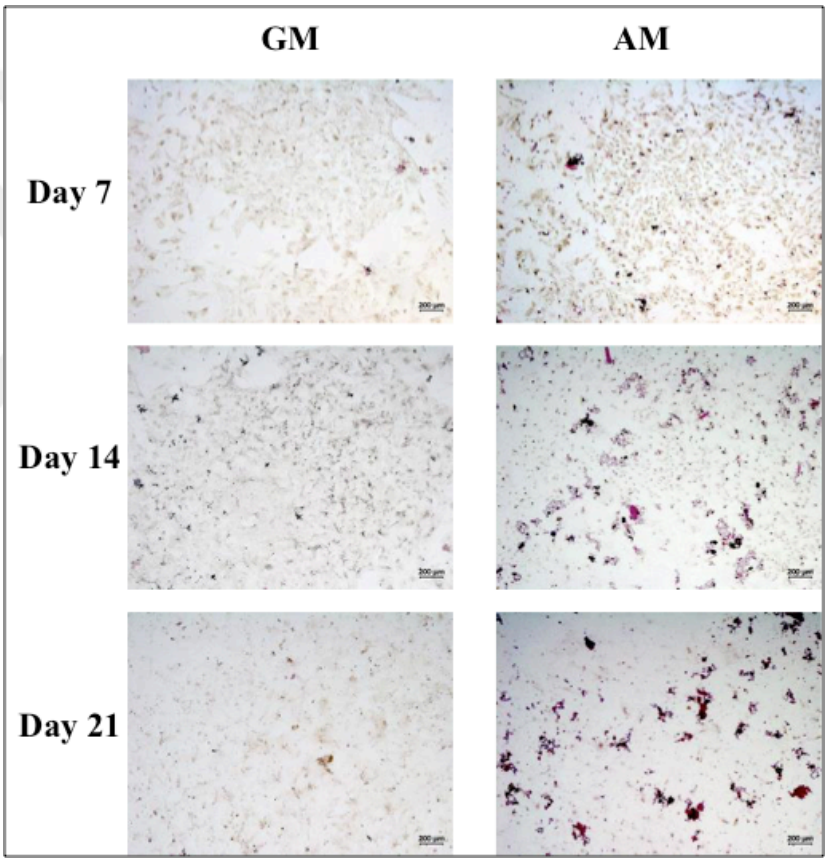


Figure 4.24 Adipogenic differentiation stainings of rBMSCs in GM and OM by oil red O, scale: 200 μm.

4.4.1.4. Flow Cytometry Analysis

The expression of MSC markers in the isolated rBMSCs was evaluated by flow cytometry. With this analysis, rBMSCs were characterized using specific surface markers. According to the flow cytometry analysis, these cells were stained positive for CD90 (99.66%), CD29 (99.57%), and negative for CD45 (2.35%), and CD34 (2.26%) (Figure 4.25).

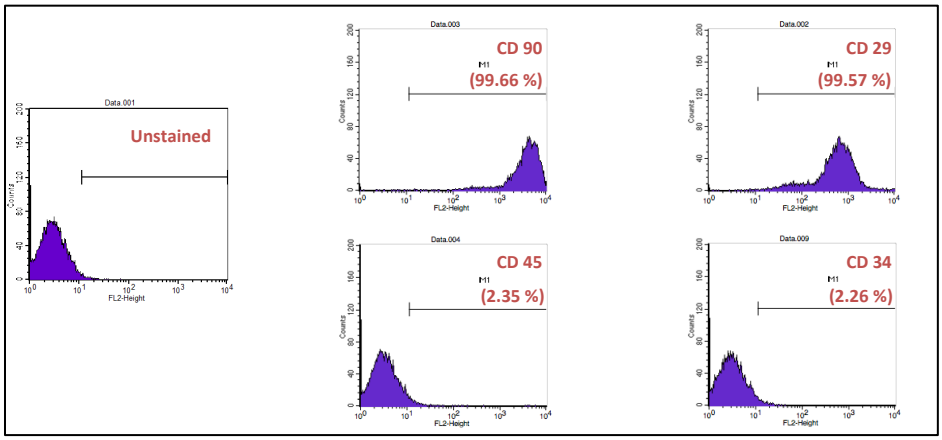


Figure 4.25 Flow cytometry analysis of rBMSCs stained with CD90, CD29, CD45, and CD34.

4.4.2. Characterization of rPBECs

Cells isolated from peripheral blood were grown in cell culture with EBM media. Images are shown in Figure 4.26.

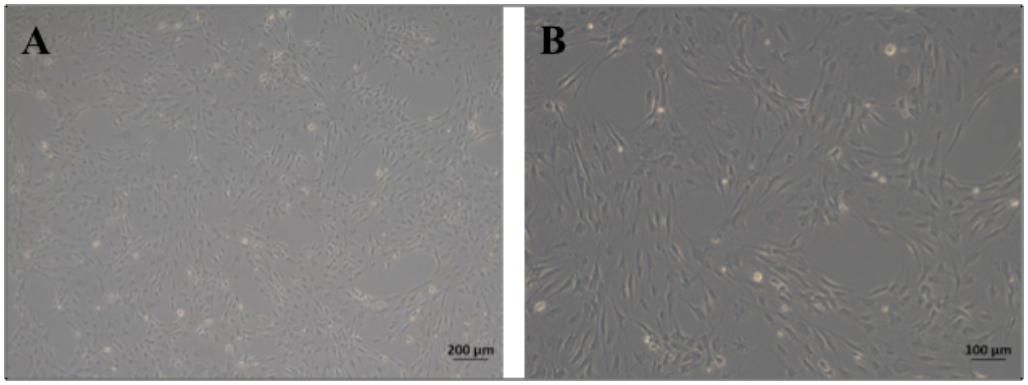


Figure 4.26 Bright field images of rPBECS with a scale of (A) 200 µm, and (B) 100 µm.

4.4.2.1. CD31 (PECAM-1)

Since CD31 antibody is a surface marker specific to endothelial cells, it was used in the characterization of isolated rPBECs. The CD31 dye was seen in green under fluorescence microscopy, and the cell nuclei were observed in blue with DAPI (Figure 4.27). All cells exhibited a green glow. This proves that all cells in culture showed endothelial cell characteristics.

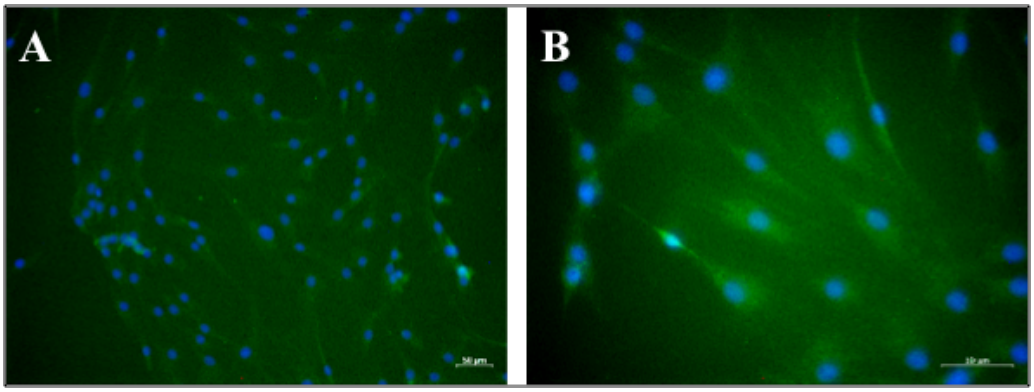


Figure 4.27 Fluorescent microscopy images of rPBECS labeled with CD31 (PECAM). Magnification: (A) 20X, and (B) 40X. Green: CD31, Blue: DAPI.

4.4.2.2. Dil acetylated low-density lipoprotein (Dil-Ac-LDL)

The uptake capacity of labeled low-density lipoprotein Dil-Ac-LDL into rPBECs was investigated. Figure 4.28 shows the combined BF image, DAPI-stained cell nuclei, LDL-stained endothelial cells, and fluorescence and BF microscope images, respectively.

In the study performed with a fluorescent microscope, it was seen that all cells in culture emit a red color. The nuclei of the cells were stained with DAPI and observed in blue. When the BF image and all the fluorescent images were merged, it was observed that there was no different cell in the environment. All cells in the cell culture showed endothelial cell characteristics, and there was no cross-contamination.

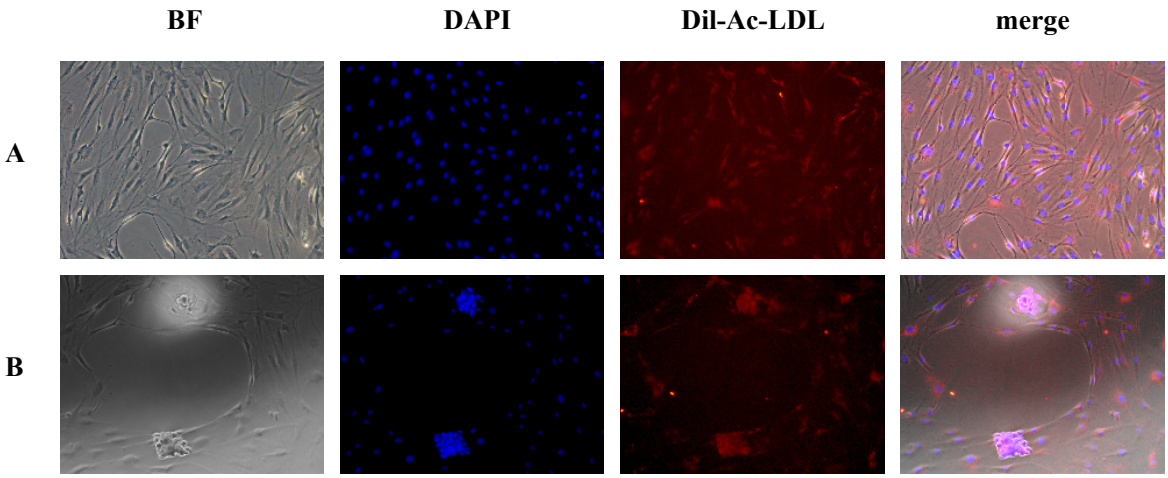


Figure 4.28 rPBECs after the Dil-Ac-LDL uptake study. Magnification: (A) 10X, and (B) 20X.

4.4.3. Cell Labeling

Fluorescent staining with cell membrane dyes was performed for both rPBECs and rBMSCs. In Figure 4.29, it was observed that the cell membranes of rBMSCs glowed red, while in Figure 4.30, the cell membranes of rPBEC cells glowed green. It was seen that all of the cell membranes were stained successfully and exhibited a bright glow in both staining types.

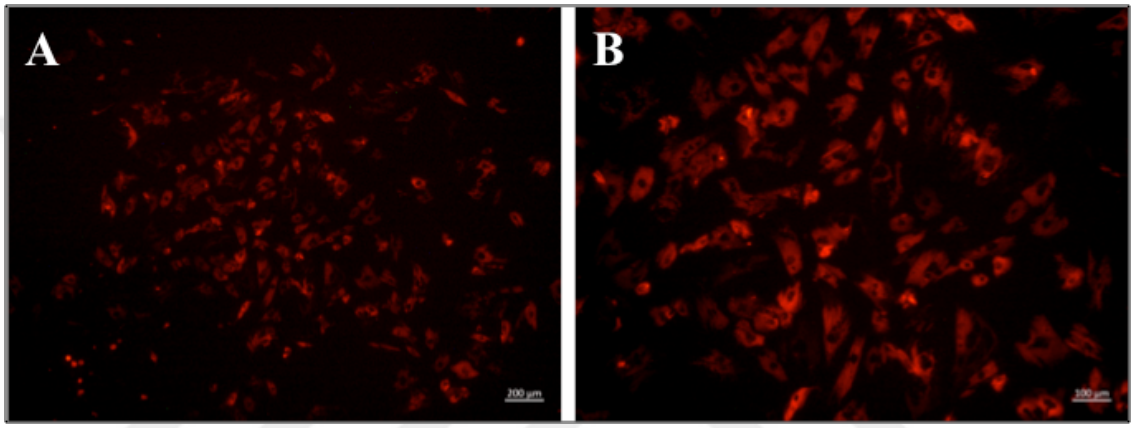


Figure 4.29 Fluorescence microscopy images of red fluorescent-labeled rBMSCs with a scale of (A) 200 µm, and (B) 100 µm.

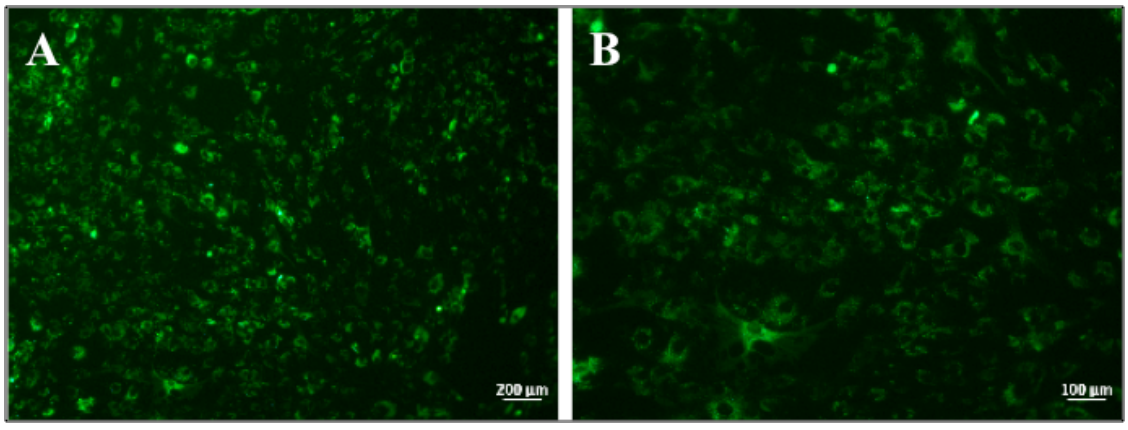


Figure 4.30 Fluorescence microscopy images of vybrant-labeled rPBECs with a scale of (A) 200 µm, and (B) 100 µm.

4.5. *IN VITRO* MATERIAL-CELL INTERACTIONS

4.5.1. PLA Scaffold-Cell Interactions

4.5.1.1. Cell Viability by MTS Assay

The viability of the cells was evaluated using the MTS assay (Figure 4.31). In the study performed with 3T3-seeded scaffolds (Figure 4.31A), it was observed that the number of cells increased rapidly until day 7; however, the number decreased sharply by day 14 and increased again towards day 21. At the end of days 7, 14, and 21, a significant difference was observed in the cell viability of the scaffold with a 60% filling rate compared to the other groups. In the study conducted with rBMSC-seeded scaffolds (Figure 4.31B), a significant difference was observed between the scaffolds with 50 and 60% filling rates at the end of 1, 14, and 21 days, while on the 7^{th} day, the scaffold with an 80% filling rate differed significantly from the 90% one.

To analyze the proliferation of differentiated rBMSCs on different scaffolds, an MTS assay was performed. OM was used to ensure osteogenic differentiation of rBMSCs. After MTS analysis on day 7, it was seen that the differentiated cell number in the scaffolds with a 60% filling rate was higher than the others, and this difference was significant (Figure 4.31C). However, at the end of day 21, this significant difference disappeared, and there was no significant change between the scaffold types.

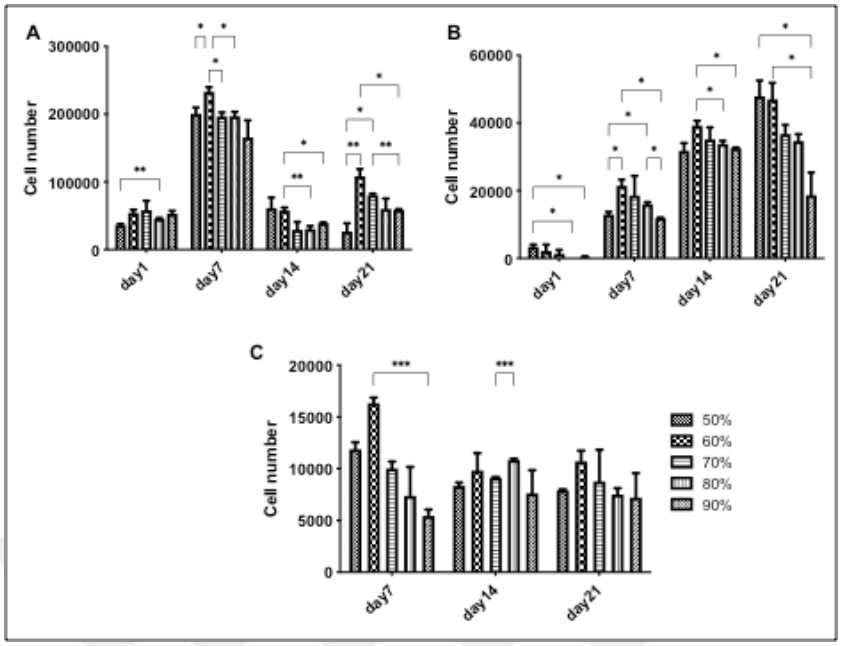


Figure 4.31 Cell viability by MTS assay in 3D-printed PLA scaffolds that were seeded with (A) 3T3 in DMEM growth medium, (B) rBMSCs in MEM-a growth medium, and (C) rBMSCs in OM with a density of 5 x 10^4 cells, n=3, $p < 0.05$.

Cell viability tests were performed in Corbion brand PLA scaffolds, with optimal pore size obtained at a filling rate of 60%. This assay was maintained for 1, 7, 14, and 21 days using rBMSCs and two different media (GM and OM) (Figure 4.32). According to the results, rBMSCs continued to proliferate on the scaffold surface in GM, and the number of cells increased by the end of the 21-day period. When the same study was performed with OM, it was seen that the number of cells remained constant.

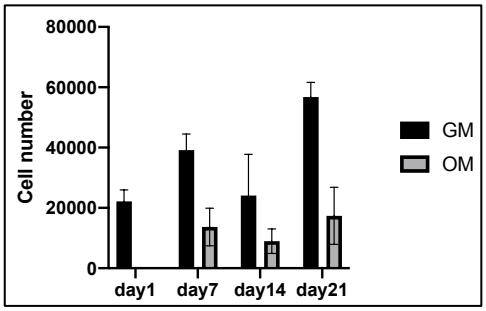


Figure 4.32 Cell viability by MTS assay in 3D-printed PLA (Corbion) scaffolds with a 60% filling rate that were seeded with rBMSCs in GM or OM with a density of 5 x 10^4 , n=3.

4.5.1.2. Live-Dead Assay

At the end of the Live-Dead assay, it was observed that rBMSCs extended along the PLA surface and connected with each other between the pores (Figure 4.33A). After day 1, the adhesion and proliferation of rBMSCs on the scaffold surface were clearly distinguished. Especially at the end of day 1, as the filling rate of the scaffolds increased, a higher number of cells was seen. While the density of cells in the scaffolds with a 90% filling rate did not significantly increase as the time passed, the density of viable cells increased throughout the 21 days of incubation in the scaffolds with low filling rates. The percentage of viable and dead cells in the total area was obtained (Figure 4.33B,C). The number of viable cells in the total area was found to be around 90% for all scaffold types. It was observed that the number of dead cells in the total area decreased as the incubation day progressed, but this difference was not significant.

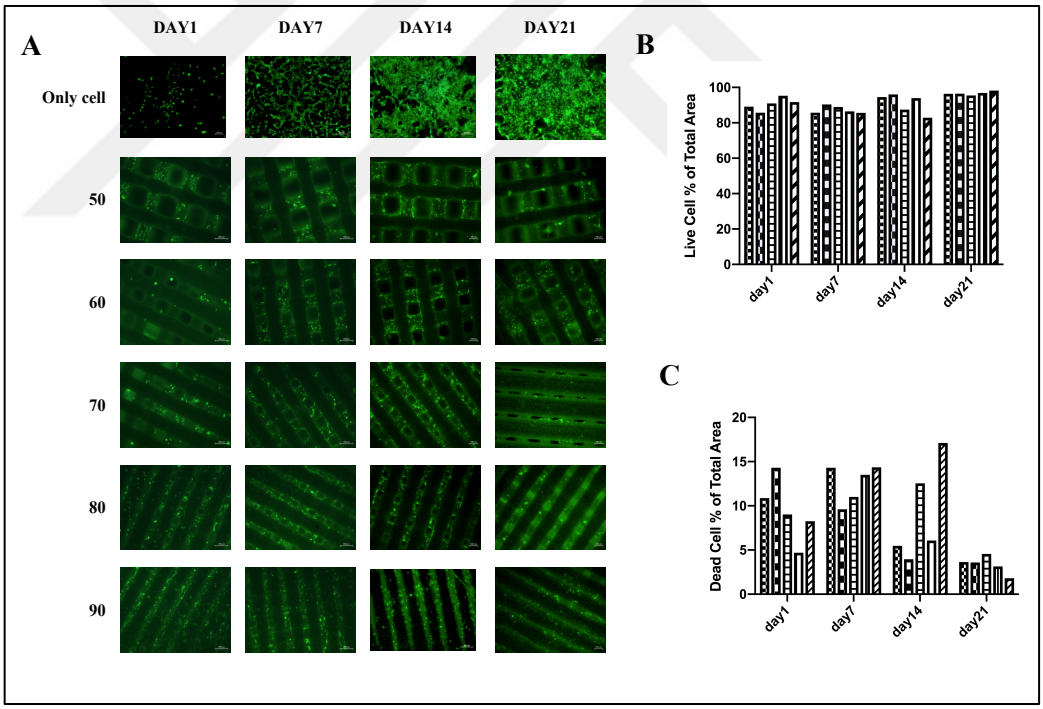


Figure 4.33 (A) Cell viability by Live-Dead assay in 3D-printed PLA (BASF) scaffolds that were seeded with rBMSC throughout 1, 7, 14, and 21 days of incubation (dead cells: red; live cells: green), scale: 200 µm. Graphs of (B) live cells and (C) dead cells as a percentage of total area.

At the end of the Live-Dead assay, it was observed that rBMSCs adhered to the PLA surface similar to other scaffolds, extended along the lines, and interconnected between the

pores (Figure 4.34). It was clearly observed that the adhesion and proliferation of rBMSCs on the scaffold surface increased as the day in culture extended. On the scaffolds, viable cell density increased during the 21-day incubation.

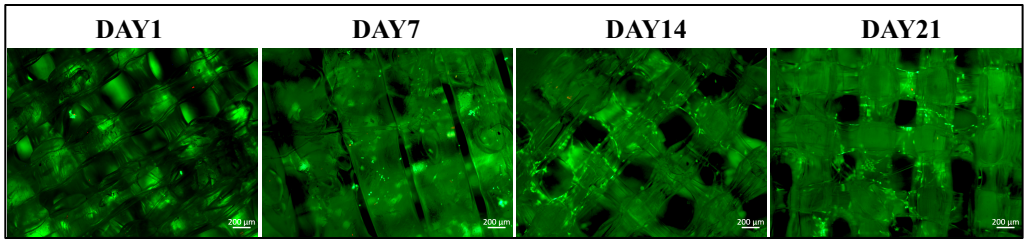


Figure 4.34 Cell viability by Live-Dead assay in 3D-printed PLA (Corbion) scaffolds with 60% filling rate that were seeded with rBMSC throughout 1, 7, 14, and 21 days of incubation (dead cells: red; live cells: green), scale: 200 µm.

4.5.1.3. Cell Proliferation by PicoGreen Assay

To detect the DNA amounts and compare the cell proliferation inside the scaffolds, a PicoGreen assay was performed (Figure 4.35). It was observed that scaffolds with a 50% filling rate had more cells and more DNA on day 7, but this difference was not significant. However, when the five types of scaffolds were compared with each other, a significant difference was observed in terms of DNA on day 14.

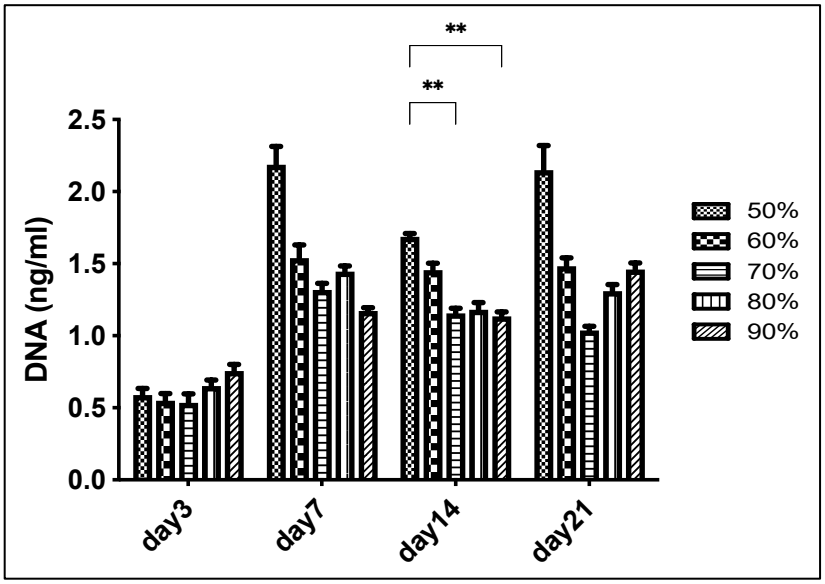


Figure 4.35 Cell proliferation (PicoGreen) assay of rBMSC seeded scaffolds; $p < 0.05$.

4.5.1.4. Alkaline Phosphatase Activity

The results of the study examining ALP activity are shown in Figure 4.36. It was observed that the ALP activity of cells in scaffolds with 60% filling rates increased significantly on day 3 and then decreased and did not change considerably. Likewise, with the 50% filling rate scaffolds, ALP activity decreased after day 3. In scaffolds with 70 and 80% filling rates, ALP activity increased and stabilized, but this increase was not significant. In scaffolds with a 90% filling rate, an increase in ALP was observed until day 7, then stabilized and did not change until day 21.

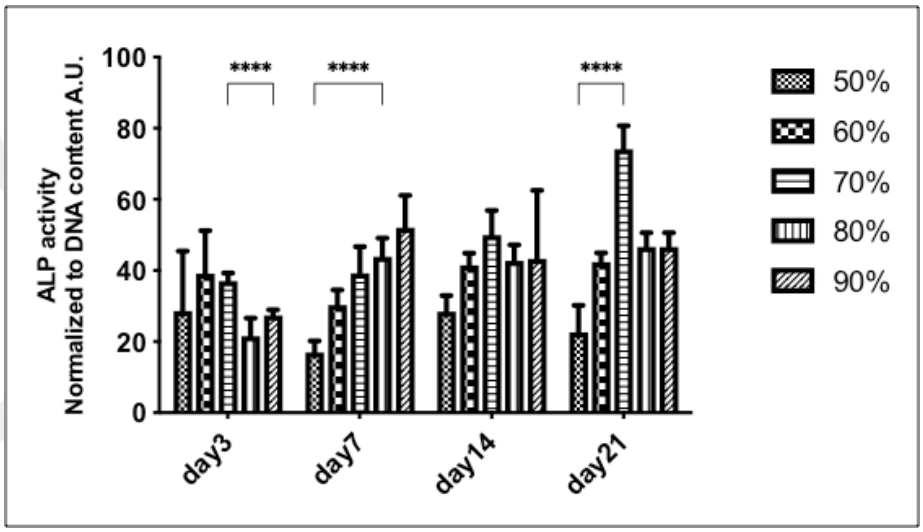


Figure 4.36 ALP analysis after 3, 7, 14, and 21 days of culturing. The data were normalized against DNA content; n=3, $p < 0.05$, ****$p < 0.0001$.

4.5.1.5. von Kossa Staining

After von Kossa staining, the cell cytoplasm stained pink, while calcium deposits stained brown. It was observed that the cells differentiated into osteoblasts and accumulated calcium in OM (Figure 4.37). While this accumulation was less on day 7, it increased on day 14 and covered almost all scaffold surfaces on day 21. On the contrary, while calcium accumulation was not observed in cells grown in GM, the number of cells increased, and a more pinkish color covered the scaffold surfaces.

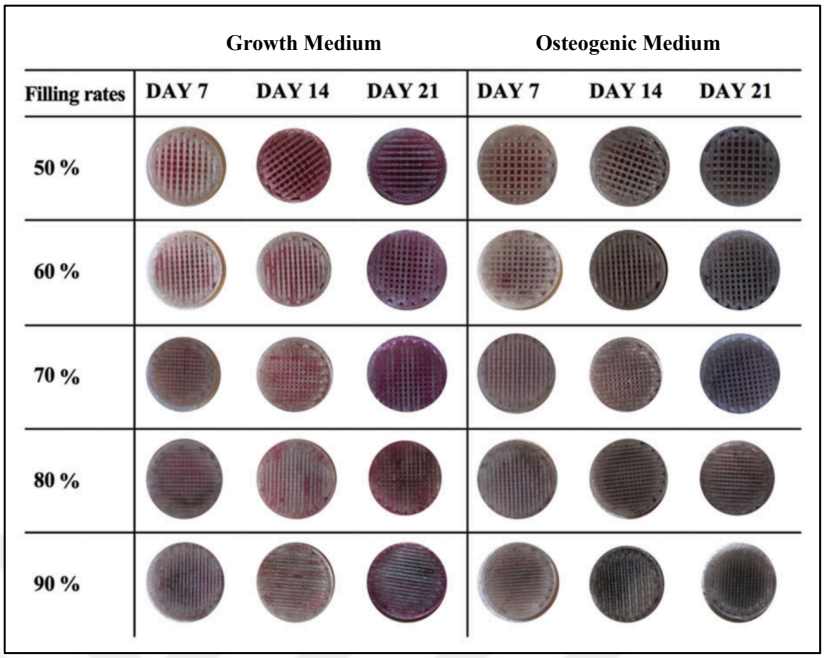


Figure 4.37 von Kossa staining of scaffolds in growth medium (GM) and osteogenic medium (OM) after 7, 14, and 21 days in culture.

As a result of the study with PLA scaffolds with different pore sizes, it was seen that the most suitable pore size for BTE applications was obtained with a scaffold with a 60% filling rate. In the following parts of the study, only this type of scaffold was used.

4.5.2. Chitosan Nanoparticle-Cell Interactions

4.5.2.1. Cell Viability by MTS Assay

The viability of the rBMSCs was assessed using the MTS assay. In this study, 50,000 cells were seeded in 6-well transwells, and inserts containing NP were added to the cells the next day. rBMSCs were analyzed at the end of day 7. As can be seen in Figure 4.38, GS4012-loaded NPs showed a significant difference compared to the other groups, while the DIPQUO-loaded group had a more toxic effect than the other groups, causing a decrease in the number of cells.

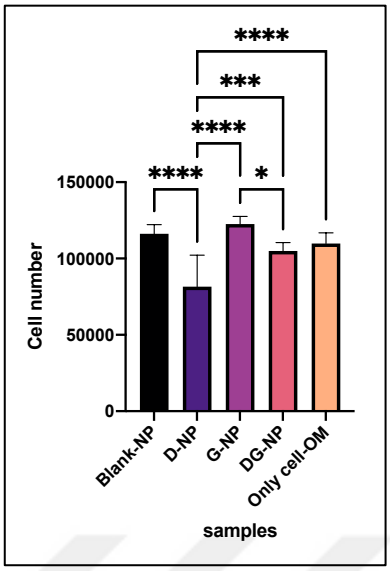


Figure 4.38 rBMSCs viability upon NP application by MTS assay. Cells were seeded at a density of 5 x 10^4 in DMEM growth medium, n=3, $p < 0.05$.

4.5.2.2. Alkaline Phosphatase Activity

The results of the study examining ALP activity are shown in Figure 4.39. It was observed that the ALP activity of cells with D-NP increased significantly on day 3 and then decreased and did not change considerably. Likewise, with all treatment groups, ALP activity decreased after day 3. It was seen that ALP activity in cells treated with DG-NP on day 14 showed a significant difference against other groups, especially against blank NP.

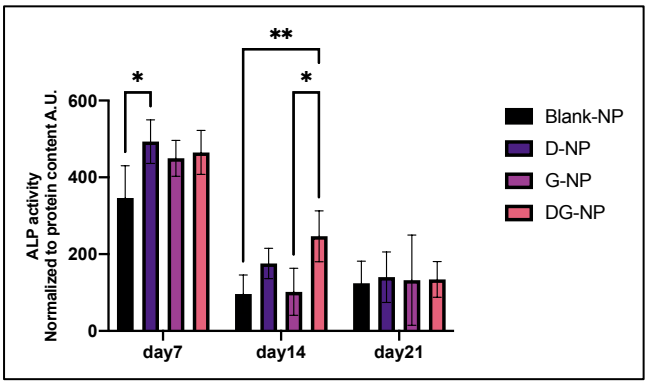


Figure 4.39 ALP analysis after 7, 14, and 21 days of culturing. The data were normalized against protein content, n=3, $p < 0.05$.

4.5.2.3. Hematoxylin&Eosin Staining

In the study carried out in transwells, rBMSCs were treated with different NPs, and the study was continued in culture for 21 days. At the end of 7, 14, and 21 days, cells were fixed and stained with H&E (Figure 4.40). Cell nuclei were stained purple with hematoxylin, while ECMs were stained pink with eosin. In culture, ECM appeared to increase for all groups as the day progressed. After 21 days, the ECM density appeared to be higher in the G-NP treated group compared to the other groups.

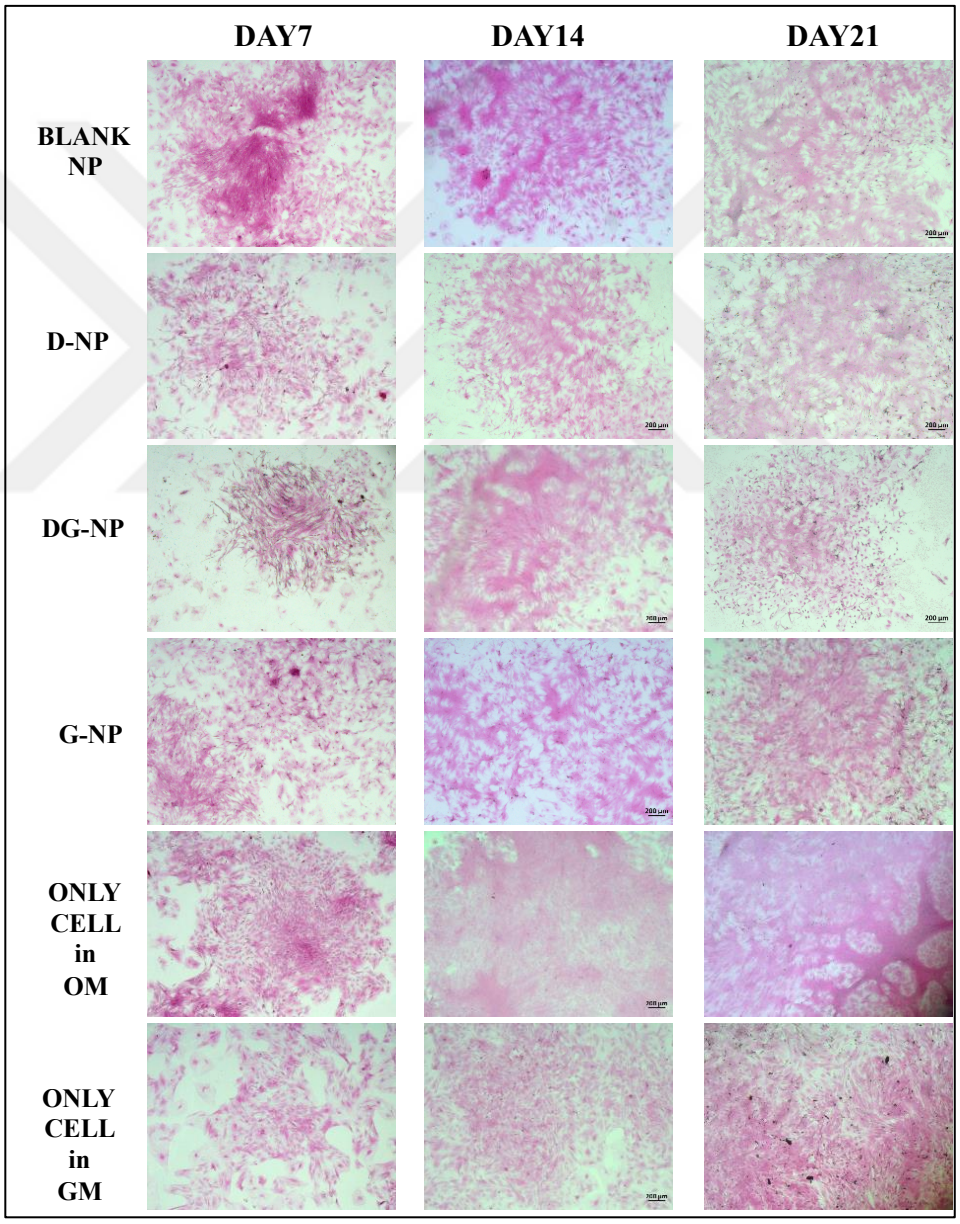


Figure 4.40 Hematoxylin & Eosin staining of NP treated cells in OM after 7, 14, and 21 days in culture, scale:200 μm.

4.5.2.4. Alizarin Red Staining

In the study carried out in transwells, rBMSCs were treated with different NPs. At the end of 7, 14, and 21 days, cells were fixed and stained with alizarin red (Figure 4.41). With this staining, calcium-containing osteocytes appeared in red. It was observed that calcium accumulation increased as the day progressed in all groups. Even in the first days, it was seen that osteogenic differentiation began in groups treated with NP containing DIPQUO (D-NP). This difference between cells treated with D-NP alone and the other treatment groups became much more pronounced after 21 days. While calcium accumulations were also seen in blank NPs, this differentiation was not as strong as in small molecule-loaded NPs.

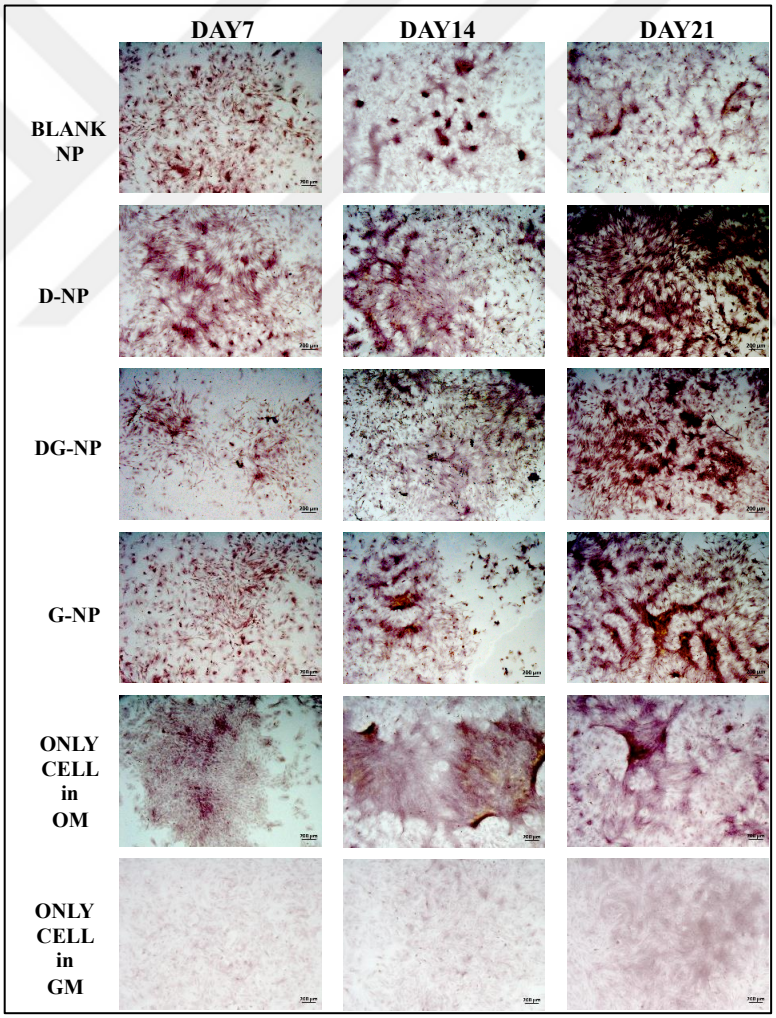


Figure 4.41 Alizarin red staining of NP treated cells in OM after 7, 14, and 21 days in culture, scale:200 µm.

4.5.2.5. von Kossa Staining

In this study, rBMSCs were treated with different NPs in transwells. At the end of 7, 14, and 21 days, the cells were fixed and stained with von Kossa (Figure 4.42). With this staining, mineralization in the cells became visible. It was observed that as the day progressed in all groups, the accumulation of mineralization increased with the number of cells. Mineralization was higher in the D-NP and DG-NP treated groups after 7 days in culture, and this difference was greater in the D-NP treated group after 21 days. The G-NP treated group came forward with its excess ECM secretion. While mineralization appeared similar to alizarin red staining in blank NPs, it was seen that these accumulations were not as many as other groups.

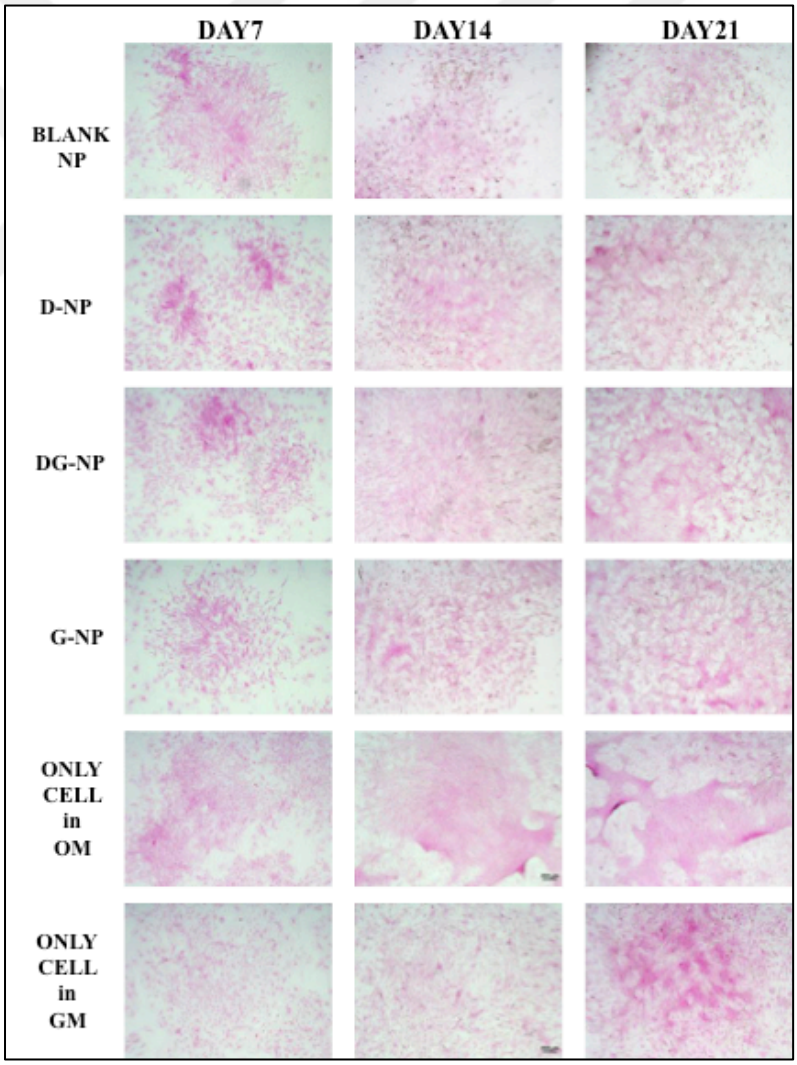


Figure 4.42 von Kossa staining of NP treated cells in OM after 7, 14, and 21 days in culture, scale:200 µm.

4.5.3. NP Coated PLA Scaffold-Cell Interactions

4.5.3.1. Cell Viability by MTS Assay

In the first step of the study, all synthesized NPs were coated on the scaffold surface at a ratio of 1:1, and cell viability analysis was performed (Figure 4.43A). As a result of this study, the negative effect of NPs on cell viability was clearly seen, and the study was carried out again with various dilutions (Figure 4.43B). Since it was seen that the NPs had a low threshold of toxic effect on the scaffolds coated with 1:10 and 1:20 dilution ratios, the study was repeated using these ratios (Figure 4.43C). At this stage, another goal was to determine which cell cultivation method—wet or dry seeding of cells—would be most appropriate. Since there was no clear advantage to wet seeding, it was decided to continue with dry seeding after this stage.

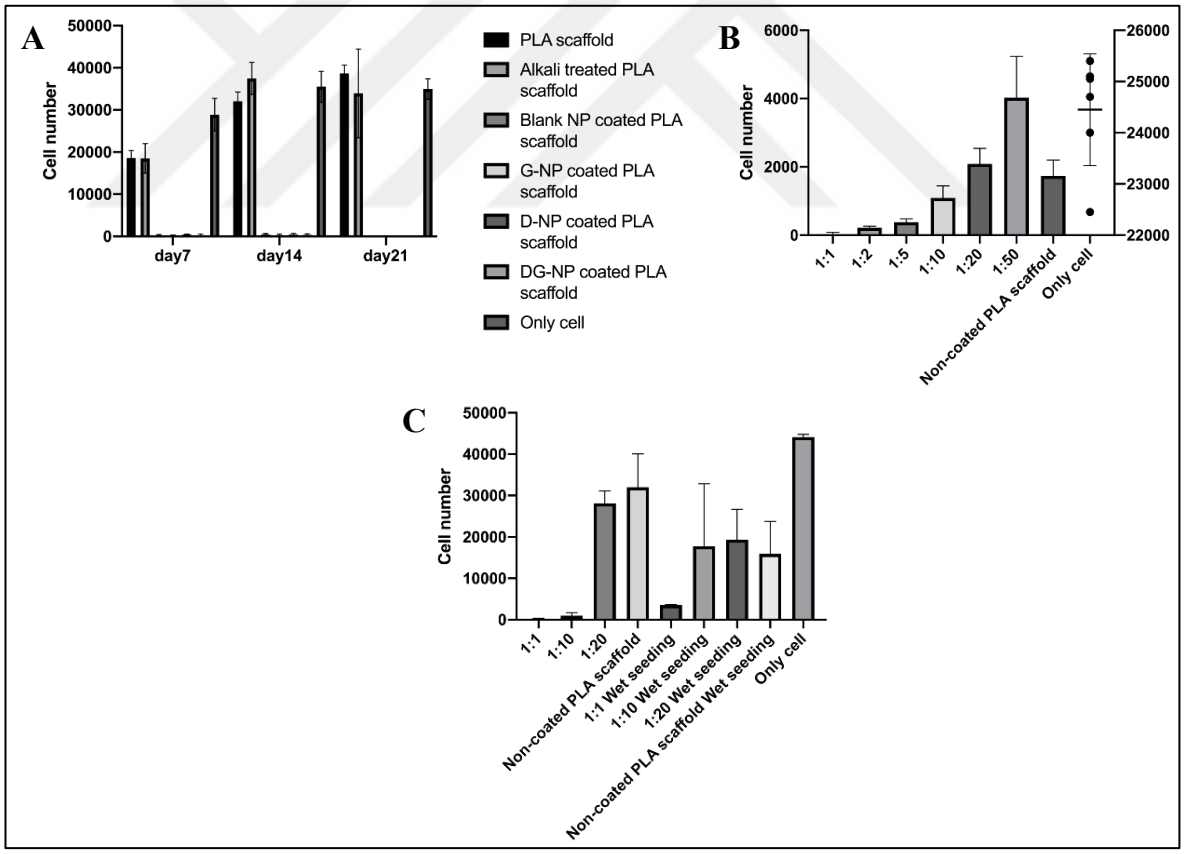


Figure 4.43 Cell viability by MTS assay of untreated and treated scaffolds coated with nanoparticles in (A) a 1:1 ratio, (B) different ratios, and (C) different ratios and seeding methods. Initial cell seeding density was 5 x 10^4 cells/scaffold.

After optimizations, the scaffolds were covered with NPs with a 1:20 dilution ratio by dry seeding, and the MTS assay was carried out at the end of 7, 14, and 21 days in culture (Figure 4.44). At all time points, cell viability was low in both uncoated and untreated scaffolds. After 7 days, the scaffold coated with D-NP had a significant difference over the untreated scaffolds. This difference continued at the end of 14 days and disappeared at the end of 21 days. After 21 days, a significant difference was observed in the cell viability of the G-NP coated scaffold versus the groups without DIPQUO.

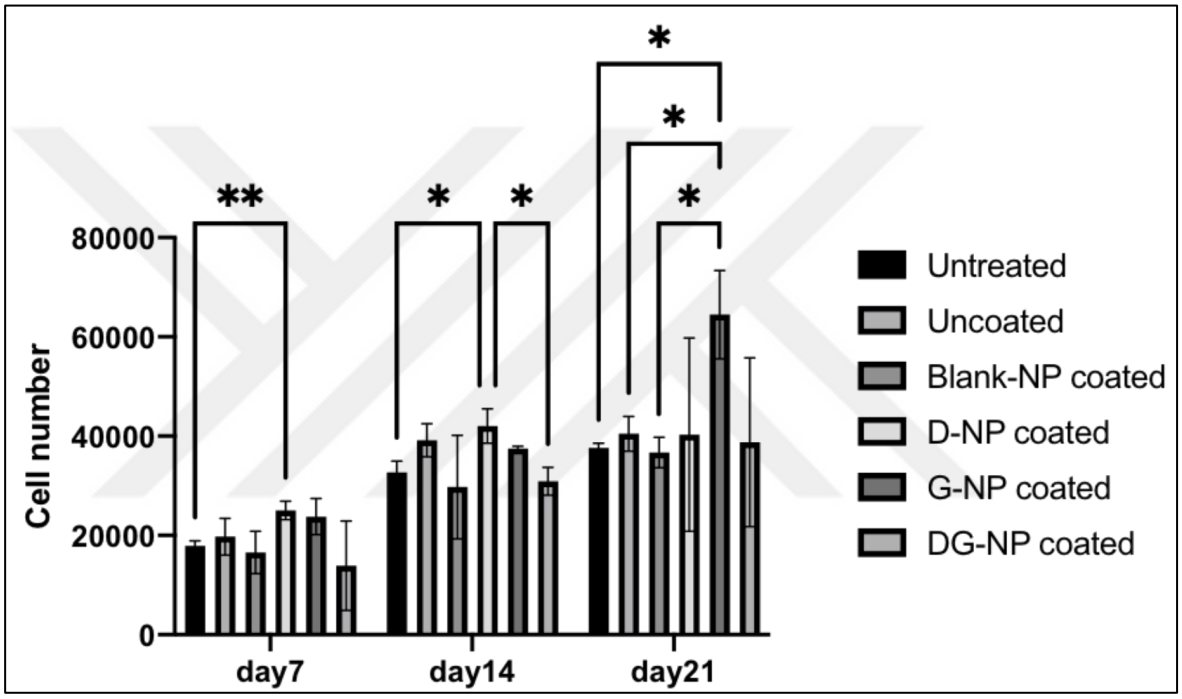


Figure 4.44 Cell viability by MTS assay of uncoated, untreated, and treated scaffolds coated with nanoparticles in a 1:20 ratio. Initial rBMSC seeding density was 5 x 104 in DMEM growth medium.

4.5.3.2. Live-Dead Assay

Cell viability was visually demonstrated by performing the Live-Dead test on NP coated scaffods. It was observed that rBMSCs extended along the PLA surface and interconnected between the pores (Figure 4.45). The increase in cell density was evident in all groups as the days passed in culture. Cell viability was significantly higher in the G-NP group, especially at the end of day 21, compared to the other groups.

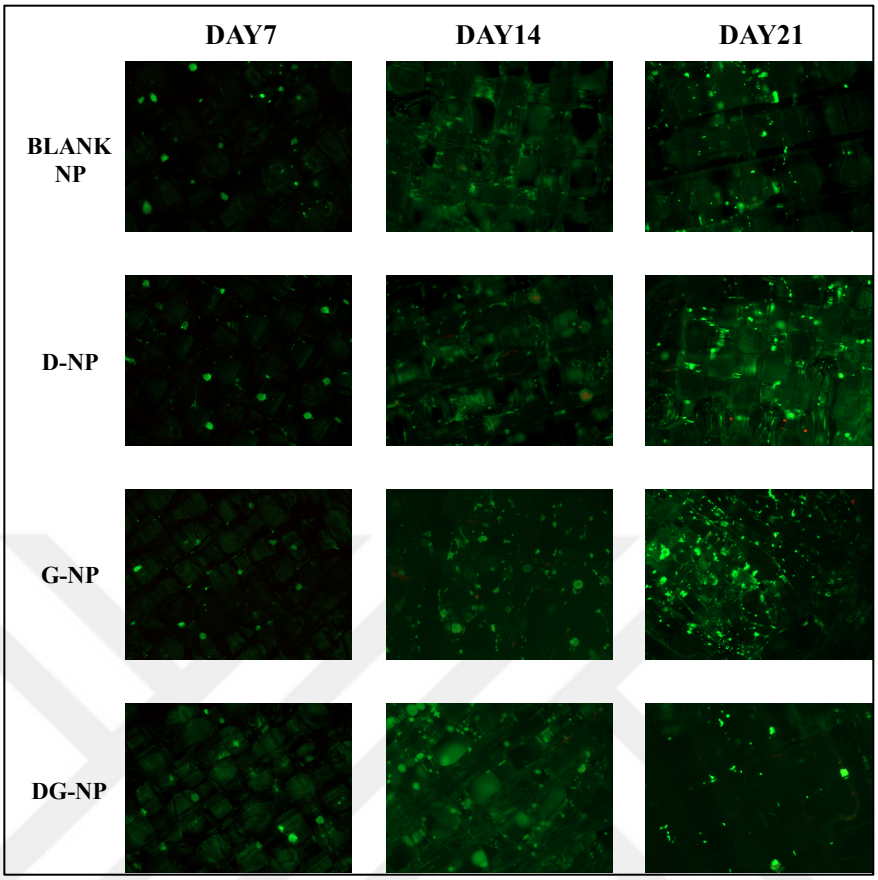


Figure 4.45 rBMSC viability by Live-Dead assay in 3D-printed NP coated PLA scaffolds throughout 7, 14, and 21 days of incubation (dead cells: red; live cells: green), scale:200 µm.

4.5.3.3. Cell Proliferation by PicoGreen Assay

A PicoGreen assay was performed to detect the amounts of DNA in NP coated scaffolds and to compare the effect of NPs on cell proliferation (Figure 4.46). As the day in culture progressed, it was observed that the amount of DNA increased in correlation in all groups. On day 7, G-NP coated piers had more cells and DNA with a significant difference from the DG-NP coated group. At the end of day 14, the amount of DNA in D-NP coated scaffolds showed a significant difference compared to blank NP coated ones. At the end of the 21-day experiment, the DNA amounts increased and the difference became insignificant.

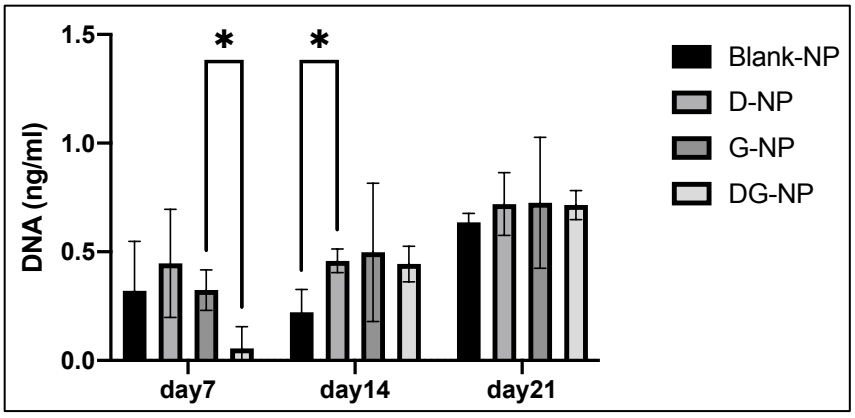


Figure 4.46 Cell proliferation by PicoGreen assay of rBMSC seeded NP coated scaffolds. $p < 0.05$. Initial cell seeding density was 5 x 10^4 cells/scaffold.

4.5.3.4. Alkaline Phosphatase Activity

The results of the study examining ALP activity are shown in Figure 4.47. It can be said that ALP activity started to decrease after day 7 for all groups. This decrease was not seen only in the blank NP coated scaffold. In the analysis performed at the end of day 7, it was observed that the ALP activities of the blank NP coated and DG-NP coated scaffolds were higher than those of the other groups, and the difference was significant and continued for 21 days of culture.

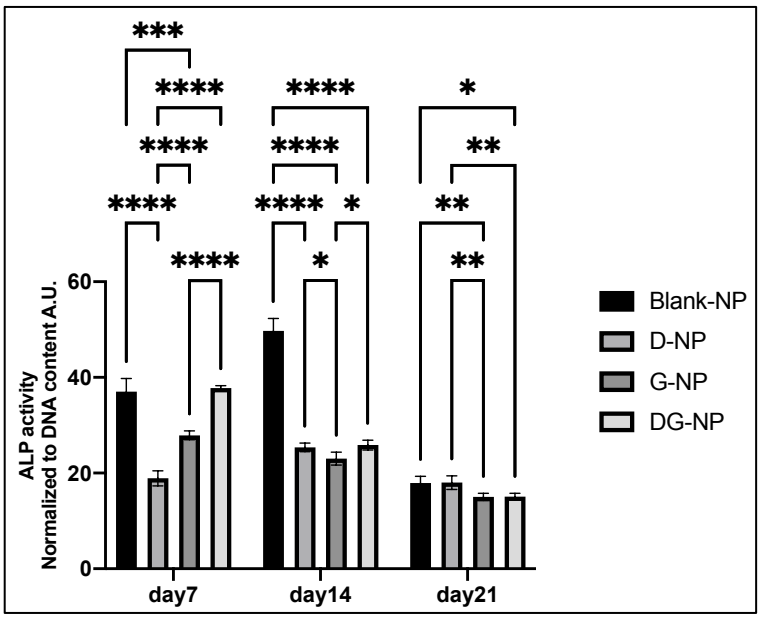


Figure 4.47 ALP analysis on rBMSC seeded NP coated scaffolds after 7, 14, and 21 days of culturing. The data were normalized against DNA content; n=3, $p < 0.05$.

4.5.3.5. Calcium Assay

The amount of calcium produced by the differentiated cells was determined by a calcium assay (Figure 4.48). In this study, it was observed that the amount of calcium produced by the cells increased. After day 7, this difference was significant on D-NP coated scaffolds. At the end of 21 days, no significant difference was observed between the groups.

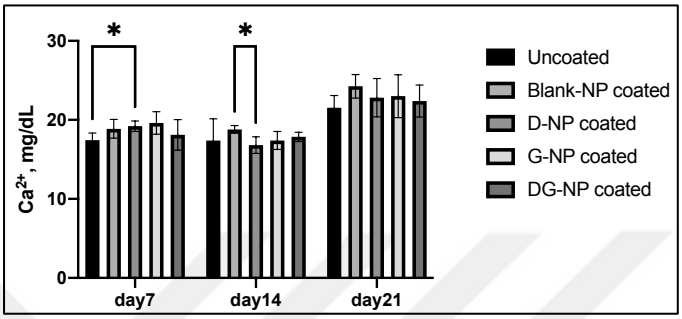


Figure 4.48 Calcium assay of rBMSC seeded NP coated scaffolds after 7,14, and 21 days of culturing; $p < 0.05$.

4.5.3.6. Osteocalcin

The osteocalcin assay was used to determine the OCN proteins secreted by rBMSCs into the medium. In this analysis, two different types of OCN were analyzed. It was observed that Gla-OCN, which is, effective in bone remodeling, increased in all groups during the 21-day study (Figure 4.49A). It was determined that the amount of OCN in the medium was high at each time point, especially in groups containing DIPQUO. Glu-OCN, on the other hand, which is effective in energy metabolism, did not increase in all groups (Figure 4.49B). In this study, it was observed that the OCN produced by rBMSCs in scaffolds containing dual small molecule-loaded NPs (DG-NP) was quite high.

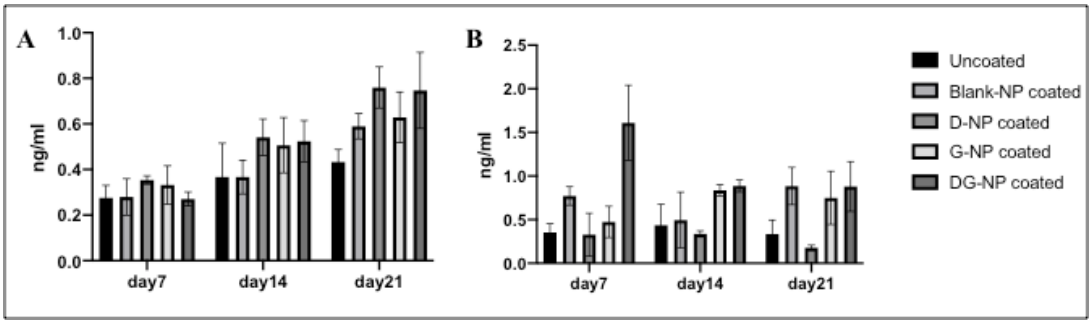


Figure 4.49 Osteocalcin assay on rBMSC seeded NP coated scaffolds after 7,14, and 21 days of culturing: (A) Gla-OCN, and (B) Glu-OCN.

4.5.3.7. Alizarin Red Staining

Alizarin red staining was applied to NP coated scaffolds after 7, 14, and 21 days of incubation (Figure 4.50). Calcium deposits were visualized in red with this staining. It was observed that the accumulations increased as the day progressed. At the end of 21 days, accumulations were low in uncoated scaffolds, whereas red deposits were high in all groups containing DIPQUO (D-NP and DG-NP coated scaffolds).

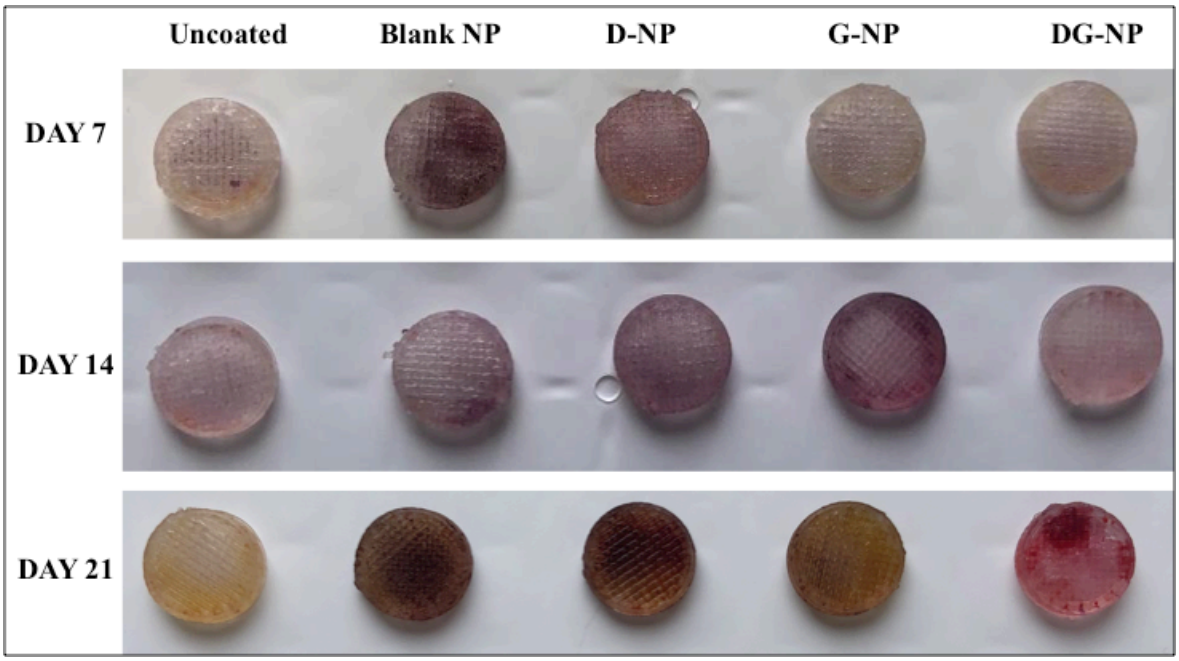


Figure 4.50 Alizarin red staining of rBMSC seeded NP coated scaffolds in osteogenic medium (OM) after 7, 14, and 21 days in culture.

4.5.3.8. von Kossa Staining

von Kossa staining was applied to NP coated scaffolds after 7, 14, and 21 days of incubation (Figure 4.51). With this staining, calcium deposits on the scaffold surface were stained brown. It was observed that the accumulations increased significantly as the day progressed. At the end of day 14, calcium accumulations were higher in NP containing groups, while calcium accumulations with osteogenic differentiation were observed in all groups at the end of day 21.

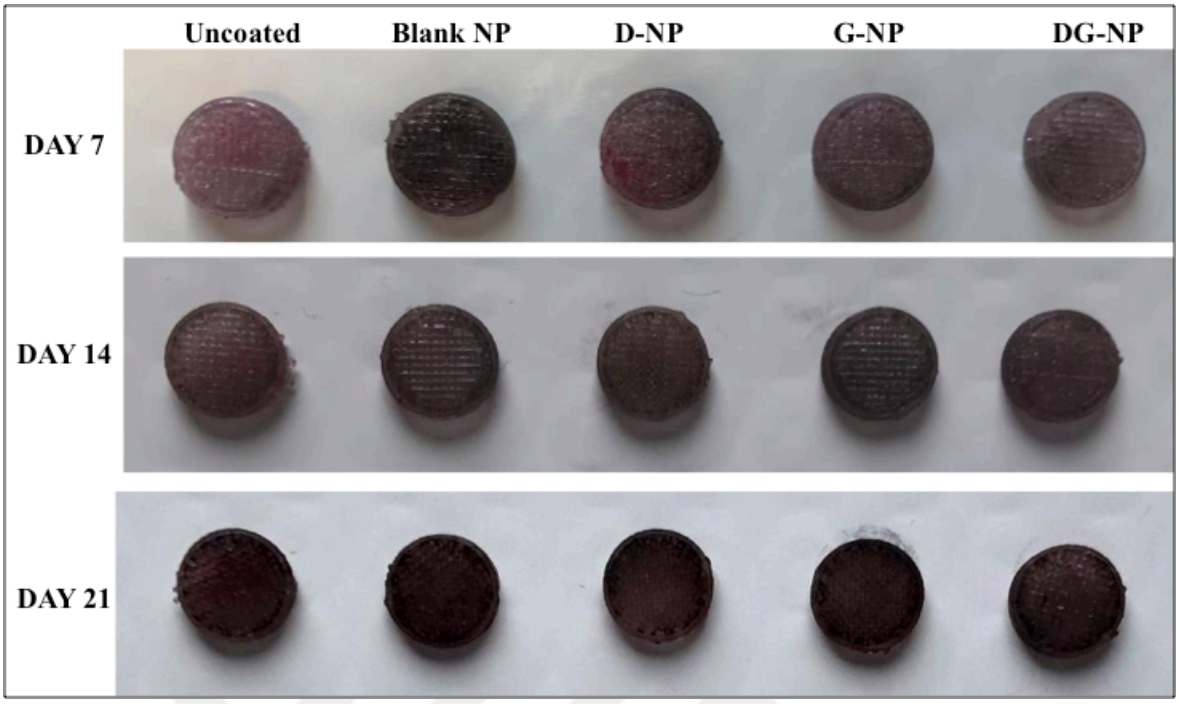


Figure 4.51 von Kossa staining of rBMSC seeded NP coated scaffolds in osteogenic medium (OM) after 7, 14, and 21 days in culture.

4.5.3.9. Realtime-PCR

In this analysis, RNAs produced by rBMSCs with bone differentiation were examined. RNA was isolated from scaffolds and transcribed into cDNA. Real-time PCR was performed using optimized primers. Within the scope of the study, the expression levels of the bone markers ONC, Runx2, and Col1a1 were examined (Figure 4.52).

At the end of the study, it was observed that the expression of ONC, a late bone marker, increased as time passed. At the end of days 7 and 14, it was observed that the fold change in blank NP coated scaffolds was higher than in the control and other groups, and this difference disappeared after day 21. At the end of day 21, it was observed that groups containing dual small molecules (DG-NP) and only DIPQUO (D-NP) exhibited a significant fold change. In D-NP coated scaffolds, the fold change was 42.76, while in DG-NP coated scaffolds it was 54.19. Similarly, the fold change in the blank and G-NP coated scaffolds was eight times greater than the control at the end of day 21.

When the Runx2 marker was examined, it was observed that the expression level increased as the day in culture progressed. After 21 days, the fold change was 7.41 in the G-NP coated scaffold group.

The bone marker Col1a1 was examined. At the end of day 7, fold change was higher in the two groups containing DIPQUO (D-NP and DG-NP) compared to the other groups. In D-NP coated scaffolds, the fold change was 1.23 compared to the control, while in DG-NP coated scaffolds it was 1.82. At the end of day 14, the D-NP coated scaffold fold change reached the highest value of 1.96 and created a significant difference from other groups. The DG-NP coated scaffold had the highest fold change at the end of day 21.

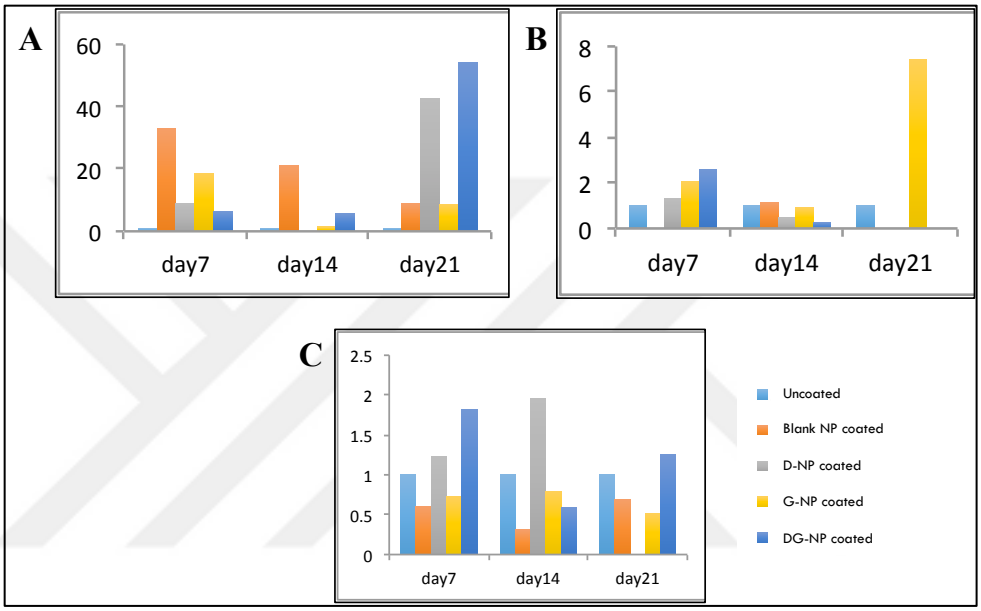


Figure 4.52 Expression levels of A) ONC, B) Runx2, and C) Collagen type I (Col1a1).

4.5.3.10. In Vitro Angiogenesis

The vessel-forming capacity of isolated rPBECs was investigated by an *in vitro* angiogenesis assay in a 3-dimensional structure (Figure 4.53). At the end of this study, it was observed that GS4012 showed similar results as the positive control and VEGF and directed the endothelial cells towards the tubular structure. This change was observed even at the end of the first 48 h. At the end of the 120th h, new tubular structures formed with the proliferation of cells, as proven by BF images. In comparison to other groups, GS4012 encapsulated in NP was particularly effective in *in vitro* tube formation.

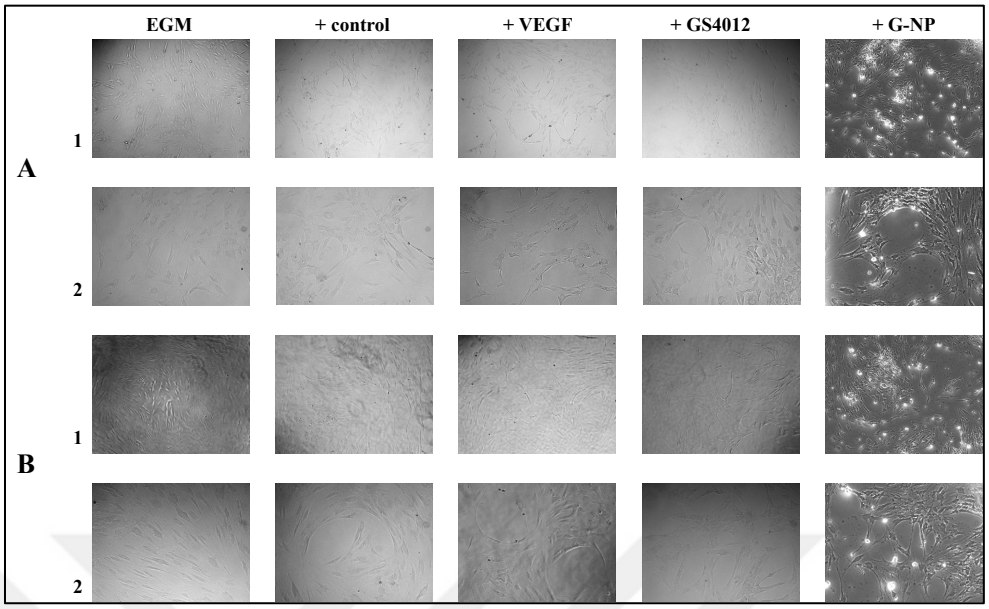


Figure 4.53 BF images obtained as a result of an *in vitro* angiogenesis assay after (A) 48 h, and, (B) 120 h with magnification of (1) 10X, and (2) 20X. EGM:endothelial growth medium.

4.5.3.11. Migration Assay

The purpose of this assay was to determine how GS4012 affected rPBEC migration. The cells passing through the tissue culture plate and inside the insert were studied under bright-field microscopy after the cells seeded on the insert were fixed and stained with crystal violet. Figure 4.54A shows that cell migration was very low in the EGM group, and therefore, cell density was observed in the inserts as a purple color. In media containing VEGF and GS4012, cell density decreased in the insert due to migration, whereas in media containing G-NP, only a very small amount of endothelial cells remained in the insert due to the migration of most of the endothelial cells. Figure 4.54B shows the insert images taken with a light microscope. It can be said that migration was significantly higher in groups containing GS4012. In particular, G-NP accelerated endothelial migration. In Figure 4.54C, it can be seen that the migrating endothelial cells adhered to the tissue culture plate and started to proliferate on the surface.

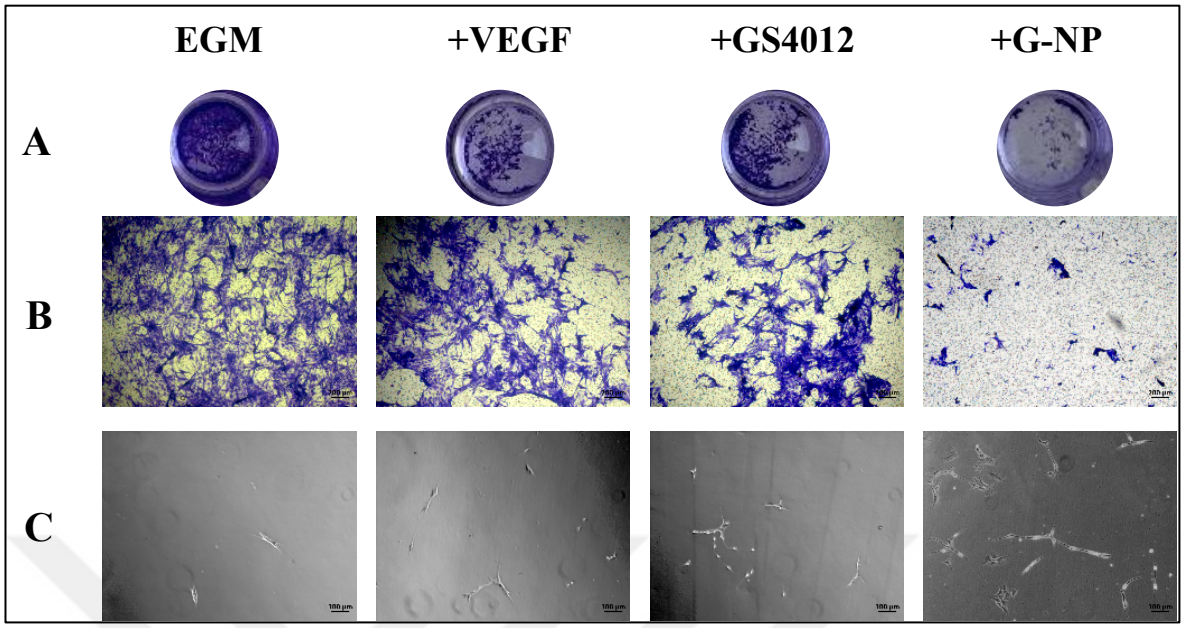


Figure 4.54 Migration assay study of rPBECs in the insert with crystal violet. (A) Digital images, (B) BF images in the insert, and (C) BF images of rPBECs migrating to a tissue culture plate after migration assay. EGM:endothelial growth medium.

4.5.3.12. Immunofluorescence Staining of Coated Scaffolds

In this analysis, the migration of rPBECs from the inserts to the surface of rBMSC seeded NP coated scaffolds during the 14 day incubation period was investigated. In this study, the effect of GS4012 was clearly observed with images taken with fluorescence microscopy (Figure 4.55). Even at the end of day 3, it was observed that the endothelial cells migrated and adhered to the G-NP coated scaffold, and this number increased as the day in the culture progressed. After day 14, high endothelial cell density was clearly observed in the G-NP coated scaffold. It was seen that blank NP coated scaffolds also induced endothelial cell migration due to their chitosan NP content, whereas migration was negligible in uncoated scaffolds.

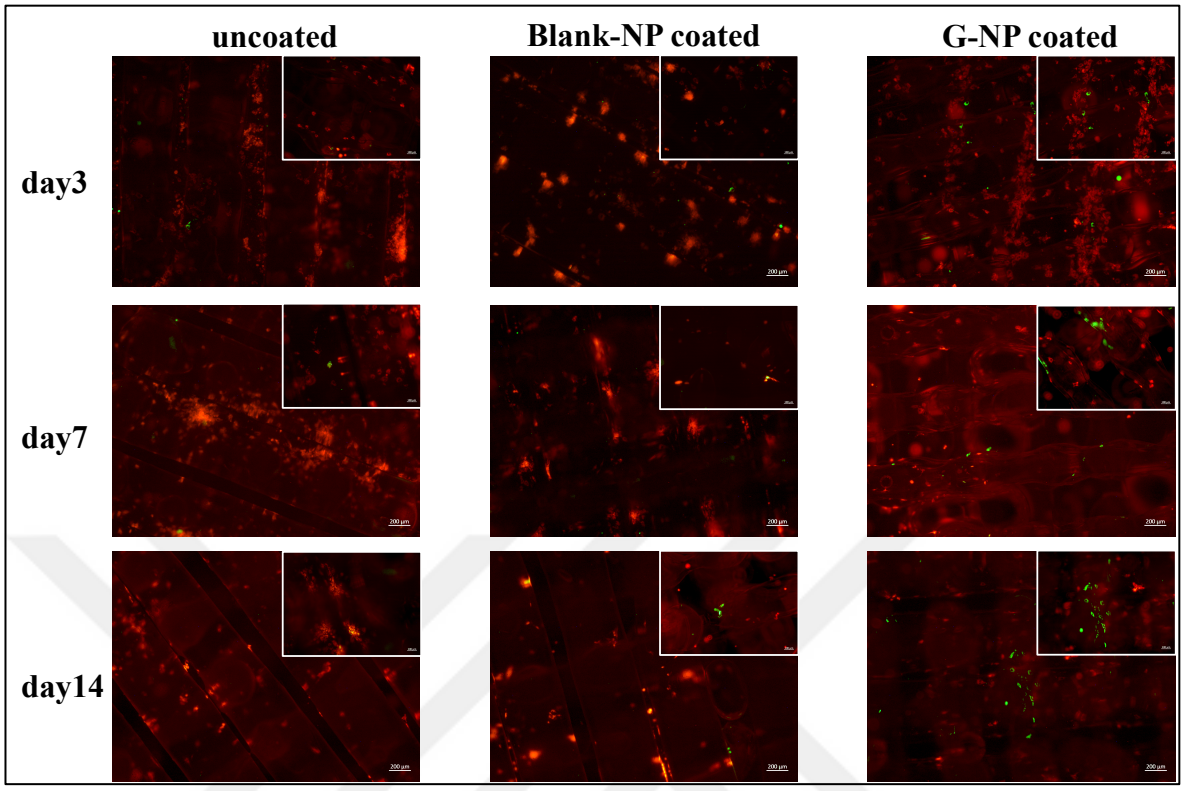


Figure 4.55 Immunofluorescence staining of NP coated scaffolds in co-culture after 7, 14, and 21 days of incubation. Scale: 200 µm, Indent scale: 100 µm.

5. DISCUSSION

The important point in BTE, which aims to create a living, functional 3D bone in the laboratory environment, is to be able to mimic the structure and provide regeneration of natural bone and obtain sufficient mineralized tissue on the 3D carrier. It is possible to achieve success in BTE studies with the right combination of scaffold design, cell selection, and GFs. In this study, scaffold production was carried out by a 3D printer using PLA polymer, which is a frequently used polymer in the literature. CS NPs loaded with DIPQUO, an osteogenic differentiation factor, and GS4012, which is an angiogenic factor, were synthesized, and surface-modified PLA scaffolds were coated with these NPs. The goal of this system was to accelerate tissue healing by promoting vascularization in conjunction with bone healing.

Our first goal in the study was to find a scaffold with a suitable pore size for BTE. In this context, firstly, the pore diameters and porosities of the tissue scaffolds were determined by the structural and morphological analyses. In accordance with the literature and considering the most preferred pore sizes, scaffolds with 100–560 micrometer pore sizes were printed. As can be seen from the digital images of the 3D-printed scaffolds, high-resolution and reproducible scaffolds were printed. Besides, it was noticed that the visibility of the pores decreased as the filling rate increased. Bright-field microscope images of the scaffolds supported the digital images. With SEM analysis, it can be seen that the pore diameters of scaffolds decreased as the filling percentage increased as expected. The results obtained with SEM from the top and cross-section views of the scaffolds were different. The reason for this is that the pore sizes of the cross-sections were smaller due to thick fibers between the layers [112]. Furthermore, the pores on the inner surface of scaffolds were smaller. When the actual fiber thicknesses were compared to the computer-designed fiber thicknesses, it was discovered that the two fiber thicknesses were very close in value. It was observed that there were differences between the theoretical design of filling rates and the filling rates obtained with SEM and BF images. This situation might be due to the expansion and cooling of the polymer after the scaffold was printed with its theoretical design [113,114]. It can be seen that the actual filling rates were higher for all scaffold types than the designed ones.

Chemical characterization of the PLA scaffold was carried out with FT-IR analysis. All peaks and stretching that were found with FT-IR in the PLA spectrum were found compatible with the literature [115].

In the DSC analysis for chemical characterization, it can be said that there were two endothermic and one exothermic peak in the graph. The first peak represented the endothermic peak that belongs to the glass transition temperature of the material. The second peak was the exothermic peak, which occurred through a phenomenon called cold crystallization. The third endothermic peak indicated the melting temperature of the material [114]. PLA has a glass transition temperature between 50 and 80, and our results are in accordance with the literature [116]. Although it can be clearly seen that the printing process decreased the material's glass transition temperature, this can be connected to the structure change and degradation with the temperature of the PLA. The lower crystallization temperature that appeared after the printing process is associated with solid-state transitions between crystalline states [114]. It was reported that this situation, which was observed in the distribution of the crystalline phases formed and in materials above the glass transition temperature, might result in changes in the phase change capacity.

PLA is a relatively hydrophobic material, which can often cause problems with cell adhesion. In this study, it was observed that the scaffolds had an average contact angle value of 85 degrees, and this value was cohesive with the standard PLA material [117]. From this, it was concluded that PLA scaffolds were almost at the limit of hydrophilicity. The filling differences between the groups did not cause a significant difference in this value.

After obtaining the scaffolds with the desired pore size, they were characterized with respect to mechanical strength, which is of great importance in BTE. The modulus of cortical bone is in the range of 15–25 GPa, while that of cancellous bone is in the range of 0.1–2 GPa [118]. While the compressive modulus values obtained in this study were lower than the cortical bone, it was seen that they were similar to the natural structure of the cancellous bone. As the pore size increased, the mechanical strength increased too. It was observed that the scaffolds' Young's modulus values increased with the filling rate. The desired Young's modulus value in compact bone is in the range of 17 to 20 GPa, and the compression modulus value of the scaffold with a 90% filling rate was close (~10 GPa) to that of compact bone. While the compression modulus values of all other scaffold types

obtained in this study were lower than 10 GPa, these values were also reported as suitable for BTE [118–120]. In our study, it was observed that compressive strength values in yield and break could not be associated with the filling rate, but these values were associated with the PLA material itself. The Young's modulus values of the tensile stress and the ultimate tensile strength value also increased positively with the filling rates. The results obtained in this study showed that PLA is a favorable polymer with suitable properties for BTE. It is known that mechanical properties not only give structural strength but also affect the growth and differentiation of stem cells [121].

In BTE applications, the scaffolds must be completely degraded to products that are non-toxic to cells, and at the same time, this degradation rate must be at a certain rate to allow the scaffolds to maintain their mechanical structure favorable for cell growth. As a result of PLA degradation, carbon dioxide and water are released, which do not cause toxic effects on cells [51]. In our study, it was seen that there was no weight loss in the degradation study of PLA scaffolds (both BASF and Corbion) carried out in standard degradation solution for 120 days, and this was due to the high crystallinity of the material. The swelling of the material is very important, as it is proportional to its water retention capacity. It was observed that the swelling ratio could be up to 20% in different pore size scaffold types and up to 10% in Corbion PLA scaffolds. Although this ratio showed that the water holding capacity was not very high, it was seen that it was in harmony with the literature [122]. In the enzymatic degradation, 30% of the different filling rates of scaffolds were degraded after 10 days of incubation, and the pH of the environment decreased to around 4 with the lactic acid release. When enzymatic degradation was applied to three different scaffold types—untreated, uncoated, and NP coated scaffolds—it was observed that the degradation was faster and higher in the uncoated group than in the other groups. Both uncoated and NP coated scaffolds had undergone alkali treatmet, and due to the alkali treatment, the degradation rate was also high due to the material's surface abrasiveness and the OH groups on the surface. This increase in the degradation rate might be due to the wider scaffold surface [123]. Xu et al. [124] showed that, as a result of PLA alkali treatment, the surface chemistry of the material changed, increasing its hydrophilic properties by reducing the contact angle and supporting the binding of hydrophilic enzymes. However, this degradation rate was also slowed down by the NP coating on the abraded scaffold surface. Similar to the other experimental group, the pH change decreased

to 4, with a sudden decrease due to the lactic acid released into the environment, and remained at this value.

In the second part of the study, NP synthesis and optimization were carried out to be the carriers of small molecules. For this purpose, chitosan was used as the main material, and the ionic gelation method was chosen. Firstly, optimum conditions were achieved by using blank NP, and then small molecules were loaded into NPs and characterized by various methods. Particle size and zeta potential measurements were performed on a zetasizer. Dimensional analysis was performed and recorded. NP synthesis was done by ionic gelation method using a pipettor on a magnetic stirrer, a burette on a magnetic stirrer, and a sonicator device. It was observed that the NPs obtained with the magnetic stirrer were better than the ones obtained by sonicator, since the sonicator alone was not sufficient. Using burette for synthesis showed similar results. It was decided to perform the synthesis with an automatic pipette since it was simpler and faster to apply. For loading of DIPQUO, it was decided that Tween 20 would be the most ideal intermediate phase. The mass ratio was chosen as 3.33.

In this part of the study, NPs of different sizes were synthesized in the preliminary studies. When the PDI value is above 0.7, it means that the sample has a large particle size and can not be analyzed in DLS [125]. In drug or molecule loaded NP studies, the PDI value is required to be below 0.3, and this value indicates a homogeneous distribution. Considering this information, NPs with a PDI values below 0.3 were selected. When the size distribution graphs of the blank and loaded NPs were examined, it was seen that the peak in the graphs exhibited a clean and uniform distribution for all samples.

Zeta potential values were found in the range of 11–18 mV in blank and loaded NPs. There was no significant difference between the zeta potentials of blank and loaded NPs (Table 4.3). The solution is considered stable when the zeta potential value is less than -30 mV or greater than +30 mV [126]. Since the zeta potential values obtained as a result of the study were in this range (-30 to +30 mV), it was seen that the NP solution was not stable and tended to aggregate. Although this may seem like a negative situation, the values obtained in this study were desired due to the increase in toxicity with the increase in negative or positive surface charge in cell studies [127]. At the same time, since the NPs were not used directly but in the scaffold coating, they did not remain in suspension, and aggregate formation was prevented by being immobilized on the surface of the scaffolds. When the

zeta potential distribution graphs of the blank and loaded NPs were examined, a single peak for all samples was observed in the graphs.

The particle morphology characteristics of the NPs were investigated using TEM. The results showed that NPs were spherical in shape and had a smooth surface. The dimensions of the NPs distributed along the surface were quite equal to each other; NPs had an average size distribution of 150 nm. The particle size results obtained using DLS and TEM images showed consistency.

Surface chemistry characterization of NPs was performed by FT-IR analysis. The peaks originating from -NH and -OH stretching in the blank NPs were found to expand to 3,381, 3,256, and 3,147 cm^{-1} peaks, respectively, in loaded NPs. This situation was thought to be due to the expansion of H bonds [128]. The peaks obtained from chitosan, TPP, and Tween 20 were coherent with the literature. While the peak caused by C=O stretching in chitosan was preserved after NP synthesis, it was observed that the peak caused by -NH stretching at 1,538 cm^{-1} in chitosan shifted to 1,535 cm^{-1} after NP synthesis. This was thought to be due to the cross-linking of -NH bonds with TPP. A new peak originating from the P=O bond was formed in the NP samples at 1,193 cm^{-1} [111]. This was due to the formation of bonds between the amino groups present in the CS and the phosphate groups present in the TPP [129]. The characteristic peaks of small molecules disappeared after NP production. This situation proved that the small molecules were effectively encapsulated [130].

The phase transition curves of CS, TPP, Tween 20, blank and loaded NPs were characterized by DSC. In the CS thermogram an endothermic peak at 115° occurred due to the loss of water [131]. In addition, the thermogram of TPP showed two endothermic peaks corresponding to the melting point of the crystalline region. Tween 20 thermogram revealed one endothermic peak at 90°, which was similar to the literature [132]. When compared to its source polymer molecule, NP's melting temperature was increased [100].

While the efficiency of the blank NP synthesis was low, the reaction yield of the loaded NPs was increased. The reaction efficiency was highest in D-NP synthesis. Because the bond provided by Tween 20, which was a mediator carrier, was strong and facilitated the synthesis, thereby increasing the reaction yield [133].

Encapsulation efficiency (EE) appeared to be higher for single small molecule loaded NPs and slightly lower for dual small molecule loaded NPs. This was thought to be due to a lack of space in the NPs with two different molecules loaded. Although a decrease in EE was observed, the EE results obtained in this study were within the acceptable range.

The loading capacity (LC) of NPs can be considered relatively low [134–136]. It was observed that while the LC of D-NP increased in dual NP, that of G-NP decreased.

Release tests on loaded NPs were performed in triplicate. Three different NPs loaded with small molecules (D-NP, G-NP, and DG-NP) were chosen to study release. The study was continued for seventeen days. The NPs that contained small molecules appeared to released all of the content they had at the end of the release study. The NPs required 13 days to release all of the small molecules. Within the first 3 h, 71% of the DIPQUO was released in D-NP, 38% of the GS4012 was released in G-NP, and similar results were obtained with DG-NP. Following that, the rate of degradation was reduced. After day 13, the degradation study continued and was shown to be stable. As seen in the results of the study, DIPQUO release was almost two times faster than GS4012. This was because D-NP contains Tween 20, a detergent agent, thus increasing the degradation rate of NPs in PBS [137]. As expected, the results obtained with G-NP were similar to the release result obtained with the BSA molecule as a preliminary test at the beginning of the study.

The IC50 value of the DIPQUO obtained as a result of the study was close to the IC50 value specified by the company. This small difference might be due to sensitive nature of the stem cells used in this study.

Since PLA is an inert material, it is not possible to integrate NPs onto the scaffold surface without interference. According to Furuike et al. [138], coating CS on the PLA surface requires the partial hydrolysis of ester bonds by alkali treatment. For this purpose, alkali treatment applications were carried out on scaffolds to add chemical groups to the surface. In our study that was carried out with different concentrations and durations, the condition of a low concentration for a long time was selected. The molarity of 0.5 was preferred, as the scaffold surface wore down during the high concentration treatment and its mechanical properties decreased. The ester hydrolysis on the PLA surface was significantly influenced by the amount of alkali treatment [138]. In the treatment performed at this concentration, 2 h were insufficient, so the time was extended, and the treatment was carried out for 4 h

[139]. As a result of this process, OH groups were attached to PLA scaffolds. Following alkali treatment, NPs were either mixed directly with scaffolds or added to the surface to immobilize NPs on the surface before drying in a vacuum desiccator. Directly adding NPs on scaffolds was chosen since the desired concentration of NP could not be achieved with only mixing by magnetic stirrer. After adding NPs directly on scaffolds extra drying was required for immobilization NPs on the surface. As a result, all surfaces of the scaffolds were completely covered with NPs, as desired. This situation was proven by SEM images.

MSCs have the capacity to differentiate into three different cell types (osteoblast, chondrocyte, and adipocyte) [140]. rBMSCs isolated within the scope of the study were differentiated into these three cell types, and their mesenchymal origin was proven with stainings [141,142]. The osteogenic differentiation capacity of rBMSCs was evaluated by using von Kossa and alizarin red stainings, and high mineralization of the cells was observed [142–144]. Calcium deposition in the cells indicated excessive mineralization. The chondrogenic differentiation capacity of the rBMSCs was identified with alcian blue staining [145]. This assay provides visualization of the deposition of the mucopolysaccharides. The cells that were cultivated in the chondrogenic medium were stained with a maximum density. Oil red O staining was utilized to confirm the adipogenic differentiation of the rBMSCs that exhibited oily vesicles and lipid droplets, which are similar to the adipocyte cells [140]. Cells isolated from bone marrow were characterized by flow cytometry analysis, showing positive for MSC markers CD29 and CD90, while negative for HSC markers, CD45 and CD34. Similar results were obtained in other studies of rBMSC characterization [142,146].

Endothelial cells isolated from rat peripheral blood were also characterized in that they exhibited endothelial properties. For this purpose, firstly, BF images were taken and endothelial cell similarity was visually confirmed. The isolated cells were stained with PECAM-1, an endothelial surface marker [147], and it was proven that there was no different type of cell in the medium. Since it is known that endothelial cells uptake Ac-LDL protein, the cells were characterized by examining their Dil-Ac-LDL uptake capacity [148].

Both isolated cell types (rBMSC and rPBEC) were successfully stained with fluorescent dyes, and visual tracking in cell culture became possible. In order to distinguish between cell types, rBMSCs were stained red, while rPBECs were stained green.

In the last part of the study, *in vitro* material-cell interactions were investigated. This section was divided into three different groups: cell interactions with PLA scaffolds, cell interactions with NPs, and cell interactions with NP coated PLA scaffolds.

The first group involved cell interactions with PLA scaffolds. Cell viability assay was done on these scaffolds. In the rBMSC proliferation study, as the filling rate increased, a decrease in the number of cells was observed. Immunofluorescence staining showed that rBMSCs displayed their characteristic morphology, attached along the PLA fibers, and provided a connection with each other between the pores. The quantitative cell number differences between the scaffolds obtained as a result of MTS and the qualitative differences obtained as a result of the Live-Dead staining images after 7, 14, and 21 days of incubation were relevant. As a result of MTS, it was seen that cell viability increased as time passed. Also in Live-Dead staining, it was observed that the morphology of the rBMSC cells and their attachment to the scaffold surfaces were quite clear, the viable cells on the scaffold surface were highly concentrated toward day 21, and the cells completely covered the surface of five different types of scaffolds.

As a result of the differentiation study using OM, it was seen that the most efficient result was obtained in the scaffold, with a 60% filling rate on day 7. There is an inverse relationship between cell proliferation and the differentiation process. While progenitor cells continue to divide and proliferate before differentiation, this proliferation stops in cells when differentiation is complete and a permanent exit from the division cycle has occurred [149]. For this reason, in scaffolds with OM, cell viability did not increase as the day progressed, as in GM. It was also observed that the proliferation of osteoblast cells was not associated with pore sizes in the long term. When rBMSC differentiation on scaffolds was investigated, it was found that there was a significant difference in ALP activity at the end of day 3 in the scaffolds with a 60% filling rate, compared to the other groups. The reason for this difference is that ALP is an early bone marker, and its prominence decreases over time [150]. In the von Kossa staining, while no bone differentiation was observed in the scaffolds with GM, rBMSCs cultivated in OM provided mineralization.

Cell viability was also investigated in chitosan-NP cell interactions, which was our second group in the study. It was observed that the G-NP group was significantly different from the other groups after day 7. It might be due to the positive effect of GS4012 on cell viability. NPs containing DIPQUO, on the other hand, had a negative effect on cell

viability. It was thought that this situation was due to the toxic effect of DMSO used for the solubilization of DIPQUO on cells [84]. Having two small molecule types in the DG-NP group, neither high viability as G-NP nor low viability as D-NP was observed. The two small molecules balanced each other and affected cell viability together.

ALP is accepted as an early marker in bone formation [34]. For this reason, as expected in the study conducted in culture, the amount of ALP was higher at the end of day 7, while the amount decreased as the study progressed in culture. Since DIPQUO is an osteogenic differentiation factor [84], osteogenic differentiation was accelerated in cells treated with D-NP at day 7, resulting in increased ALP synthesis. Although GS4012 is not an osteogenic factor, it is effective in bone formation since it is a VEGF inducer, and VEGF affects the transformation mechanism of stem cells [91,92]. This was evidenced by the higher ALP activity of GS4012-containing NP groups compared to blank NPs. By day 14, ALP activity in NPs containing DIPQUO was higher than in other groups due to the osteogenic differentiation. The difference was found to be significant in DG-NP treated cells. Since ALP is an early marker, there was no significant difference between the groups at the end of day 21.

The stainings supported the effect of GS4012 on cell proliferation as indicated by MTS. The stem cell's ECM was stained with H&E stain. The positive or negative effect was investigated by staining cells in NP treated groups. Compared to the blank NPs, it was observed that the G-NP treated cells were more accelerated even in the first days and this difference was more clear on the last day of the culture. Similar to the results of MTS, cell density was lower depending on DMSO in groups containing DIPQUO, but the difference was not significant. Alizarin red and von Kossa stainings were also performed to investigate the bone differentiation of rBMSC cells with NP treatments. It was observed that NPs that contained DIPQUO had a significant difference in bone differentiation compared to the other groups, especially at the end of day 21, and that the entire tissue culture plate surface was stained a dark red color. Calcium accumulation was quite high as a result of osteoblast differentiation in D-NP treated cells; following that, it was seen that the most accumulation was found in DG-NP, followed by G-NP treated cells. When DIPQUO and GS4012 were administered simultaneously (DG-NP treated), it was observed that DIPQUO could not show the differentiation activity that it did alone. It could be due to synergestic effect of small molecule on cells, leading not only to differentiation but also to

proliferation due to GS4012 present in the medium. Similar results were observed in von Kossa staining.

In the last part of the study, cell interactions with NP coated PLA scaffolds were investigated. First, a cell viability study was performed. After synthesis, it was observed that the small size of the NPs in direct coatings and the positive surface charge caused cell death by having a toxic effect on them. For this reason, during the study, the NPs were diluted 1:20 after synthesis, and the surfaces of the PLA scaffolds were coated. Chitosan coating also increased the biocompatibility of the scaffolds [98]. The induction of cell proliferation by GS4012 was also observed in cell seeded scaffolds, particularly at the end of day 21. Unlike our prior NP-cell interaction study results, on NP coated scaffolds, it was observed that the toxic effect of NPs containing DIPQUO was reduced. In fact, at the end of days 7 and 14, the positive effect was seen. The reason for this was that the NPs immobilized on the scaffold surface released their content with a slower release profile due to the ionic bonds established with the surface, and thus, not a negative but even a positive effect was observed on cells. Also, immobilization of NPs is thought to increase the local concentration of bioactive substances at the cell surface, maximizing their efficiency [98]. In our study, the results of MTS and Live-Dead staining after days 7, 14, and 21 were all consistent. As a result of MTS, it was observed that cell viability increased as time passed; the same result was also visualized by Live-Dead staining. In addition, it was observed that the morphology of rBMSCs seeded on NP coated scaffolds and their attachment to scaffold surfaces were quite clear with Live-Dead staining.

The osteogenic differentiation characterizations of NP coated scaffolds were carried out, beginning with the most common one, ALP activity [34]. The early existence of ALP expression indicates the presence of osteogenic cells in the culture [151]. Aside from what was expected, a significant difference was observed between the blank NP and DG-NP coated scaffolds and the other groups. CS alone was known to induce osteogenic differentiation in rBMSCs [152]. A similar situation occurred here, and ALP activity was found to be high in blank NP coated scaffolds. Calcium assay was also performed to show differentiation and the increase in the amount of calcium together with the bone formation in all groups was consistent with the literature [153–155]. The expression of OCN is induced by mature osteoblasts, which are known as the ECM proteins of bone [143]. Gla-OCN is a type of protein that is active in bone remodeling [156]. As a result, it was

expected that the amount of Gla-OCN in the culture would grow over time. As a result of the study, it was observed that the amount of Gla-OCN increased in the medium taken from all groups. DIPQUO's significant effect on osteogenic differentiation was especially pronounced in Gla-OCN secreted groups containing this small molecule. Glu-OCN is a protein involved in energy metabolism. Therefore, the same increase was not observed for all groups. Cell energy metabolism was found to be high at all time points in the group containing both small molecules. It was observed that presence of dual small molecules in the environment increased the secretion of Glu-OCN by stimulating the energy pathways of rBMSCs. Alizarin red staining was also conducted for determination of differentiation. Red deposits in alizarin red stained scaffolds indicate calcium condensation [142–144]. Looking at day 21 images, it was observed that the NPs alone affected bone differentiation due to the presence of chitosan [157], but the highest differentiation was observed in the presence of osteogenic factor DIPQUO [84]. In von Kossa staining, on the other hand, the color of the scaffolds was dark brown in behalf of calcium accumulation, and even near-black accumulations were observed at the end of 21 days [158]. Then, it was seen in all groups that osteoblast differentiation of rBMSCs was performed successfully, and accordingly, calcium deposition took place on the entire scaffold surface.

Consequently, real-time PCR analysis was used to determine the expression of the ONC, Runx2, and collagen type I genes. In this study, it was observed that the expression of ONC, a late marker, increased as time passed [159]. Since ONC is a late marker, its concentration in the culture is expected to increase over time. ONC synthesis was also increased with the induction of osteogenic differentiation, especially in groups containing DIPQUO. Onether transcription factor that affects differentiation is called Runx2. The Runx2 gene controls osteogenesis by employing a G protein-coupled signaling pathway to encourage the up-regulation of ECM proteins unique to bones, like ALP, OCN, and BSP [151]. Runx2 is an early marker and therefore has an early effect on bone differentiation [80]. At the end of day 7, it was seen that the dual NP coated scaffolds were more effective than the other groups. At the end of 21 days, this difference created by DG-NP disappeared, and a significant difference was observed in the group with G-NP compared to other groups. Collagen type 1 (Col1a1) represents over 90% of the protein in bone [160]. Immature osteoblasts are in charge of expressing collagen type I, which is referred to as the ECM protein of bone [28]. From days 7 to 14, Col1a1 expression was lower in the

DG-NP coated group compared to the control group. It was more noticeable on day 7 since immature osteoblasts were responsible for its expression. It might be connected to the bone remodeling cycle, which exhibits osteoclasts demineralizing collagen [80]. The potential for osteoblast recruitment may also be impacted [39]. From day 14 to day 21, there was an increase in collagen expression as the bone repair progressed. In addition, collagen expression was found to be higher in D-NP, the other group containing DIPQUO, compared to other groups. From this, it can be concluded that DIPQUO is effective in bone regeneration.

Vascularization is of great importance in bone regeneration [91,161,162]. Therefore, the vascularization capacity of NP coated scaffolds with endothelial cells was studied. In the first part, the *in vitro* angiogenesis capacity of GS4012 alone and in NP embedded forms were investigated. The vascularization effect of GS4012 was demonstrated in previous studies and has been proven again in this study [87,88,90,163]. In this study, additionally, it was observed that GS4012 in NP was more effective than giving it directly to the medium, which, together with chitosan, induced more tubular structure formation of endothelial cells. Chitosan induces angiogenesis by acting like heparin and taking part in the formation of new blood vessels [164]. A migration assay was performed to prove that GS4012 is a VEGF inducer and invites endothelial cells to its environment [163]. GS4012 increases VEGF expression [88]. Here, it was demonstrated that GS4012 attracted endothelial cells, similar to the literature. Besides, GS4012 in NP was shown to be more effective. After GS4012 was shown to recruit endothelial cells, immunofluorescence staining was performed to prove its effect on NP coated scaffolds. In this part the migration of rPBECs from the inserts to the rBMSC seeded NP coated scaffolds was investigated. It was seen that blank NP coated scaffolds called rPBECs due to the presence of chitosan, but they were not as effective as GS4012 in the medium. It was proven that GS4012 can strengthen angiogenesis by summoning most of the endothelial cells to the environment and by ensuring the attachment of these endothelium to the scaffolds.

6. CONCLUSION

In this study, two small molecules, GS4012, an activator of VEGF, which plays a central role in vascularization, and DIPQUO, a newly discovered small molecule for bone-like structure differentiation, were encapsulated into chitosan NPs to find a solution to the failures due to insufficient vascularity frequently encountered, which is the most important basis in BTE studies. It was also aimed that by coating these NPs on PLA scaffolds printed with a 3D printer, endothelial cells would migrate to the defect area and lead to vascularization and eventually the formation of mature bone tissue.

First of all, PLA scaffolds, NPs, and NP-coated PLA scaffolds were produced. In the first step, PLA scaffolds were prepared by a 3D printer. The effects of the different pore sizes of 3D-printed scaffolds that are used in BTE were thoroughly assessed from a larger perspective. The chemical and mechanical characterization of different pore sizes of 3D-printed scaffolds showed that scaffolds with a 60 % filling rate had optimum features for use in BTE applications. Furthermore, in vitro assessment of the 3D-printed PLA scaffold showed that cellular adhesion was provided at all filling rates of the scaffolds. Also, it was reported that the pore size of polymer scaffolds was found to play a more important role, as the ones with a larger pore size significantly enhanced the migration of rBMSCs. However, the differentiation potential of cells into bone cells was most effectively achieved when the 3D-printed PLA scaffold had a fill rate of 60 %. The surface of the scaffolds that had a 60 % filling rate was treated with alkali to open the active group; the treatments made the scaffolds biologically compatible, and a suitable environment was prepared for the binding of NPs.

Then, physical and chemical characterizations and optimum conditions for CS-NP synthesis were determined. Chitosan, which is the preferred polymer for NP production, accelerates bone remodeling with its own osteogenic and angiogenic induction. NPs to be used in scaffold coating were synthesized and characterized by loading the osteogenic factor DIPQUO and the angiogenic factor GS4012 on NPs under optimum conditions.

Finally, the NPs' with all of the optimum conditions was coated on treated scaffolds surface, and the material's suitability in BTE applications was evaluated from a broad perspective.

At the end of the study, it was shown that rBMSCs successfully differentiated into osteoblasts due to the controlled release of DIPQUO, and GS4012 provided vascularization by affecting the migration of rPBECs to the environment. With the loading of small molecules into the NP, the desired amount was released without any toxic effect, and the effect was strengthened with controlled release.

It is known that the achivement of vascularization of bone tissue provides a solution to the failures due to insufficient vascularity encountered in animal experiments and clinical studies using BTE. In addition, it will be possible to prevent the long term recovery and convalescence process caused by these failures on the patient's side, as well as job loss, moral collapse, and economic losses in this process.

7. FUTURE PROSPECTS

TE is a vibrant field that is constantly evolving. New biomaterials with better properties are always being researched in this area. In this study, 3D scaffolds were produced to solve the problem of insufficient vascularization in the bone defect area and to induce bone differentiation with the controlled release of these molecules by loading osteogenic and angiogenic factors into NP. In the future, other small molecules may be attempted to induce osteogenesis and/or angiogenesis. The polymer used for the carrier system of these small molecules or the production method can be changed. *In vivo* studies can be used to demonstrate the success of these developed scaffolds in an experimental model.

REFERENCES

1. Favus MJ, Goltzman D. Regulation of Calcium and Magnesium. *Prim. Metab. Bone Dis. Disord. Miner. Metab. Eighth Ed.* 2013:171-79.

2. Salgado AJ, Coutinho OP, Reis RL. Bone Tissue Engineering: State of the Art and Future Trends. *Macromol Biosci*. 2004;4(8):743–65.

3. Safadi FF, Barbe MF, Abdelmagid SM, Rico MC, Aswad RA, Litvin J, et al. Bone Structure, Development and Bone Biology. *Bone Pathol.* 2009:1–50.

4. Lynnerup N, Klaus HD. Fundamentals of Human Bone and Dental Biology. *Ortner's Identif. Pathol. Cond. Hum. Skelet. Remain.* 2019:35–58.

5. Betts JG, Young KA, Wise JA, Poe B, Kruse DH, Korol O, et al. Bone Tissue and Skeletal System. *Anat. Physiol.* 2013:6.

6. Morgan EF, Barnes GL, Einhorn TA. The Bone Organ System. Form and Function. Fourth Edi. 2013:3-20.

7. Olszta MJ, Cheng X, Jee SS, Kumar R, Kim Y-Y, Kaufman MJ, et al. Bone structure and formation: A new perspective. *Mater Sci Eng R*. 2007;58:77–116.

8. Luz GM, Mano JF. Mineralized structures in nature: Examples and inspirations for the design of new composite materials and biomaterials. *Compos Sci Technol*. 2010;70:1777–88.

9. Halpert I, Sires UI, Roby JD, Potter-Perigo S, Wight TN, Shapiro SD, et al. Matrilysin is expressed by lipid-laden macrophages at sites of potential rupture in atherosclerotic lesions and localizes to areas of versican deposition, a proteoglycan substrate for the enzyme. *Proc Natl Acad Sci U S A*. 1996.

10. Meyer U, Wiesmann H. Bone and Cartilage. *Bone Cartil. Eng.* 2006:7–46.

11. Gosman JH. The Molecular Biological Approach in Paleopathology. *A Companion to Paleopathol.* 2012:76-96.

12. Boyle WJ, Simonet WS, Lacey DL. Osteoclast differentiation and activation. *Nature*. 2003;423(6937):337-42.

13. Zreiqat H, Dunstan CR, Rosen V. *A Tissue Regeneration Approach to Bone and Cartilage Repair*. Cham: Springer International Publishing; 2015.

14. Laurencin CT, Ashe KM, Henry N, Kan HM, Lo KW-H. Delivery of small molecules for bone regenerative engineering: preclinical studies and potential clinical applications. *Drug Discov Today*. 2014;19(6):794–800.

15. Majidinia M, Sadeghpour A, Yousefi B. The roles of signaling pathways in bone repair and regeneration. *J Cell Physiol*. 2018;233(4):2937–48.

16. Elbackly RM, Mastrogiacomo M, Cancedda R. *Regenerative Medicine Applications in Organ Transplantation*. Cambridge: Academic Press; 2014.

17. Mano J., Silva G., Azevedo H., Malafaya P., Sousa R., Silva S., et al. Natural origin biodegradable systems in tissue engineering and regenerative medicine: present status and some moving trends. *J R Soc Interface*. 2007;4(17):999–1030.

18. Moreno Madrid AP, Vrech SM, Sanchez MA, Rodriguez AP. Advances in additive manufacturing for bone tissue engineering scaffolds. *Mater Sci Eng C*. 2019;100:631–44.

19. Hart NH, Nimphius S, Rantalainen T, Ireland A, Siafarikas A, Newton RU. Mechanical basis of bone strength: Influence of bone material, bone structure and muscle action. *J Musculoskelet Neuronal Interact*. 2017;17:114–39.

20. Khan WS, Rayan F, Dhinsa BS, Marsh D. An Osteoconductive, Osteoinductive, and Osteogenic Tissue-Engineered Product for Trauma and Orthopaedic Surgery: How Far Are We? *Stem Cells Int*. 2012;2012:1–7.

21. Holmes A, Brown R, Shakesheff K. Engineering tissue alternatives to animals: Applying tissue engineering to basic research and safety testing. *Regen Med*. 2009;4:579–92.

22. Bala Y, Seeman E. Bone's Material Constituents and their Contribution to Bone Strength in Health, Disease, and Treatment. *Calcif Tissue Int*. 2015;97:308–26.

23. Burg KJL, Porter S, Kellam JF. Biomaterial developments for bone tissue engineering. *Biomaterials*. 2000;21:2347–59.

24. Meyer U, Joos U, Wiesmann HP. Biological and biophysical principles in extracorporal bone tissue engineering. Part I. *Int J Oral Maxillofac Surg*. 2004;33:325–32.

25. Cancedda R, Dozin B, Giannoni P, Quarto R. Tissue engineering and cell therapy of cartilage and bone. *Matrix Biol*. 2003;22(1):81–91.

26. Bruder SP, Jaiswal N, Ricalton NS, Mosca JD, Kraus KH, Kadiyala S. Mesenchymal stem cells in osteobiology and applied bone regeneration. *Clin Orthop Relat Res*. 1998;355:247–56.

27. Risbud M V, Sittinger M. Tissue engineering: advances in in vitro cartilage generation. *Trends Biotechnol*. 2002;20(8):351–6.

28. Deng H, Liu Y, Guo C, Di Chen. *Current Topics in Bone Biology*. Singapore: World Scientific; 2005.

29. Nantavisai S, Egusa H, Osathanon T, Sawangmake C. Mesenchymal stem cell-based bone tissue engineering for veterinary practice. *Heliyon*. 2019;5.

30. Black CRM, Goriainov V, Gibbs D, Kanczler J, Tare RS, Oreffo ROC. Bone Tissue Engineering. *Curr Mol Biol Reports*. 2015;1(3):132–40.

31. Sundelacruz S, Kaplan DL. Stem cell- and scaffold-based tissue engineering approaches to osteochondral regenerative medicine. *Semin Cell Dev Biol*. 2009;20(6):646–55.

32. Zhang M, Grote C, Wang J. Epigenetic mechanisms underlying the pathogenesis of osteoarthritis and their clinical relevance. *Progn. Epigenetics*. 2019: 245–68.

33. Komori T, Yagi H, Nomura S, Yamaguchi A, Sasaki K, Deguchi K, et al. Targeted disruption of Cbfa1 results in a complete lack of bone formation owing to maturational arrest of osteoblasts. *Cell*. 1997;89(5):755-64.

34. Atkins GJ, Findlay DM, Anderson PH, Morris HA. Target Genes: Bone Proteins. *Vitam. D*. 2005:711–20.

35. Wei J, Shimazu J, Makinistoglu MP, Maurizi A, Kajimura D, Zong H, et al. Glucose Uptake and Runx2 Synergize to Orchestrate Osteoblast Differentiation and Bone

Formation. *Cell*. 2015;161(7):1576–91.

36. Naylor KE, Eastell R. Measurement of Biochemical Markers of Bone Formation. *Dyn. Bone Cartil. Metab.* 2006:529-40.

37. Kraenzlin ME, Seibel MJ. Measurement of Biochemical Markers of Bone Resorption. *Dyn. Bone Cartil. Metab.* 2006:541–63.

38. Williams DF. There is no such thing as a biocompatible material. *Biomaterials*. 2014;35(38):10009–14.

39. Khang G. *Handbook of Intelligent Scaffolds for Tissue Engineering and Regenerative Medicine*. Singapore: Jenny Stanford Publishing; 2017.

40. Rice JJ, Martino MM, De Laporte L, Tortelli F, Briquez PS, Hubbell JA. Engineering the Regenerative Microenvironment with Biomaterials. *Adv Healthc Mater*. 2013;2(1):57–71.

41. Puppi D, Chiellini F, Piras AM, Chiellini E. Polymeric materials for bone and cartilage repair. *Prog Polym Sci*. 2010;35(4):403–40.

42. Bonzani IC, George JH, Stevens MM, Basu A, Schneider J. Novel materials for bone and cartilage regeneration. *Curr Opin Chem Biol*. 2006;10:568–75.

43. Lopes MS, Jardini AL, Filho RM. Poly (Lactic Acid) Production for Tissue Engineering Applications. *Procedia Eng*. 2012;42:1402–13.

44. Lasprilla AJR, Martinez GAR, Lunelli BH, Jardini AL, Filho RM. Poly-lactic acid synthesis for application in biomedical devices — A review. *Biotechnol Adv*. 2012;30(1):321–8.

45. Bouapao L, Tsuji H, Tashiro K, Zhang J, Hanesaka M. Crystallization, spherulite growth, and structure of blends of crystalline and amorphous poly(lactide)s. *Polymer (Guildf)*. 2009;50:4007–17.

46. Karande RD, Abitha VK, Rane AV, Mishra RK. Preparation of polylactide from synthesized lactic acid and effect of reaction parameters on conversion. *J Mater Sci Eng with Adv Technol*. 2016;12(1–2):1–37.

47. Chan CM, Vandi LJ, Pratt S, Halley P, Richardson D, Werker A, et al. Composites of Wood and Biodegradable Thermoplastics: A Review. *Polym Rev*. 2018;58(3):444–94.

48. Jamshidian M, Tehrany EA, Imran M, Jacquot M, Desobry S. Poly-Lactic Acid: Production, Applications, Nanocomposites, and Release Studies. *Compr Rev Food Sci Food Saf*. 2010;9(5):552–71.

49. Rasal RM, Janorkar A V, Hirt DE. Poly(lactic acid) modifications. *Prog Polym Sci*. 2010;35(3):338–56.

50. Auras R, Harte B, Selke S. An Overview of Polylactides as Packaging Materials. *Macromol Biosci*. 2004;4(9):835–64.

51. Farah S, Anderson DG, Langer R. Physical and mechanical properties of PLA, and their functions in widespread applications — A comprehensive review. *Adv Drug Deliv Rev*. 2016;107:367–92.

52. Mitragotri S, Lahann J. Physical approaches to biomaterial design. *Nat Mater*. 2009;8(1):15–23.

53. Gross BC, Erkal JL, Lockwood SY, Chen C, Spence DM. Evaluation of 3D Printing and Its Potential Impact on Biotechnology and the Chemical Sciences. *Anal Chem*. 2014;86(7):3240–53.

54. Chia HN, Wu BM. Recent advances in 3D printing of biomaterials. *J Biol Eng*. 2015;9(1):4.

55. Lutton C, Read J, Trau M. Nanostructured biomaterials: A novel approach to artificial bone implants. *Aust. J. Chem.* 2001;54(10):621.

56. Rezvani Z, Venugopal JR, Urbanska AM, Mills DK, Ramakrishna S, Mozafari M. A bird's eye view on the use of electrospun nanofibrous scaffolds for bone tissue engineering: Current state-of-the-art, emerging directions and future trends. *Nanomedicine Nanotechnology, Biol Med*. 2016;12(7):2181–200.

57. Liu H, Ding X, Zhou G, Li P, Wei X, Fan Y. Electrospining of nanofibers for tissue engineering applications. *J Nanomater*. 2013;2013(37):1–31.

58. Ghosal K, Agatemor C, Špitálsky Z, Thomas S, Kny E. Electrospinning tissue engineering and wound dressing scaffolds from polymer-titanium dioxide nanocomposites. *Chem Eng J*. 2019;358:1262–78.

59. Soundarya SP, Menon AH, Chandran SV, Selvamurugan N. Bone tissue engineering: Scaffold preparation using chitosan and other biomaterials with different design and fabrication techniques. *Int J Biol Macromol*. 2018;119:1228–39.

60. Sultana N. *Biodegradable Polymer-Based Scaffolds for Bone Tissue Engineering*. Berlin: Springer;2013.

61. Hull C. Apparatus for production of three-dimensional objects by stereolithography, US6027324A (Patent) 1986.

62. Roseti L, Parisi V, Petretta M, Cavallo C, Desando G, Bartolotti I, et al. Scaffolds for Bone Tissue Engineering: State of the art and new perspectives. *Mater Sci Eng C*. 2017;78:1246–62.

63. Zhang L, Yang G, Johnson BN, Jia X. Three-dimensional (3D) printed scaffold and material selection for bone repair. *Acta Biomater*. 2019;84:16–33.

64. Sachs EM, Haggerty JS, Cima MJ, Williams PA. Three-dimensional printing techniques, US5204055A (Patent) 1993.

65. Melchels FP, Feijen J, Grijpma DW. A review on stereolithography and its applications in biomedical engineering. *Biomaterials*. 2010;31:6121–30.

66. Zein I, Hutmacher DW, Cheng Tan K, Hin Teoh S. Fused deposition modeling of novel scaffold architectures for tissue engineering applications. *Biomater.* 2002;23(4):1169-85.

67. Grémare A, Guduric V, Bareille R, Heroguez V, Latour S, L'heureux N, et al. Characterization of printed PLA scaffolds for bone tissue engineering. *J Biomed Mater Res - Part A*. 2018;106(4):887–94.

68. Findrik Balogová A, Hudák R, Tóth T, Schnitzer M, Feranc J, Bakoš D, et al. Determination of geometrical and viscoelastic properties of PLA/PHB samples

made by additive manufacturing for urethral substitution. *J Biotechnol*. 2018;284(March):123–30.

69. Ji S, Dube K, Chesterman JP, Fung SL, Liaw C-Y, Kohn J, et al. Polyester-based ink platform with tunable bioactivity for 3D printing of tissue engineering scaffolds. *Biomater Sci*. 2019;7(2):560–70.

70. Liu J, Yan C. 3D Printing of Scaffolds for Tissue Engineering. *3D Print.* 2018: 138–54.

71. Bae E-J, Kim J-H, Kim W-C, Kim H-Y. Bond and fracture strength of metal-ceramic restorations formed by selective laser sintering. *J Adv Prosthodont*. 2014;6:266–71.

72. Mazzoli A. Selective laser sintering in biomedical engineering. *Med Biol Eng Comput*. 2013;51(3):245–56.

73. Mandrycky C, Wang Z, Kim K, Kim D-H. 3D bioprinting for engineering complex tissues. *Biotechnol Adv*. 2016;34(4):422–34.

74. Aravamudhan A, M. Ramos D, Nip J, Subramanian A, James R, D. Harmon M, et al. Osteoinductive Small Molecules: Growth Factor Alternatives for Bone Tissue Engineering. *Curr Pharm Des*. 2013;19(19):3420–8.

75. Ayala R, Zhang C, Yang D, Hwang Y, Aung A, Shroff SS, et al. Engineering the cell–material interface for controlling stem cell adhesion, migration, and differentiation. *Biomaterials*. 2011;32(15):3700–11.

76. Rose FRAJ, Oreffo ROC. Bone Tissue Engineering: Hope vs Hype. *Biochem Biophys Res Commun*. 2002;292(1):1–7.

77. Vo TN, Kasper FK, Mikos AG. Strategies for controlled delivery of growth factors and cells for bone regeneration. *Adv Drug Deliv Rev*. 2012;64:1292–309.

78. Azevedo HS, Pashkuleva I. Biomimetic supramolecular designs for the controlled release of growth factors in bone regeneration. *Adv Drug Deliv Rev*. 2015;94:63–76.

79. Gothard D, Smith EL, Kanczler JM, Rashidi H, Qutachi O, Henstock J, et al. Tissue engineered bone using select growth factors: A comprehensive review of animal

studies and clinical translation studies in man. *Eur Cells Mater*. 2014;28:166–208.

80. Hollinger JO, Einhorn TA, Doll BA, Sfeir C. *Bone Tissue Engineering*. London: CRC Press;2005.

81. Lo KW-H, Ashe KM, Kan HM, Laurencin CT. The role of small molecules in musculoskeletal regeneration. *Regen Med*. 2012;7(4):535–49.

82. Spring DR. Chemical genetics to chemical genomics: Small molecules offer big insights. *Chem Soc Rev*. 2005;34(6):472–482.

83. Han QQ, Du Y, Yang PS. The role of small molecules in bone regeneration. *Future Med Chem*. 2013;5(14):1671–84.

84. Cook B, Rafiq R, Lee H, Banks KM, El-Debs M, Chiaravalli J, et al. Discovery of a Small Molecule Promoting Mouse and Human Osteoblast Differentiation via Activation of p38 MAPK-β. *Cell Chem Biol*. 2019;26(7):926-35.

85. Daigang L, Jining Q, Jinlai L, Pengfei W, Chuan S, Liangku H, et al. LPS-stimulated inflammation inhibits BMP-9-induced osteoblastic differentiation through crosstalk between BMP/MAPK and Smad signaling. *Exp Cell Res*. 2016;341(1):54–60.

86. Thouverey C, Caverzasio J. Focus on the p38 MAPK signaling pathway in bone development and maintenance. *Bonekey Rep*. 2015;4:711.

87. Sato TN. *Mechanical and Chemical Signaling in Angiogenesis*. Berlin: Springer;2013.

88. Peterson RT, Shaw SY, Peterson TA, Milan DJ, Zhong TP, Schreiber SL, et al. Chemical suppression of a genetic mutation in a zebrafish model of aortic coarctation. *Nat Biotechnol*. 2004;22(5):595–9.

89. Rennekamp AJ, Peterson RT. 5 years of zebrafish chemical screening. *Curr Opin Chem Biol*. 2015;24:58–70.

90. Wu YC, Chang CY, Kao A, Hsi B, Lee SH, Chen YH, et al. Hypoxia-induced retinal neovascularization in zebrafish embryos: A potential model of retinopathy of prematurity. *PLoS One*. 2015;10(5):1–17.

91. Hu K, Olsen BR. The roles of vascular endothelial growth factor in bone repair and regeneration. *Bone*. 2016;91:30–8.

92. Grosso A, Burger MG, Lunger A, Schaefer DJ, Banfi A, Di Maggio N. It Takes Two to Tango: Coupling of Angiogenesis and Osteogenesis for Bone Regeneration. *Front Bioeng Biotechnol*. 2017;5(Nov):1–7.

93. De Witte T-MM, Fratila-Apachitei LE, Zadpoor AA, Peppas NA. Bone tissue engineering via growth factor delivery: from scaffolds to complex matrices. *Regen Biomater*. 2018;5(June):197–211.

94. Lienemann PS, Lutolf MP, Ehrbar M. Biomimetic hydrogels for controlled biomolecule delivery to augment bone regeneration. *Adv Drug Deliv Rev*. 2012;64(12):1078–89.

95. Lee K, Silva EA, Mooney DJ. Growth factor delivery-based tissue engineering: general approaches and a review of recent developments. *J R Soc Interface*. 2011;8(55):153–70.

96. Draenert FG, Nonnenmacher AL, Kämmerer PW, Goldschmitt J, Wagner W. BMP-2 and bFGF release and in vitro effect on human osteoblasts after adsorption to bone grafts and biomaterials. *Clin Oral Implants Res*. 2013;24(7):750–7.

97. Wang Z, Wang K, Lu X, Li M, Liu H, Xie C, et al. Bmp-2 encapsulated polysaccharide nanoparticle modified biphasic calcium phosphate scaffolds for bone tissue regeneration. *J Biomed Mater Res - Part A*. 2015;103:1520–32.

98. Monteiro N, Martins A, Reis RL, Neves NM. Nanoparticle-based bioactive agent release systems for bone and cartilage tissue engineering. *Regen Ther*. 2015;1:109–18.

99. Sarukawa J, Takahashi M, Abe M, Suzuki D, Tokura S, Furuike T, et al. Effects of chitosan-coated fibers as a scaffold for three-dimensional cultures of rabbit fibroblasts for ligament tissue engineering. *J Biomater Sci Polym Ed*. 2011;22(4–6):717–32.

100. Rajam M, Pulavendran S, Rose C, Mandal AB. Chitosan nanoparticles as a dual growth factor delivery system for tissue engineering applications. *Int J Pharm*.

2011;410(1–2):145–52.

101. Shahrezaee M, Salehi M, Keshtkari S, Oryan A, Kamali A, Shekarchi B. In vitro and in vivo investigation of PLA/PCL scaffold coated with metformin-loaded gelatin nanocarriers in regeneration of critical-sized bone defects. *Nanomedicine Nanotechnology, Biol Med*. 2018;14(7):2061–73.

102. Parajó Y, D'Angelo I, Welle A, Garcia-Fuentes M, Alonso MJ. Hyaluronic acid/Chitosan nanoparticles as delivery vehicles for VEGF and PDGF-BB. *Drug Deliv*. 2010;17(8):596–604.

103. Niu X, Feng Q, Wang M, Guo X, Zheng Q. Porous nano-HA/collagen/PLLA scaffold containing chitosan microspheres for controlled delivery of synthetic peptide derived from BMP-2. *J Control Release*. 2009;134(2):111–7.

104. Corona-Gomez J, Chen X, Yang Q, Puoci F. Functional Biomaterials Effect of Nanoparticle Incorporation and Surface Coating on Mechanical Properties of Bone Scaffolds: A Brief Review. *J Funct Biomater*. 2016;7:18.

105. Vieira SS, Vial S, Reis RL, Oliveira JM. Nanoparticles for Bone Tissue Engineering. *Biotechnol Prog*. 2017;33(April):1–22.

106. Queiroz MF, Melo KRT, Sabry DA, Rocha HAO. Does the Use of Chitosan Contribute to Oxalate Kidney Stone Formation? *Mar Drugs*. 2014;13(1):141–58.

107. Ferreira Tomaz A, Sobral de Carvalho S, Cardoso Barbosa R, L. Silva S, Sabino Gutierrez M, B. de Lima A, et al. Ionically Crosslinked Chitosan Membranes Used as Drug Carriers for Cancer Therapy Application. *Materials (Basel)*. 2018;11(10):2051.

108. Ravichandran V, Kesavan V, Cojean S, Loiseau PM, Jayakrishnan A. Polysorbate Surfactants as Drug Carriers: Tween 20-Amphotericin B Conjugates as Anti-Fungal and Anti-Leishmanial Agents. *Curr Drug Deliv*. 2018;15(7):1028–37.

109. Banu VRN, Rajendran S. Corrosion inhibition of carbon steel by tween 20 self-assembling monolayers. *J Chem Pharm Res*. 2015;7(10):127–32.

110. Nandiyanto ABD, Oktiani R, Ragadhita R. Indonesian Journal of Science &

Technology How to Read and Interpret FTIR Spectroscope of Organic Material. *Indones J Sci Technol*. 2019;4(1):97–118.

111. Qi L, Xu Z. Lead sorption from aqueous solutions on chitosan nanoparticles. *Physicochem Eng Asp*. 2004;251:183–90.

112. Moxon SR, Ferreira MJS, Santos P dos, Popa B, Gloria A, Katsarava R, et al. A Preliminary Evaluation of the Pro-Chondrogenic Potential of 3D-Bioprinted Poly(ester Urea) Scaffolds. *Polymers (Basel)*. 2020;12(7):1478.

113. Gregor A, Filová E, Novák M, Kronek J, Chlup H, Buzgo M, et al. Designing of PLA scaffolds for bone tissue replacement fabricated by ordinary commercial 3D printer. *J Biol Eng*. 2017;11(1):31.

114. Cuiffo MA, Snyder J, Elliott AM, Romero N, Kannan S, Halada GP. Impact of the Fused Deposition (FDM) Printing Process on Polylactic Acid (PLA) Chemistry and Structure. *Appl Sci*. 2017;7(6):579.

115. Choksi N, Desai H. Synthesis of Biodegradable Polylactic Acid Polymer By Using Lactic Acid Monomer. *Int J Appl Chem*. 2017;13(2):377–84.

116. Vouyiouka SN, Papaspyrides CD. Mechanistic Aspects of Solid-State Polycondensation. *Polym. Sci. A Compr. Ref.*vol. 4. 2012: 857–74.

117. Baran E, Erbil H. Surface Modification of 3D Printed PLA Objects by Fused Deposition Modeling: A Review. *Colloids and Interfaces*. 2019;3(2):43.

118. Bose S, Roy M, Bandyopadhyay A. Recent advances in bone tissue engineering scaffolds. *Trends Biotechnol*. 2012;30(10):546–54.

119. Turnbull G, Clarke J, Picard F, Riches P, Jia L, Han F, et al. 3D bioactive composite scaffolds for bone tissue engineering. *Bioact Mater*. 2018;3(3):278–314.

120. Donate R, Monzón M, Alemán-Domínguez ME. Additive manufacturing of PLA-based scaffolds intended for bone regeneration and strategies to improve their biological properties. *E-Polymers*. 2020;20(1):571–99.

121. Murphy CM, Matsiko A, Haugh MG, Gleeson JP, O'Brien FJ. Mesenchymal stem cell fate is regulated by the composition and mechanical properties of collagen–

glycosaminoglycan scaffolds. *J Mech Behav Biomed Mater*. 2012;11:53–62.

122. Cheng C-H, Shie M-Y, Lai Y-H, Foo N-P, Lee M-J, Yao C-H. Fabrication of 3D Printed Poly(lactic acid)/Polycaprolactone Scaffolds Using TGF-β1 for Promoting Bone Regeneration. *Polymers (Basel)*. 2021;13(21):3731.

123. Urinov E, Hanstein S, Weidenkaff A. Enzymatic Degradation of Fiber-Reinforced PLA Composite Material. *Macromol*. 2022;2(4):522–30.

124. Xu L, Crawford K, Gorman CB. Effects of Temperature and pH on the Degradation of Poly(lactic acid) Brushes. *Macromolecules*. 2011;44(12):4777–82.

125. Danaei M, Dehghankhold M, Ataei S, Hasanzadeh Davarani F, Javanmard R, Dokhani A, et al. Impact of Particle Size and Polydispersity Index on the Clinical Applications of Lipidic Nanocarrier Systems. *Pharmaceutics*. 2018;10(2):57.

126. Raval N, Maheshwari R, Kalyane D, Youngren-Ortiz SR, Chougule MB, Tekade RK. Importance of Physicochemical Characterization of Nanoparticles in Pharmaceutical Product Development. *Basic Fundam. Drug Deliv.* 2019: 369–400.

127. Aksu D, Büyük Nİ, Köse GT. Nanotoksikoloji. *Nanobiyoteknoloji*. 1. Baskı. 2021: 58–66.

128. Xu Y, Du Y. Effect of molecular structure of chitosan on protein delivery properties of chitosan nanoparticles. *Int J Pharm*. 2003;250(1):215–26.

129. Qi L, Xu Z. Lead sorption from aqueous solutions on chitosan nanoparticles. *Colloids Surfaces A Physicochem Eng Asp*. 2004;251(1):183–90.

130. Malhotra M, Lane C, Tomaro-Duchesneau C, Saha S, Prakash S. A novel method for synthesizing PEGylated chitosan nanoparticles: strategy, preparation, and in vitro analysis. *Int J Nanomedicine*. 2011;6:485–94.

131. Ferrero F, Periolatto M. Antimicrobial finish of textiles by chitosan UV-curing. *J Nanosci Nanotechnol*. 2012;12(6):4803-10.

132. Ahmad N, Khalid MS, Al Ramadhan AM, Alaradi MZ, Al Hammad MR, Ansari K, et al. Preparation of melatonin novel-mucoadhesive nanoemulsion used in the treatment of depression. *Polym Bull*. 2022.

133. Yang J-M, Jiang C-N, Dong H, Fang D. Synthesis of 1-carbamatoalkyl-2-naphthols in Tween® 20 Aqueous Micelles. *J Chem Res*. 2013;37(5):279–81.

134. Dounighi M, Eskandari R, Zolfagharian H, Mohammad M. Preparation and in vitro characterization of chitosan nanoparticles containing Mesobuthus eupeus scorpion venom as an antigen delivery system. *J Venom Anim Toxins Incl Trop Dis*. 2012;18(1):44–52.

135. Rozana R, Yulizar Y, Saefumillah A, Apriandanu DOB. Synthesis, characterization and in vitro release study of efavirenz-loaded chitosan nanoparticle. *AIP Conf. Proc.* 2020: 040004.

136. Tan Q, Tang H, Hu J, Hu Y, Zhou X, Tao R, et al. Controlled release of chitosan/heparin nanoparticle-delivered VEGF enhances regeneration of decellularized tissue-engineered scaffolds. *Int J Nanomedicine*. 2011;6:929.

137. Chen S, Zhu J, Cheng J. Preparation and in vitro evaluation of a novel combined multiparticulate delayed-onset sustained-release formulation of diltiazem hydrochloride. *Die Pharm - An Int J Pharm Sci*. 2007;62(12):907–13.

138. Furuike T, Nagahama H, Chaochai T, Tamura H. Preparation and Characterization of Chitosan-Coated Poly(l-Lactic Acid) Fibers and Their Braided Rope. *Fibers*. 2015;3(4):380–93.

139. Chen W, Nichols L, Brinkley F, Bohna K, Tian W, Priddy MW, et al. Alkali treatment facilitates functional nano-hydroxyapatite coating of 3D printed polylactic acid scaffolds. *Mater Sci Eng C*. 2021;120(October):111686.

140. Thitiset T, Buranapraditkul S, Damrongsakkul S, Honsawek S. Isolation and cellular properties of mesenchymal stem cells from human periosteum. *Asian Biomed*. 2013;7(6):777–85.

141. Sareen N, Sequiera GL, Chaudhary R, Abu-El-Rub E, Chowdhury SR, Sharma V, et al. Early passaging of mesenchymal stem cells does not instigate significant modifications in their immunological behavior. *Stem Cell Res Ther*. 2018;9(1):121.

142. Kumar K, Das K, Madhusoodan A, Kumar A, Singh P, Mondal T, et al. Rat bone marrow derived mesenchymal stem cells differentiate to germ cell like cells.

BioRxiv. 2018:1–21.

143. Castrén E, Sillat T, Oja S, Noro A, Laitinen A, Konttinen YT, et al. Osteogenic differentiation of mesenchymal stromal cells in two-dimensional and three-dimensional cultures without animal serum. *Stem Cell Res Ther*. 2015;6(1):167.

144. Miron RJ, Zhang YF. Osteoinduction: A review of old concepts with new standards. *J Dent Res*. 2012;91(8):736–44.

145. Han F, Zhou F, Yang X, Zhao J, Zhao Y, Yuan X. A pilot study of conically graded chitosan-gelatin hydrogel/PLGA scaffold with dual-delivery of TGF-β1 and BMP-2 for regeneration of cartilage-bone interface. *J Biomed Mater Res - Part B Appl Biomater*. 2015;103(7):1344–53.

146. Zhang L, Chan C. Isolation and Enrichment of Rat Mesenchymal Stem Cells (MSCs) and Separation of Single-colony Derived MSCs. *J Vis Exp*. 2010;(37):2–5.

147. Punshon G, Vara DS, Sales KM, Seifalian AM. A novel method for the extraction and culture of progenitor stem cells from human peripheral blood for use in regenerative medicine. *Biotechnol Appl Biochem*. 2011;58(5):328–34.

148. Voyta JC, Via DP, Butterfield CE, Zetter BR. Identification and isolation of endothelial cells based on their increased uptake of acetylated-low density lipoprotein. *J Cell Biol*. 1984;99(6):2034–40.

149. Ruijtenberg S, van den Heuvel S. Coordinating cell proliferation and differentiation: Antagonism between cell cycle regulators and cell type-specific gene expression. *Cell Cycle*. 2016;15(2):196.

150. Kuru L, Griffiths GS, Petrie A, Olsen I. Alkaline phosphatase activity is upregulated in regenerating human periodontal cells. *J Periodontal Res*. 1999;34(2):123–7.

151. You M-H, Kwak MK, Kim D-H, Kim K, Levchenko A, Kim D-Y, et al. Synergistically Enhanced Osteogenic Differentiation of Human Mesenchymal Stem Cells by Culture on Nanostructured Surfaces with Induction Media. *Biomacromolecules*. 2010;11(7):1856–62.

152. Mathews S, Gupta PK, Bhonde R, Totey S. Chitosan enhances mineralization

during osteoblast differentiation of human bone marrow-derived mesenchymal stem cells, by upregulating the associated genes. *Cell Prolif*. 2011;44(6):537–49.

153. Witek L, Shi Y, Smay J. Controlling calcium and phosphate ion release of 3D printed bioactive ceramic scaffolds: An in vitro study. *J Adv Ceram*. 2017;6(2):157–64.

154. Cushnie EK, Ulery BD, Nelson SJ, Deng M, Sethuraman S, Doty SB, et al. Simple Signaling Molecules for Inductive Bone Regenerative Engineering. *PLoS One*. 2014;9(7):e101627.

155. Chu L, Jiang G, Hu X-L, James TD, He X-P, Li Y, et al. Biodegradable macroporous scaffold with nano-crystal surface microstructure for highly effective osteogenesis and vascularization. *J Mater Chem B*. 2018;6(11):1658–67.

156. Razny U, Fedak D, Kiec-Wilk B, Goralska J, Gruca A, Zdzienicka A, et al. Carboxylated and undercarboxylated osteocalcin in metabolic complications of human obesity and prediabetes. *Diabetes Metab Res Rev*. 2017;33(3):1–11.

157. Aguilar, Zein, Harmouch, Hafdi, Bornert, Offner, et al. Application of Chitosan in Bone and Dental Engineering. *Molecules*. 2019;24:1–17.

158. Lopes D, Martins-Cruz C, Oliveira MB, Mano JF. Bone physiology as inspiration for tissue regenerative therapies. *Biomaterials*. 2018;185:240–75.

159. Helmi SA, Rohani L, Zaher AR, El Hawary YM, Rancourt DE. Enhanced Osteogenic Differentiation of Pluripotent Stem Cells via γ-Secretase Inhibition. *Int J Mol Sci*. 2021;22(10):5215.

160. McKee MD, Cole WG. *Bone Matrix and Mineralization*. Amsterdam: Elsevier; 2012.

161. Lacerda CMR. Biomaterials for bone tissue engineering. *Bone Regen Concepts, Clin Asp Futur Dir*. 2018:231–54.

162. Subbiah R, Hwang MP, Van SY, Do SH, Park H, Lee K, et al. Osteogenic/Angiogenic Dual Growth Factor Delivery Microcapsules for Regeneration of Vascularized Bone Tissue. *Adv Healthc Mater*. 2015;4(13):1982–

92.

163. Gurel Pekozer G, Abay Akar N, Cumbul A, Beyzadeoglu T, Torun Kose G. Investigation of Vasculogenesis Inducing Biphasic Scaffolds for Bone Tissue Engineering. *ACS Biomater Sci Eng*. 2021;7(4):1526–38.

164. Cao L, Wang J, Hou J, Xing W, Liu C. Vascularization and bone regeneration in a critical sized defect using 2-N,6-O-sulfated chitosan nanoparticles incorporating BMP-2. *Biomaterials*. 2014;35(2):684–98.

APPENDIX A: ETHICAL APPROVAL FORM

T.C. YEDİTEPE ÜNİVERSİTESİ
Hayvan Deneyleri Yerel Etik Kurulu (HADYEK)

ETİK KURUL KARARI

Protokol No	Toplantı Tarihi	Toplantı Sayısı	Karar No	Proje Yürütücüsü
2020-848	20.06.2020	2020/06	2020/06-3	Prof. Dr. Gamze Torun Köse

'3D baskılı PLLA-PBSu Doku İskelesinin Küçük Molekülle İndüklenmiş Kemik Rejenerasyonunda Kullanımı' isimli proje oy birliğiyle etik açıdan uygun görülmüştür.

Hayvan Türü / Irkı	Toplam Hayvan Sayısı	Hayvanın Cinsiyeti
Sıçan / Sprague Dawley	50	Erkek

Görevi	Adı Soyadı	Katılım Durumu
Başkan	Prof. Dr. Bayram YILMAZ	
Başkan Vekili	Prof. Dr. Erdem YEŞİLADA	
Üye	Veteriner Hekim Engin SÜMER	
Üye	Prof. Dr. M. Ece GENÇ	
Üye	Prof. Dr. Rukset ATTAR	
Üye	Prof. Dr. Gamze TORUN KÖSE	Katılmadı
Üye	Doç. Dr. Ediz DENİZ	
Üye	Doç. Dr. Aylin YABA UÇAR	
Üye	Doç. Dr. Burcu GEMİCİ BAŞOL	Katılmadı
Üye	Hakan GÖKSEL	
Üye	Ahmet ŞENKARDEŞLER	